Atlas to Patient Registration with Brain Tumor Based on a New Mesh-free Method

by

Idanis Beatriz Diaz

A thesis submitted in partial fulfillment of the requirements for the degree of

Doctor of Philosophy

Department of Computing Science

University of Alberta

Abstract

An atlas is an anatomical representation containing all brain structures well identified in a stereotaxic space from a single subject or a population. Atlases provide information about the organization and localization of the different brain tissues.

One may take advantage of this well-organized information for the analysis and processing of a patient's image by warping the atlas to the patient's image, and establishing a one-to-one correspondence between the two images. This process is also known as atlas to patient's image registration and is quite useful for brain tissues segmentation and registering different images to a common reference space. Also, a registered atlas is a model of the patient that can be used for simulation of medical procedures, such as recession and needle insertions.

In the presence of brain tumors, the task of atlas to a patient's image registration becomes even more challenging since tumors deform referential brain structures and cause intensity variations in the affected areas thus augmenting the dissimilarity between the atlas and patient images. Consequently, most of the deformable registration based on intensity or shape similarities between images fail in this cases.

In order to overcome this issue, some methods use bio-mechanical models to simulate the tumor's mass-effect in order to simulate realistic deformations of the brain structures onto the atlas according to the patient's reference MRIs. However, these approaches have weaknesses, mainly related to either the assumption of a spherical growth model of the tumor, or the limitations of the Finite Element Method to simulate large deformations, or the computational time that they require.

We propose a new approach for atlas to patient's image registration with tumor based on bio-mechanical deformation of the brain. But in contrast to other approaches, our method simulates tumor growth with irregular shape by segmenting from the multi-modal magnetic resonance images of a specific patient. We have developed a totally new mesh free method for the bio-mechanical deformation avoiding the limitations of traditional finite element methods. Experimental results are structurally very similar to the patient's image and show that our approach outperforms two of the current top ranking algorithms.

In loving memory of my father Marco Diaz F.
To my mother whom I attribute all my successes in life.
To my love and companion for being at my side
during this life achievement.

Acknowledgements

My most sincerest gratitude and appreciation to my supervisor Dr. Pierre Boulanger for his guidance, great kindness, and support throughout the development of this project.

I would also like to thank Dr. Russel Greiner, Dr. Murtha and the rest of the Brain Tumor Analysis Project for all the knowledge, experience and collaboration that they provided me during the development of my PhD program at the Department of Computing Science.

Contents

List of Figures

List of Tables

Chapter 1

Introduction

Brain tumors are one of the most lethal forms of cancer since they destroy critical structures of body functions and are the cause of the highest mortality rates. With a median of 70%, patients diagnosed with brain tumors will die within sixteen months from the date they are diagnosed [14, 30, 40, 79]. This statistic illustrates the importance of improving diagnosis and treatment of brain tumors in order to increase patient survival outcome and to improve treatment efficiency.

Normally, during treatment, patients undergo several imaging sessions at different times in order to evaluate both the progression of the disease and the success of the treatment. All image sets are integrated and visually inspected in order to track the evolution of the disease. Among all the medical image modalities available, Magnetic Resonance Imaging (MRI) is the preferred choice for imaging brain diseases as it is non-invasive and it can provide high-contrast between soft tissues. The downside for medical teams is that they must deal with large volumetric data sets and face some problems with image alignment as they are commonly acquired without any spatial reference system and diverse voxel spacings. Tumor segmentation of affected regions tends to be carried out manually and subjectively with ill-defined boundaries due to the presence of intensity inhomogeneities and artifacts created by variations of the magnetic fields. All these affect the accuracy of visual inspection, and make it a difficult and an expensive process. In addition, manual identification and segmentation of those images are subjective with great variance between individual oncologists [15, 56, 99].

From the computer science standpoint, one can significantly contribute to this field by developing computational tools for faster and more accurate processing of the information required for diagnosis and treatment. An important contribution, for example, has been the development of automatic tools for accurate medical image segmentation, better known as automatic image analysis.

Automatic analysis of medical images usually entails a complex processing pipeline including [72]: registration, re-sampling, and segmentation. Registration is an essential step when comparing two images because differences in orientation and position of the head relative to the MRI machine generate differences that have nothing to do with tumor evolution [29, 33, 34]. Re-sampling and interpolation are necessary in order to spatially

match the MRIs, especially when the images are acquired with different resolutions and anisotropic spacing. Segmentation is required to localize Regions-Of-Interest (ROI) [5, 74], specially, when quantitative measurements are estimated directly from ROIs in the image.

Inhomogeneity and intensity corrections are also commonly included within the processing pipeline as preprocessing steps. Inhomogeneity correction is necessary in order to compensate for the effect of smooth intensity variations created by fluctuations of the magnetic field during the acquisition process. This phenomenon is caused by different factors that occur during the acquisition of MRIs *e.g.*, radio frequency field fluctuation and gradient driven eddy currents [52, 96]. The intensity inhomogeneities present in all MRIs hinder image registration, tissue segmentation, and consequently voxel-to-voxel comparison between images. The need for intensity normalization arises from the fact that there is not a pulse sequence for a MRI standardized intensity scale as the Hounsfield units in computerized X-ray tomography. In MRI, even for images obtained from the same patient following the same protocol and scanning device can differ from each acquisition [7, 52, 68]. As for field inhomogeneity, the lack of correspondence between tissue properties and intensity values also affects the image registration, segmentation, and the direct comparison between images. No general solution has been found so far that solves the effect of the inhomogeneous fields in the MRI and the lack of intensity normalization between images. Each one represents a challenge in medical image processing.

Bringing the patient's images to a common stereo-taxic space such as an atlas can be the solution of these problems since an atlas is a high resolution image, free of intensity inhomogeneities, where the patient's anatomy can be represented with the same resolution and intensity scale. In this way, atlas images registered to the patient's images can make possible the direct comparison between patient's models to track disease evolution and aid to an accurate analysis of the images.

One of the main contributions of this thesis is to develop an automatic atlas-based MRI image registration method for patients with tumors capable of registering these images in a common stereo-taxic space over time.

1.1 Image Registration

Automatic image registration aims at solving the problem of image miss-alignment. The purpose is to align, map, or match two or more images such that there is a one-to-one spatial correspondence between voxels of the the registered sliced images. The registration problem is often formulated as an optimization problem in order to maximize a cost function ρ that measures the similarity S between a target image I_t and a source image I_s undergoing a transformation $\mathbf{T}_g$ between them [44], *i.e.*:

$$S(I_t, I_s) = \arg\max_{\mathbf{T}_g} \rho(I_t, \mathbf{T}_g(I_s)). \tag{1.1}$$

The transformation $\mathbf{T}_g$ that maps the source image I_s to the target image I_t applies a constrained distortion to I_s such that the slice pixels in I_s corresponds to the slice pixels in

(a) Patient Image (b) Atlas Image

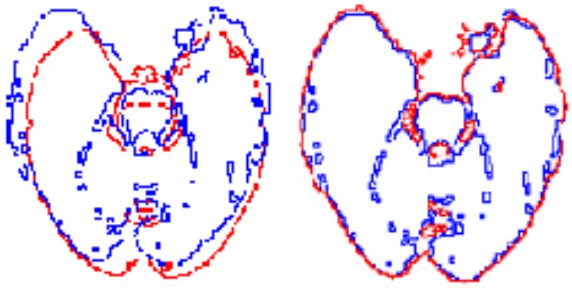

(c) No matching edges (d) Matching edges

Figure 1.1: At the top are two slices from a patient image (a) and from an atlas (b), at the bottom the blue line corresponds to the edge of the patient's slice and the red line to the atlas's slice. The edges deploy the miss-matching without registration in (c), and the matching after applying demon-based deformable registration in (d). The patient slice was taken from NCI-MICCAI 2013 and the atlas slice belongs to the SRI24 Atlas [78].

I_t. The transformation model involves linear and non-linear operations such as rotation, translation, scaling, shearing, and displacements. Figure 1.1 shows a registration example between a patient MRI slice image and its corresponding atlas Figure (3.6b). Figure (1.1c) shows the miss-match between the edges of the patient sliced image and the atlas and Figure (1.1d) shows the computed transformation after applying a demon-based deformable registration algorithm [91]. The blue lines corresponds to the patient slice image edges and the red lines to the atlas image edges.

1.2 Atlas to Patient Registration

The anatomical deformation of brain structures, and intensity variations caused by the presence of a tumor augment the dissimilarity between patient and atlas images, making the registration process more complex. Figure 1.2 shows two slices from the same anatomical region, one from an atlas and another from a patient with a tumor. The patient's slice shows deformation caused by the tumor mass-effect that changes the intensity values in the region occupied by the tumor.

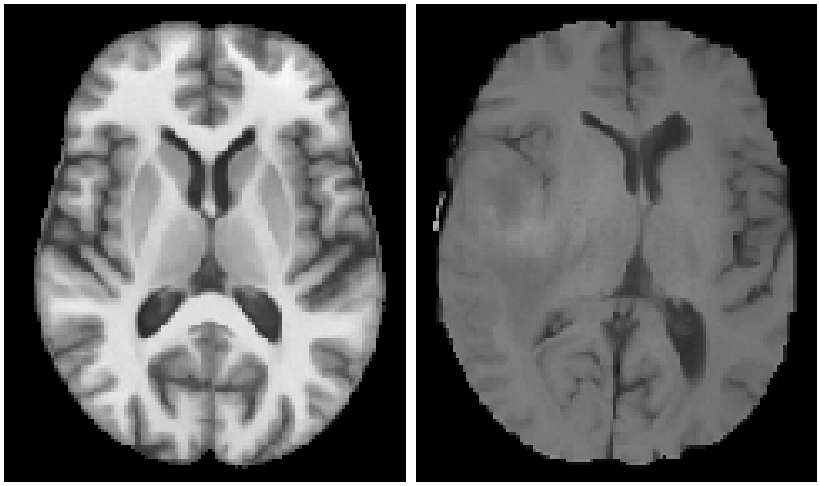

(a) Atlas Image (b) Patient Image

Figure 1.2: Left an atlas slice, right a patient slice with tumor showing the deformation caused by the mass-effect, and intensity variation around the tumor.

For a clearer illustration, Figure 1.3 shows the results obtained by two deformable registration algorithms. The first one, Figure 1.3c, is a symmetric diffeomorphic image registration algorithm with cross-correlation (SyN), introduced by Avants *et al.* [3]. This algorithm was classified as one of the top ranking algorithms for brain MRI registration in [46]. The second algorithm, Figure 1.3d, is the diffeo-morphic demon registration implemented in 3D Slicer [75] one of the top medical image processing software from Harvard Medical School. One can immediately see that the resulting deformations produced by both algorithms on the Atlas did not match the shapes of the deformed brain structures in the patient image.

In order to address these limitations in the registration algorithms due to the presence of tumor, some approaches propose specialized modifications of some well-known deformable registration methods, such as the demons algorithm [91] that deals with the large deformation in localized areas closer to the tumor boundaries [16, 18, 87]. Other approaches introduce biomechanical models of brain tissues to simulate the mass-effect deformation using the idea of growing a tumor from a seed [31, 48, 64, 107]. The objective is to attain a more realistic warping of the atlas after deforming the brain structures according to the mechanical pressure caused by the tumor growth. Although approaches that use bio-mechanical models to simulate the brain deformation yield better results than those that do not, these approaches also have some limitations as there is no satisfactory model that predicts exactly how tumors grow. Most current methods assume an unrealistic omni-directional constant pressure model that causes the tumor to grow spherically. This is not the case for real tumors. Brain tumors, specially at an advanced stage, such as glioblastomas, show irregular shapes causing no regular deformation. One way to simulate tumor growth is the use of Finite Element Methods (FEM) to compute bio-mechanical

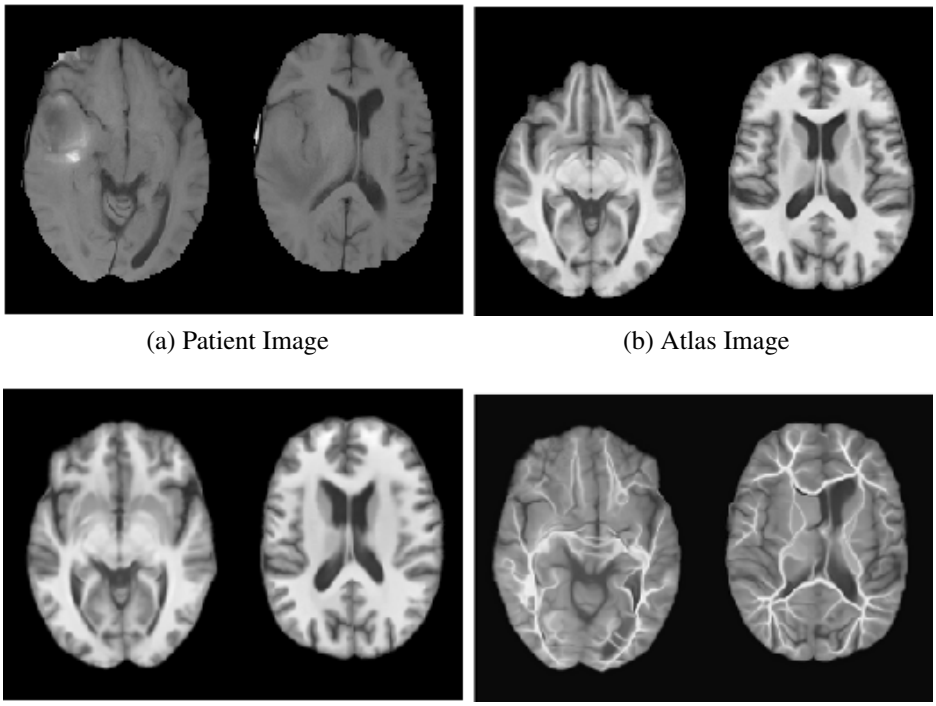

(a) Patient Image (b) Atlas Image

(c) SyN Registration (d) Diffeomorphic Demon Registration

Figure 1.3: At the top, (a) contains two slices taken from a patient image, and (b) contains the respective slices from an atlas after affine registration. At the bottom, (c) the result after Symmetric Diffeomorphic Image Registration with Cross-Correlation (SyN), and (d) the result after Diffeomorphic Demon registration.

deformation. FEM methods usually use triangular or tetrahedral meshes which are not suitable to simulate large deformations because large distortions require that the structural elements deal with non-linear energy functions. The high computational time required by these approaches is another limitation of these methods.

1.3 Applications of Atlas Registration

The importance of atlas to patient registration relies on its diverse applications. Lets discuss some of the most important issues.

Likely the most important application is to *image segmentation*, which consists of assigning a label to a region of interest (ROI) or to regions in an image with shared common features, such as, the localization and labeling of all voxels belonging to different types of brain tissues. A digital brain atlas facilitates segmentation because it is an anatomical representation in a stereotaxic space from a single subject or a population containing common brain structures clearly identified. When a correspondence between an atlas and an image is established through registration, one can then use the labeled structures of an atlas and label a patient image and thus solving the affected structure identification problem. One can find

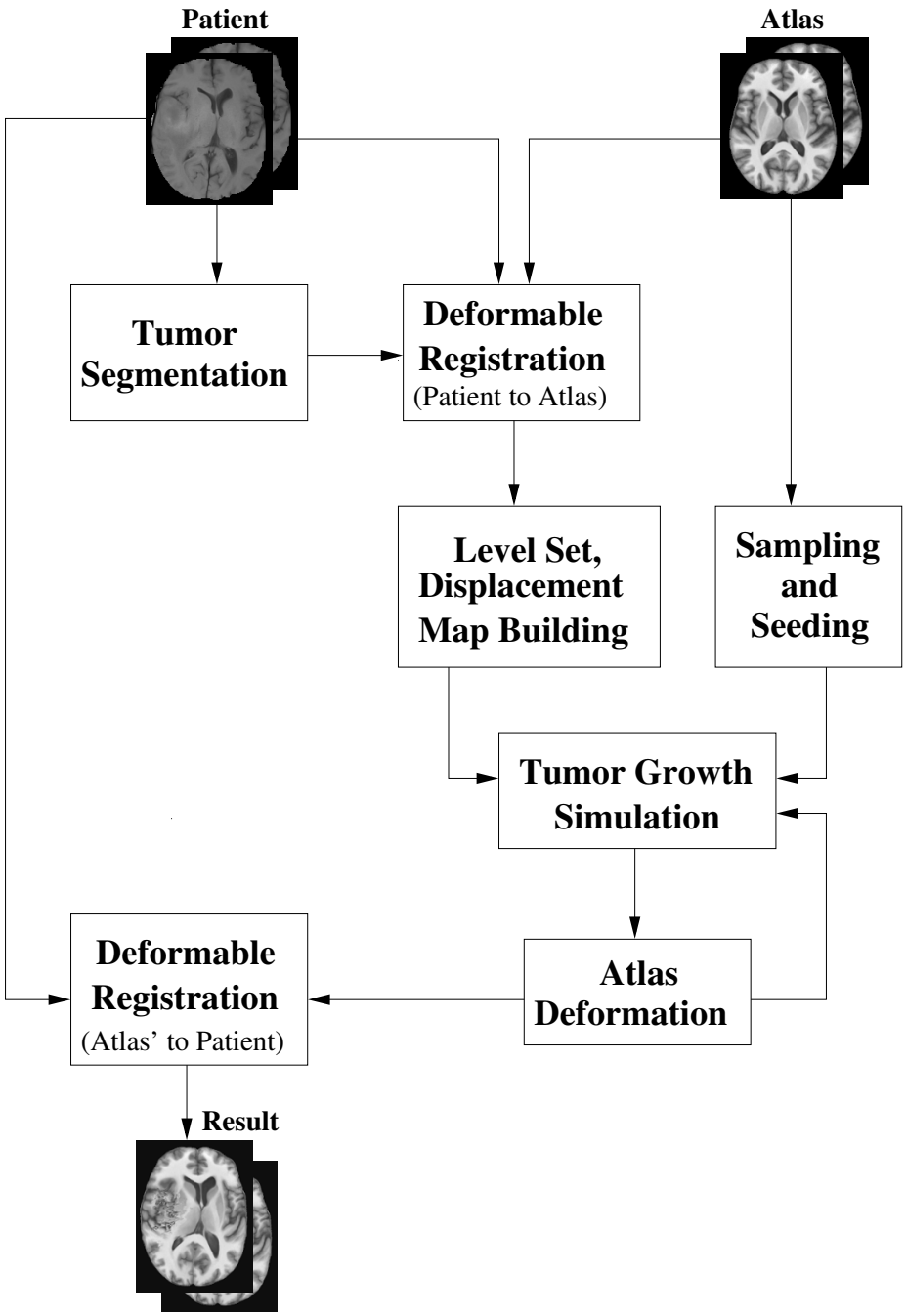

Figure 1.4: Flow diagram of the proposed algorithm ARMSTG.

in the literature several works that follow this direction where they segment images using a classification algorithm guided by prior knowledge provided by an atlas [12, 76, 98].

Another important application of atlas to patient registration is statistical image analysis of diseases based on population studies. Some research works have provided population-based atlas of the development and of evolution of diseases such as Alzheimers over time by registering patient data to a common reference space (an atlas) [2, 92]. Registering

population data to a common reference space allows to compare neuro-anatomical features between groups classified by: age, sex, and disease evolution grade.

Registered atlas to patient images can also be useful for patient image comparisons. This is an important step to quantify tumor progression or assess treatment effectiveness. Tracking the evolution of a brain tumor in medical images entails direct comparison between images. Many methods in the literature subtract images acquired at different times to analyze the differences between them [35, 49, 77, 90]. However, a direct subtraction of images likely generates artifacts that may be misinterpreted as changes caused by the disease. By using atlas to patient registration, one can preserve the atlas resolution and alleviate the problems caused by different intensity scales and slice misalignments.

Also, registered atlases to patients can help for surgical and treatment planning. One advantages of a registered atlas is that the model is suitable for surgical simulations, such as recession and needle insertions. In the literature one can find works that aim at using patient-specific models of the brain for surgery simulation [61, 88] and needle insertion [101].

1.4 Contributions

In this thesis, we propose a new approach to atlas to patient's image registration with the presence of tumor, based on a bio-mechanical deformation model of the brain. While most approaches assume a regular shape, our method simulates tumor growth following the irregular shape of the tumor segmented from the patient's multi-modal images. We proposed a new mesh-free method for the bio-mechanical deformation avoiding the limitations of FEM. Additionally, our approach is implemented in parallel in a Graphic Processor Unit (GPU) using Compute Unified Device Architecture (CUDA) which helps us reduce the computation time required for the simulations.

We will refer to the method proposed in this work as ARMSTG, which stands for Atlas Registration Based on Mesh-free Simulation of Tumor Growth. Figure 1.4 summarizes the method consisting of several steps including: tumor segmentation, fitting the segmented tumor within the brain atlas boundaries through deformable registration, building a displacement map of the tumor boundary from a level set method, sampling and seeding the atlas to perform mesh-free growth simulations, tumor growth and mass-effect simulations, and a finally atlas warping to the patient's image by registering the deformed atlas to the patient's images. In the thesis, we demonstrate that our method produces some of the best results in the literature and that they are structurally more similar to the one obtained with other methods based on non-linear deformation. We compared ARMSTG with two of the top ranked algorithms for brain MRI registration reported by Klein *et al.* in [46] and demonstrated that it compares favorably. Our most relevant contributions are:

1. A mesh-free Total Lagrangian Explicit Dynamic (TLED) method to simulate the bio-mechanical brain tissue deformation caused by a tumor;

2. A tumor growth model based on a level-set displacement map that follows the shape of the tumor of real patient for the simulation;

3. A GPU implementation of the mesh-free method for brain tumor growth and mass effect simulation in an atlas.

1.5 Publications

The following papers have been published or are under revision in the context of this work:

1. A Critical Review of the Effect of De-noising Algorithms on MRI Brain, in the Annual International Conference of the IEEE Engineering in Medicine and Biology Society [19];

2. An Automatic Brain Tumor Segmenter Tool, in the 35th Annual International Conference of the IEEE Engineering in Medicine and Biology Society [20];

3. Fully Automated Brain Tumor Segmentation using two MRI Modalities, in the International Symposium on Visual Computing [81];

4. Atlas to Patient Registration with Brain Tumor Based on a Mesh-free Method (Submitted to EMBC 2015, accepted).

1.6 Organization

The rest of this documents is organized as following. Chapter 2 reviews some prior methods proposed to deal with atlas to patient registration in the presence of a tumor and explains some challenges entailed by this task. Chapter 3 describes our approach, giving details of each stage and shows the results obtained from each one. In Chapter 4, we present some experimental results that demonstrate the performance of our new method. Chapter 5 concludes this work, discussing the pros and cons of the algorithm and describe new directions of the work.

Chapter 2

Literature Review of Atlas to Patient Registration with Tumor

Atlas to patient's image registration have been used to register patient's image into a pre-established high resolution common reference system [93]. Bringing a patient's MRI to the stereotaxic space of an atlas has the following advantages:

1. In the atlas space, the distinctive brain tissues are already well segmented and labeled;
2. The atlas image is free of distortions and intensity inhomogeneities, two factors that hamper the performance of image processing algorithms;
3. A set of images on a common reference system allows the application of many image operations such as direct comparison, and operations for statistical analysis that otherwise might yield inaccurate results.

The registration of an atlas to patient's image is usually carried out by warping the atlas to the target by performing image deformation. Most of the algorithms based on deformable registration are not designed to deal with large deformations and dissimilarities as they have to deal with non-linear energy functions that are known to be unstable . This is why images with brain tumors are very challenging for deformable registration algorithms because of the lack of topological and intensity equivalences between the atlas and patient image. In addition, large distortions caused by the tumor mass-effect may not be smooth as many of the registration algorithms assume [80].

Some approaches deals with the problem of an atlas to a patient registration in the presence of a tumor by trying to reduce the differences between images by simulating the tumor growth in the atlas and then performing a classical deformable registration method based on geometric warping functions [31, 64, 106]. Some other approaches mask the tumor area in the images in such a way that the affected regions do not influence the deformable matching process. In both cases, authors have used either bio-mechanical models to deform the atlas or simpler strategies that do not involve bio-mechanical models at all. The review presented in this chapter has been divided according to two main categories shown in Figure 2.1. Section 2.1 describes methods in the first category which do not use brain tissue

bio-mechanics models. While Section 2.2, reviews methods using bio-mechanical models that can simulate tumor mass-effect. Section 2.3 presents a summary of the reviewed methods in Table 2.1.

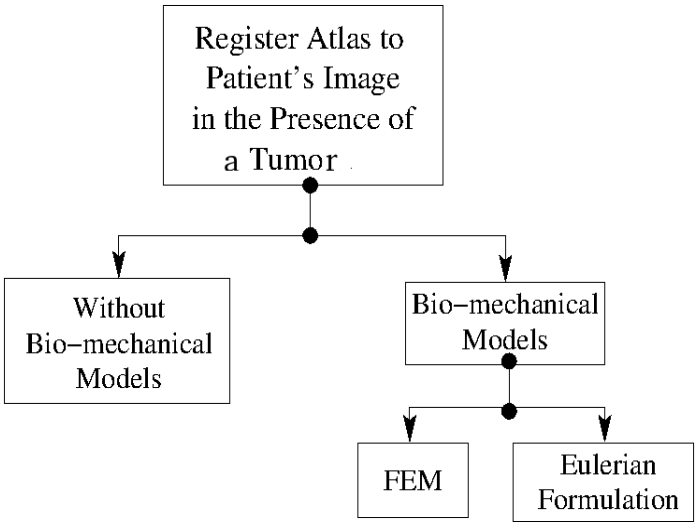

Figure 2.1: Categorization for atlas to patient's image registration in the presence of a tumor.

2.1 Methods Without Bio-mechanical Models

Most of the methods that do not include bio-mechanical models rely on different versions of deformable registration algorithms using optical flow information. The main modification of this simple algorithm is the use of a variable regularization term that allows large deformation in regions around the tumor and other regions of interest while limiting deformation in others.

A representative algorithm was developed by Dawant *et al.* [18], which introduces an approach where an atlas is registered to a volume with a large lesion. The approach involves seeding a tumor in an atlas and then deforming the seed using a modified version of the demons-based registration algorithm proposed by Thirion [91].

Thirion's algorithm is inspired by an analogy to Maxwell's thermodynamic demons [91] and is used by many researchers in the field. The algorithm views registration of two images as a diffusion process where the boundaries in one of the images, called the scene S, are considered as semi-permeable membranes, and the other image is considered as a deformable grid model or a diffusing model M. A set of effectors (demons), situated within the membranes, artificially diffuses M into S through an iterative process that depends on: the position of all demons, a deformation operator $\mathcal{T}$ composed of a sequence of discrete transformations represented as displacement fields, an interpolation method, and an equation to estimate the instantaneous force $\boldsymbol{f}$ that the individual demons exert onto the deformable model M and the scene S. The demons' forces are proportional to displacement

field velocities $\boldsymbol{v}$ and are estimated using:

$$\boldsymbol{v}_{i+1}(\boldsymbol{p}) = G_{|\Sigma|} * \left(\boldsymbol{v}_i(\boldsymbol{p}) - \frac{|M(\mathcal{T}_i(\boldsymbol{p})) - S(\boldsymbol{p})|}{\|\nabla S(\boldsymbol{p})\|^2 + \|M(\mathcal{T}_i(\boldsymbol{p})) - S(\boldsymbol{p})\|^2} \, \boldsymbol{s}_i(\boldsymbol{p}) \right) \tag{2.1}$$

where $\boldsymbol{p}$ is the 3D indexed position in the image, $G_{|\Sigma|}$ is a zero-mean Gaussian filter with standard covariance matrix $\boldsymbol{\Sigma}$ and where $*$ is a convolution operator.

The demon-based registration algorithm assumes that the element positions in the region-of-interest change but the intensities of individual voxels remain constant. Also, it assumes that the displacement field slowly varies at each iteration. This assumption is imposed in order to control stability and yield a more reliable deformation of the demons' exerting force. At each iteration, the displacement field is smoothed by a regularization term. In Thirion's first implementation, the regularization term is the output of a Gaussian filter with a multidimensional covariance matrix $\boldsymbol{\Sigma}$. Thus the displacement field between two images is iteratively approximated by Equation (2.1).

In Dawan *et al.* [18], the initial seed location is extracted by segmenting the image followed by eroding the segmented region using a morphological operator to smooth its boundary. Once the seed is estimated, it is registered relative to the atlas using a rigid transformation. Following these steps, a mask is created by assigning a distinctive intensity value of the seed region that is distinct from the rest of the tissues in the atlas. The authors implemented a hierarchical version of Thirion's registration method that maintains the compatibility between the forward and reverse motion fields. This deformable registration method is capable of warping the seed atlas to the patient's image.

In order to control the deformation in the atlas, the authors propose to vary the regularization parameter in Equation 2.1 at each iteration. The regularization parameter is a Gaussian filter that smooths the deformation caused by the demon forces. In this approach, the parameter σ in Equation 2.1 varied according to the tissue type in such a way that the deformation is larger around the tumor and smaller in other regions. The approach reduces the morphological differences between the atlas and the patient's image by placing a seed with almost the same size as the real tumor and with the same intensity value. This is one of the the major disadvantage of this method since a large seed region may mask other structures in the brain, *e.g.* ventricles, and may lead to an erroneous deformation result as the disturbance of the deformation field is very large. Another disadvantage of this method is that Dawan *et al.* did not present any quantitative evaluation of the proposed method. They mentioned that future work would be done to evaluate the method and select its optimal parameters.

In order to overcome the problem caused by large tumor seeds, Cuadra *et al.* [16] extends the approach in [18] and introduces another method for atlas deformation called *Model of Lesion Growth (MLG)*. In this approach, the initial seed is manually placed in the atlas by an expert, according to anatomical and biological knowledge of tumor growth. The authors propose to use a simple spherical growth model for the seed that is then integrated into a non-linear demons-based registration algorithm. The algorithm drives the deformation outside the tumor area with the demons algorithm using Equation (2.1); while inside

the tumor, the deformation is driven by a spherical growth model. The regularization term used in this approach is based on an adaptive Gaussian filter that smooths the displacement field at each voxels. The filter parameters varies according to three area types: inside the tumor ($\sigma = 0$), around the tumor ($\sigma = 0.5$), and the rest of the brain ($\sigma = 0.08$). The authors did observed a correlation between the brain deformation caused by the tumor growth and the position of the seed. We will see in the next section that this observation is also valid for methods based on bio-mechanics models. Moreover, the tumor seed localization is an unknown parameter that must be identified in order to obtain accurate deformation results. The major limitation of the Dawant *et al.* method is the radial growth assumption for the tumor, which does not resemble the growth of a real tumor. The method only works well when the tumor is close to a spherical shapes. Figure 2.2 shows a block diagram of Cuadra's *et al.* method. The registration results of this method were visually evaluated by

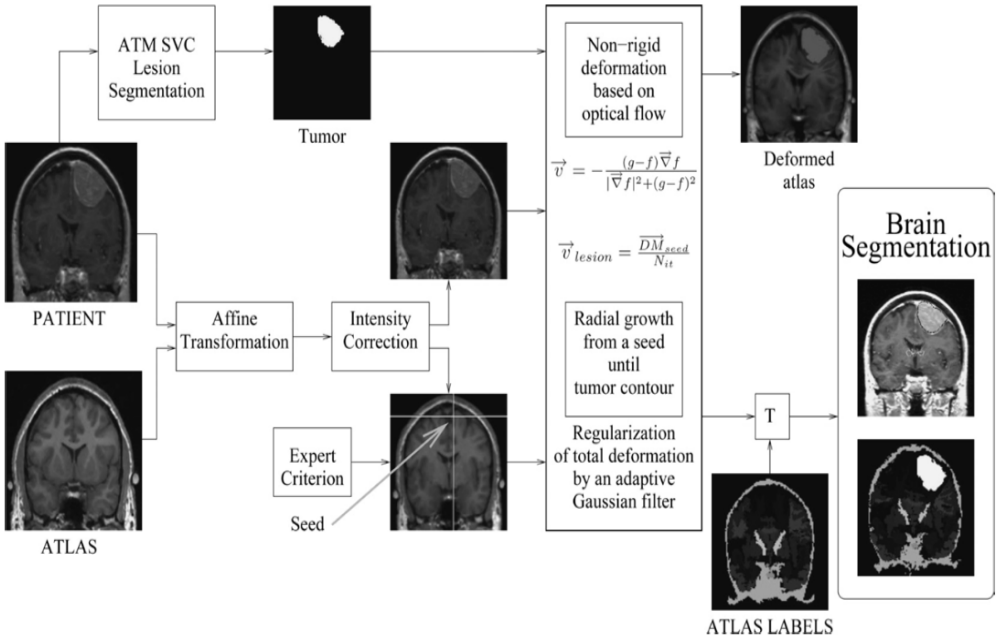

Figure 2.2: Block diagram of Cuadra's *et al.* [16] method (MLG) for atlas to patient registration in presence of tumor.

an expert. Cuadra *et al.* [16] also used as a metric the mean square error between the registered image and the source. However, the authors stated that this metric is not properly to measure the accuracy of inter-patient matching because of the lack of correspondence between image intensities.

Stefanescu *et al.* [87] attempts to solve the problem of atlas to subject registration by using a tumor mask. The method also relies on a non-rigid registration method based on optical flow in [86]. The registration method iteratively optimizes a similarity criterion that uses a regularising term similar to an anisotropic diffusion filter. The procedure allows some areas to undergo larger deformation than others according to a parameter d that af-

fects the regularization term and is assigned according to tissue segmentation of the image. Stefanescu also proposed to assign confidence values to voxels according to the squared local correlation coefficient used as a second similarity criterion between the source and the target. Voxels with low confidence do not influence the alignment process. For the tumor cases, the authors assign a null confidence value to all voxels inside the dilation mask. This approach does not place the tumor in the atlas since the purpose of this method is only to deform the brain tissues to match the unaffected regions in the patient's image. The method was tested over 22 T1-weighted images. However, the author did not present any quantitative evaluation of the registration results.

A more recent approach for deformable registration of brain MRI with tumor was proposed by Parisot *et al.* in [71]. The approach consists of a concurrent registration and tumor segmentation framework, where a sparse grid is superimposed to the volume domain and each node is simultaneously displaced and classified. The method starts with a first approximation to the tumor segmentation obtained with a Gentle Adaboost Algorithm [26]. The problem domain is modeled as a unified pairwise discrete Markov Random Field (MRF) on a graph, where a label is assigned to each node x. Each label is associated to a value that characterizes the node as tumor or background, and a displacement value. The optimal segmentation-registration is found out by minimizing a MRF energy equation that involves unary terms representing classification likelihoods, a similarity metric between the source and target images, and pairwise terms to control the smoothness of the concurrent registration and segmentation. This approach relaxes the registration term in areas with high classification score leading to high dissimilarity between volumes, and at the same time introduces spatial information on the brain structures to reduce false tumor detection. The method result were evaluated mostly qualitatively, although the authors also presented a quantitative analysis of 33 FLAIR volumes based on Dice score, False and True Positive and mean absolute distance between contours outside of the tumor area.

2.1.1 Discussion

The difference between a normal atlas representing a healthy brain and a patient's image with a tumor lies not only with the lesion itself but also with the secondary deformations present in the rest of brain structures. For example, the ventricles in a patient's image may appear displaced and deformed due to the pressure exerted by the tumor, *i.e.* mass-effect, or the tissue texture and intensity around the tumor created by the presence of edema and infiltration. Figure 2.3 shows the deformation caused by the mass-effect to the ventricles for three different patients. One can see that the tumor's geometry is quite irregular and far from the spherical approximation assumed in [16]. All methods proposed by Dawant *et al.* [18], Cuadra *et al.* [16] and Stefanescu *et al.* [87] consider the tumor as the only major differences between a healthy and cancerous brain without considering changes to other structures or reference points. These approximations will result in large differences between the images that will lead to inexact results. Another general issue with those methods is the selection of the parameter that controls the regularization term. The value

should not only vary according to the tissue type, but also with the deformation level caused by the tumor mass-effect. In general, this parameter is set in an *ad hoc* manner and there is no real understanding on what is the effect of this parameter on the registration.

Parisot *et al.* [71] proposed a more recent method that addresses the problem in another direction. The registration problem is coupled with the tumor segmentation problem in a unified pairwise discrete MRF model on a sparse grid. One of the main issues of this method relies on the initial tumor segmentation carried out with a Gentle Adaboost Algorithm [26] which may introduces initial segmentation errors. Another issue is that similar to the other methods reviewed in this section, this approach only focuses on handling the large dissimilarity in the tumor area, and does not consider the dissimilarity caused by the deformation of the brain structures.

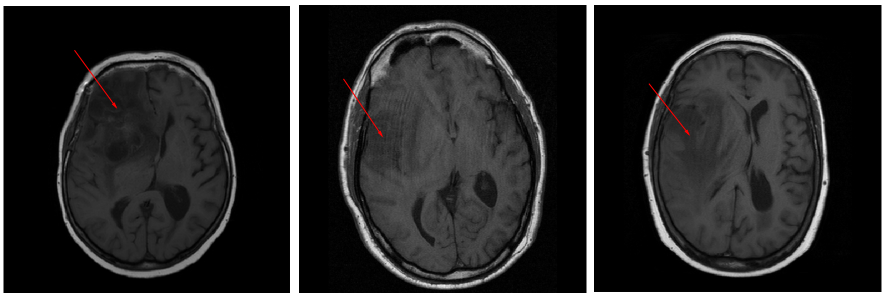

(a) Patient 1 (b) Patient 2 (c) Patient 3

Figure 2.3: Mass-effect from three different patient cases. The slices were taken from a T1-weighted MRI. The tumors are located in areas pointed out by the arrows. The images were provided by The Brain Tumor Analysis Project at University of Alberta [67].

2.2 Methods Based on Bio-mechanical Models

In the literature, one can find numerous methods that use bio-mechanics models of brain tissues to study the deformation generated by the presence of a tumor. One of the most popular is the Finite Element Method (FEM) [6] that approximate the atlas by using an irregular 3D mesh and a discretization of the constituent law of continuous mechanics at each mesh node. A second approach is based on an Eulerian formulation [25, 53]. The Eulerian description, introduced by d'Alembert, focuses on giving attention to what is occurring at a fixed point in space as time progresses, instead of giving attention to individual nodes as they move through space and time. Before describing each methods, let's briefly review some bio-mechanical models of brain tissues one can find in the literature.

2.2.1 Models For Brain Tissue Mechanical Properties

The equations that govern the mechanics of a continuous materials include fundamental laws of motion that satisfies various conservation principles such as: mass, momentum,

and energy. Different constitutive equations to model the brain tissue mechanics have been formulated in the literature. The models are divided into two main categories: single-phase viscoelastic and biphasic elastic models. The first class includes: linear elastic model that represents the brain tissues as an isotropic linear elastic solid obeying Hooke's law [57]. The constitutive equation proposed by this model is:

$$\boldsymbol{\sigma} = \lambda \operatorname{Tr}(\boldsymbol{\varepsilon})\mathbf{I} + 2\mu\boldsymbol{\varepsilon} \tag{2.2}$$

where $\boldsymbol{\sigma}$ is the strain tensor, $\boldsymbol{\varepsilon}$ is the stress tensor, $\mathbf{I}$ is an identity matrix and λ and μ are the first and second Lamé parameters [55].

The single-phase viscoelastic representation also includes constitutive models based on quasi-linear viscoelasticity theory [28]. The assumption behind this model is that brain tissues are non-linear elastic solids that can be represented by equations modeling hyper-elastic behavior with a linear viscoelastic relaxation term to describe time-dependency. The Mooney-Rivlin and the Ogdeon are hyper-elastic models used for this purpose [9]. The Mooney-Rivlin equation defines the strain energy potential in terms of the material constants μ_i:

$$W = \frac{\mu_1}{2}\left(\overline{I}_1 - 3\right) + \frac{\mu_2}{2}\left(\overline{I}_2 - 3\right) \tag{2.3}$$

$$\overline{I}_1 = J^{-\frac{2}{3}} I_1 \qquad I_1 = \lambda_1^2 + \lambda_2^2 + \lambda_3^2 \qquad J = \det(\mathbf{F}) \tag{2.4}$$

$$\overline{I}_2 = J^{-\frac{4}{3}} I_2 \qquad I_2 = \lambda_1^2\lambda_2^2 + \lambda_2^2\lambda_3^2 + \lambda_3^2\lambda_1^2 \tag{2.5}$$

where W is the energy function, $\overline{I}_1$ and $\overline{I}_2$ are the first and the second invariants of the unimodular component of the left Cauchy-Green deformation tensor; and $\mathbf{F}$ is the deformation gradient, for an incompressible material, $J = 1$.

The Ogdeon model defines the strain energy potential in terms of the material parameters μ_i, α_i and the principal stretch ratios λ_i. The most recent constitutive equation that follows the Ogdeon formulation is proposed by Miller and Chinzei [59], and is defined as:

$$W = \frac{2}{\alpha^2} \int_0^t \left[\mu(t-\tau)\frac{d}{d\tau}(\lambda_1^2 + \lambda_2^2 + \lambda_3^2 - 3)\right] d\tau \tag{2.6}$$

$$\mu = \mu_0 \left[1 - \sum_{k=1}^{n} g_k \left(1 - \exp(-t/\tau_k)\right)\right] \tag{2.7}$$

where W is an energy function; $\lambda_i \in \{1, 2, 3\}$ are the principal stretches; μ_0 is the instantaneous shear modulus in the un-deformed state; τ_k are the characteristic times; g_k are relaxation coefficients; and α is a material coefficient.

The other class of models is the biphasic elastic representation, that is based on Hakim *et al.* [36] work who stated that brain tissues are similar to porous solids saturated by fluid where they change according to the hydration and applied loads. This model obeys the Biot's consolidation theory [10]. It is well known that the gray matter is stiffer and

less porous than the white matter [73]. Mechanical loadings cause instantaneous tissue displacement and deformation due to hydrodynamic changes of the interstitial fluid. The Partial Differential Equation (PDE) that describe this behavior are:

$$\nabla \cdot G\,\nabla \mathbf{U} + \nabla \frac{G}{1-2\,\nu}\,(\nabla \cdot \mathbf{U}) - \alpha \nabla p = 0 \tag{2.8}$$

$$\alpha \frac{\partial}{\partial t}(\nabla \cdot \mathbf{U}) + \frac{1}{S}\frac{\partial p}{\partial t} - \nabla \cdot k \nabla p = 0 \tag{2.9}$$

where G is the shear modulus, ν is the Poisson ratio, α is the ratio of fluid extracted to volume change of the tissue under compression, k is the hydraulic conductivity and $1/S$ is the amount of fluid that can be force into the tissue under constant volume [13].

2.2.2 Atlas Registration Based on FEM

One of the first attempt to use FEM and bio-mechanical models to register atlas to brain tumor image registration was presented by Kyriacou *et al.* [48]. They proposed to initially shrink the tumor in the patient's image to an infinitesimal mass, and then to register the atlas to the resulting volume without tumor. Once the atlas is registered, the tumor is seeded and expanded in the atlas. This method works over cross-sectional images and with plain stress, assuming zero stress in the normal direction to each section. The displacements caused by the contraction and expansion of the tumor are determined by using FEM over a triangular mesh in 2D. The models for tumor growth and mass-effect are based on two assumptions: that white matter, gray matter, and tumor tissues are non-linear elastic solid material obeying the Mooney-Rivlin model (see Equation 2.3), and that the tumor is stress free with a uniform strain e_0 that make it grows uniformly. Initially, the method shrinks the tumor by applying negative strains, *i.e.* e_0 in the range $[-0.6, -0.9]$. Then, the atlas is registered to the volume without tumor by using a registration method based on an elastic deformable model, proposed by Davatzikos [17]. Once the atlas and volume without tumor are registered, a non-linear regression model estimates the seed initial position and volumetric expansion that generate the best deformation similar to the patient's image. For a circular seed of diameter D_s, the growth diameter D_t is estimated by $D_t = D_s(e_0 + 1)$. Thus, for $e_0 = 0$, the tumor does not grow. This approach simulates the mass-effect over parenchyma, dura, falx membranes, and ventricles. The authors reported some limitations in the practical implementation of this method regarding the distortion of the the mesh, especially around the tumor. Another limitation is the uniform tumor growth, which is not realistic. The authors also reported that the tumor contraction procedure generates unrealistic deformations of the brain anatomy.

Mohamed *et al.* [64] proposed a registration method for brain tumor images that involves: a bio-mechanics model for tumor and peri-tumor edema mass-effects; a statistical training procedure to estimate the model's parameters; and a deformable image registration to refine the deformation in the atlas to the patient's image. The constitutive model for the brain tissue mechanic is based on a hyper-viscoelastic model introduced by Miller and

Chinzei [59] (see Equation 2.6), while the tumor growth model follows Wasserman *et al.* proposal in [97]. The force of expansion generated by the neoplasm is approximated by a constant outward pressure P that acts on the tumor boundary. The edema expansion is also considered in this model, which is simulated with an isotropic strain e expansion in analogy to thermal expansion. The approximation of the tumor and edema in the atlas are represented by two concentric spheres. In order to match the deformation caused by the tumor and edema, the method estimates the following parameters: the center of the tumor c_t, the radii r_t and d_r for the size of the tumor and edema respectively, and the pressure P. These parameters are estimated through a training process that creates a statistical model of the final deformation χ_f from a set of n_s normal subjects. The procedure can simulate the tumor mass-effect with n_m different parameters sets, $\boldsymbol{\theta}[i] = (c_t, r_t, r_d, P, [i] = \{1, \ldots, n_m\})$ over the subject images. Thus, the training step obtains $(n_s \times n_m)$ deformations, which are determined using Principal Component Analysis (PCA). The result is a deformation map estimated from the sum of two components in orthogonal subspaces representing a statistical model of the the transformation caused by the simulated tumor on each subject registered to the atlas. Then, the statistical deformation model is used to warp the atlas to the patient's image. The performance of this method was evaluated over two cases: a real tumor MRI and a simulated volume image with a tumor. In the evaluation, 21 landmarks were selected around the tumor area in both images, the patient's image and atlas. The results show that the maximum and mean errors between the landmarks were reduced by 71% and 57.6% respectively, in comparison to the registration results without the proposed biomechanics model. To illustrate this process, we have taken one of the graphic results presented by Mohamed *et al.* in their paper. In Figure 2.4 one can see the difference between the result obtained by directly applying a registration method to match the atlas to the patient's image without any biomechanics model and the result obtained by Mohamed's *et al.* method.

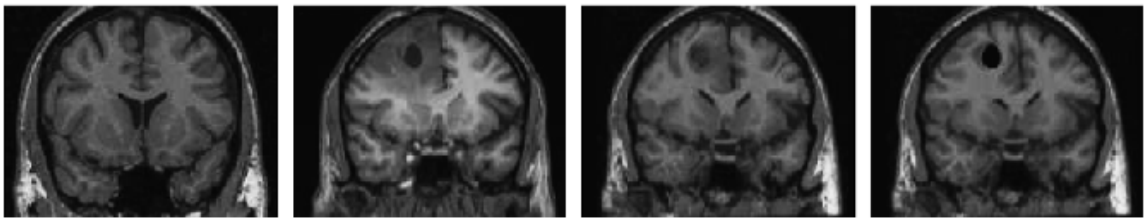

Figure 2.4: A registration result obtained by the method proposed by Mohamed *et al.* [64]. Left to right: atlas image, patient's image, registration result without using bio-mechanical model, and registration result using Mohamed's method.

The statistical procedure proposed in [64] is computationally expensive because of the number of simulations required to apply the PCA is large. Therefore, the use of an optimization process to estimate the possible best model's parameters is computationally unfeasible. For these reasons, Zacharaki *et al.* built a new approach based on Mohamed *et al.* work, *i.e.* a multi-resolution framework called ORBIT [106]. The framework searches for

the best parameters, including: initial position of the tumor seed and size of the seed, that deform the atlas to match the patient's image. The mechanical models for mass-effect and tumor growth used by this approach are the same as the one proposed by Mohamed *et al.*. However, this approach implements a new strategy to approximate the displacement field caused by initial parameters, and an optimization procedure to find the best parameters for a given patient. The approaches consists of three principal steps:

1. *A simulation model for tumor growth and the computation of mass-effect based on local PCA*: In order to make feasible the use of an optimization process, Zacharaki *et al.* propose to separate the training step from the model's parameter search. This approach searches for the tumor seed position $\boldsymbol{x}_t$ and the sizes of the seed r_t. In the training process, ORBIT obtains N displacements fields $\boldsymbol{u}(\boldsymbol{x}_t[i]),\ i = \{1, \ldots, N\}$, with parameters $\boldsymbol{\theta}_i = (\boldsymbol{x}_t[i], r_t[i]),\ i = \{1, \ldots, N\}$. The training process is carried out only once to estimate a mean displacement $\bar{\boldsymbol{u}}$, a matrix $\mathbf{V}$ containing the eigenvectors of the covariance matrix that correspond to the M largest eigenvalues, and a vector $\hat{\boldsymbol{z}} = [\hat{z}^{(1)}, \ldots, \hat{z}^{(M)}]^T$ corresponding to the eigenvalue coefficients. The estimation of these parameters is carried out using PCA over the N displacement fields. Once $\bar{\boldsymbol{u}}$, $\mathbf{V}$, and the vector $\hat{\boldsymbol{z}}$ are determined, a new displacement field $\hat{\boldsymbol{u}}(\boldsymbol{x}_t[j])$ can be approximated for a new tumor parameters $\boldsymbol{\theta}$ by $\hat{\boldsymbol{u}}(\boldsymbol{x}_t[j]) = \bar{\boldsymbol{u}} + \mathbf{V}\hat{z}^j$, where the value of the new $\hat{z}^j$ is interpolated from the previous $\hat{z}^i$ coefficients in the vector $\hat{\boldsymbol{z}}$.

2. *A deformable registration method*: The authors extended the HAMMER method, an elastic deformation method proposed by Dinggang and Davatzikos in [22] for atlas to brain tumor image registration. The deformation method calculates displacement field by maximizing a similarity criterion based on an attribute vector. Each voxel is represented by an attribute vector involving features of the brain structure and tumor geometry in both images: the target and the source.

3. *An optimization process*: The optimality criterion for $\boldsymbol{\theta}$ is given by:

$$\begin{aligned} \boldsymbol{\theta} &= \arg\min_{\theta} \mathbf{E} \\ \mathbf{E} &= \sum_{k=1}^{3} \sum_{x \in \Omega_E} c_k h_k(x) E_k(\mathbf{x}; \theta) \end{aligned} \tag{2.10}$$

   where $\mathbf{E}$ consists of three normalized measures, E_1 : the residual volume between the co-registered atlas and patient's image, E_2 : the distance between attribute vectors, E_3 : the laplacian of the deformation field. c_k : is a weight for each measure E_k and h_k : is a weight according to the voxel location $\mathbf{x}$. The weight value is inversely proportional to the distance from the tumor boundary and $\Omega_{\mathbf{E}}$ is the volume over which $\mathbf{E}$ is calculated.

Figure 2.5 shows a block diagram of this method. ORBIT was evaluated over synthetic and real images. The registration error was estimated to be $1.9 \pm 0.2mm$ around the tumor

and 0.8 for the rest of the tissues. Also, the authors used landmarks to evaluate the method's performance and the distance between the ventricle boundaries. ORBIT results where better than the original HAMMER method and a non-rigid registration method implemented in the Segmentation and Registration Toolkit (ITK) [45]. In another work, Zacharaki *et al.* in [107] proposed a new method based on a statistical model to reduce the computational time [107].

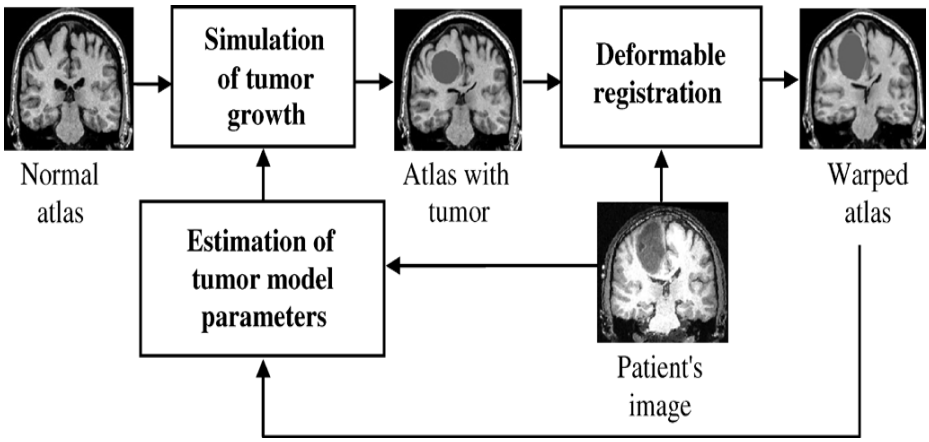

Figure 2.5: Method proposed by Zacharaki *et al.* [106] for atlas to patient registration in the presence of tumor

2.2.3 Methods Based On Eulerian Formulation

Methods based on FEM present some issues related to the need for domain meshing and re-meshing during simulations and to its high computational cost. In addition, large deformations generate non-linearity in the energy function that produce instability and inaccuracies. In the light of these challenges, alternative formulations that do not require meshes have been developed. In this subsection, we present some methods based on two Eulerian Formulations introduced by [37] and [38]. In both models, the brain tissues are represented as a linear inhomogeneous elastic material, with different mechanical properties for white matter, gray matter, and ventricles. The first model in Hogeas *et al.* [37], represents the tumor mechanical action on the surrounding tissues through a uniform outward force at the tumor boundary, *i.e.* as an inhomogeneous linear elastic material that can be represented by a Maxwell-Wiechert model with Neumann boundary conditions. At each iteration of the model, the boundary of the tumor is expanded with a predefined velocity $\mathbf{v} = \dfrac{\partial \mathbf{u}}{\partial t}$. The motion of the boundary is tracked with a level set function of an evolving fronts. All this representation is embedded in a regular grid containing the brain plus a surrounding fictitious material. Figure 2.6 illustrates the grid representation.

Zacharaki *et al.* in [105] compared the first Eulerian model with the model for mass-effect implemented by Mohamed *et al.* in [64]. Similar to the ORBIT structure, the two models were evaluated as a pre-processing step before applying the deformable registration

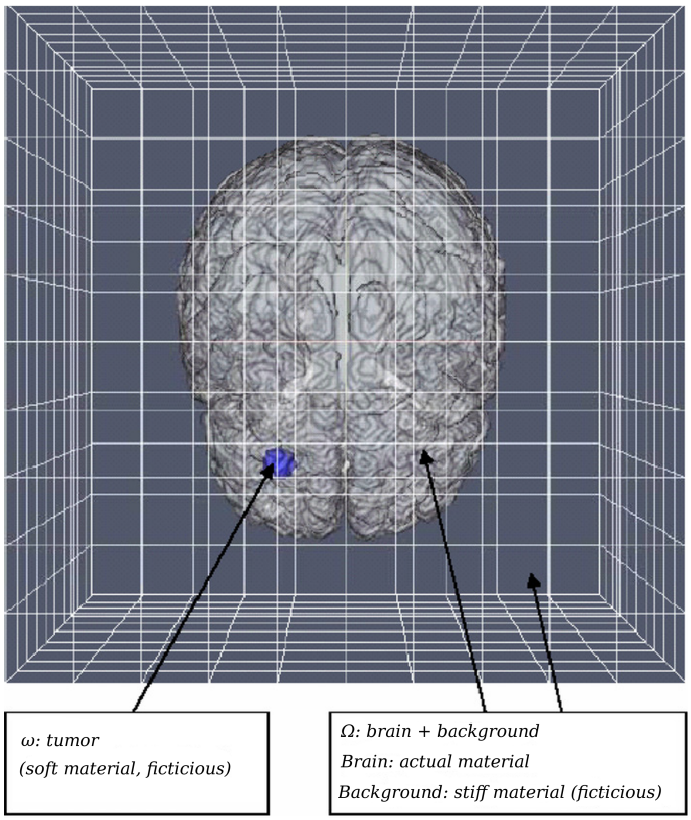

Figure 2.6: This figure illustrates the regular grid used to represent the brain and tumor and to solve the system equations derived from the Eulerian formulation [37].

method based on the HAMMER algorithm [106]. The comparison was performed over four brain tumor patients and the accuracy of the models was assessed by setting landmarks points in the registered atlas and the patient's image. The results indicate a non-significant difference between the models. However, the model in [37] was computed ten times faster than the model used by Mohamed *et al.* [63].

Motivated by the reduction of computational time that Eulerian methods requires, Zacharaki *et al.* presented another work for spatial normalization of MRIs from patients with brain tumors in a common stereotaxic space, with the goal of analyzing groups of patients. The method is an extension of ORBIT using the Eulerian formulation proposed by Hogea *et al.* [37]. In this framework, the authors embedded the simulation framework in an objective function that is solved with an asynchronous parallel patter method called APPSPACK [32]. The method searches for the position and size of the seed as well as a tumor factor to control that the expanding tumor in the atlas does not exceed the size of the real tumor. Tumor growth is simulated in the atlas for a parameter set with a tumor seed that is created by eroding the tumor in the patient's image. Then, the deformable registration method derived from HAMMER is applied. If the similarity between the registered atlas and the patient's image is below a threshold, then the method selects a new set of parameters and

starts again. According to the authors, the registration error of this new implementation was reduced by 55% for the majority of 21 cases in comparison with ORBIT.

The second Eulerian model proposed by Hogeas *et al.* in [38] pursues two different interests: improving the deformable registration from images of brain tumor patients to a common stereotactic space and improving the prediction of glioma growth. In this approach, the glioma growth is represented by a non-linear reaction-advection diffusion model while the brain tissues is modeled as a linear elastic inhomogeneous material as in the previous approach. The tumor exerts a local pressure field on the surrounding tissues, which is given by a parameterized function of the tumor cell density. The equation that represents the tumor density through the time involves three terms: a diffusion term with different coefficients for white matter and gray matter; an advection term that accounts for displaced tumor cells as a consequence of the underlying tissue mechanical deformation; and a reaction term representing the cell proliferation and death.

Gooya *et al.* [31] adopted this second Eulerian formulation with the purpose of registering atlases to brain images with glioblastoma multi-forme, which is a malignant brain tumor with a high fatality rate. Gooya *et al.* use four MRI types, T1, T2, T1C and FLAIR, which are segmented in six different tissues types WM, GM, CSF, enhancing tumor (ET), non-enhancing tumor (NET) and edema (ED). The approach calculates posterior probability maps from the segmented images using the Support Vector Machine (SVM) algorithm. The probability maps from the atlas and the patient's image are registered in an optimization process that involves an expectation maximization procedure to find the joint maximum probabilities for each class. The expectation maximization procedure is in turn encapsulated in a more general optimization process carried out by APPSPACK [32] which searches for the bio-mechanical model parameters, including: seed position, the diffusion coefficients for gray and white matters, a proliferation coefficient, and two parameters required by the function that estimates the local pressure field of the tumor. According to the evaluation, this approach outperforms ORBIT over fifteen patient cases. Gooya *et al.* assessed the accuracy of the method qualitatively, and also quantitatively. The quantitatively evaluation relied on the computation of Jaccard ratios between labels of four segmented regions: grey matter, CFS, tumor and ventricles.

2.2.4 Discussion

According to this review and the published results, the best strategy so far to tackle the problem of atlas to image patient registration with a tumor is by simulating the tumor evolution in the atlas including the mass-effect before applying non-rigid registration. The simulation is carried out via a bio-mechanics model that describes the tumor-growth dynamics and the parenchyma mechanical response to the pressure exerted by the tumor. Most of the methods that follow this direction have been proposed as an optimization problem whose objective is to find optimum values for some parameters such as seed position, seed size, and tumor pressure.

The methods currently developed to simulate tumor evolution and mass-effect in atlas use either Lagrangian formulations by FEM, or Eulerian formulations whose equations are solved using a regular grid. Methods that use FEM present some challenges inherent to the computational cost that they imply, which hamper the use of optimization techniques. One of the reasons for FEM's high computational cost is related to the fact that the brain-structure geometry is represented with an unstructured mesh composed of triangular or tetrahedral elements, *i.e.* a regular geometry approximating a non-regular geometry. Therefore, the larger the number of nodes, the better the brain geometry approximation is. However, as the the number of nodes increases, the computational requirement also increases. Another important factor is that the strain field frequently deteriorates the mesh quality. Consequently, the mesh must be constantly recalculated, which is computationally expensive.

On the other hand, the Eulerian formulation proposed by Hogea *et al.* [37, 38] requires less computational time and can be integrated in one optimization framework, *e.g.* Zacharachi *et al.* [107], Gooya *et al.* [31] and Hogea *et al.* [37, 38]. The Eulerian formulation uses a regular grid, that is simpler to generate than a tetrahedral mesh and does not require being re-meshed. In addition, for simplicity Hogea *et al.* represent brain tissues with a linear-elastic model, which is computationally faster than a hyper-elastic model. However, issues related to the accuracy of a brain structure geometry approximation with a regular grid and the use of a linear-elastic model in this context should be further evaluated. Regular grids whose elements are the same size do not provide the same flexibility of an unstructured mesh to fit irregular geometry with different size elements and density according to the designer's interest. In Figure 2.7 shows an iso-surface triangular mesh over a bone geometry. One can see how different triangle sizes fit the object's surface.

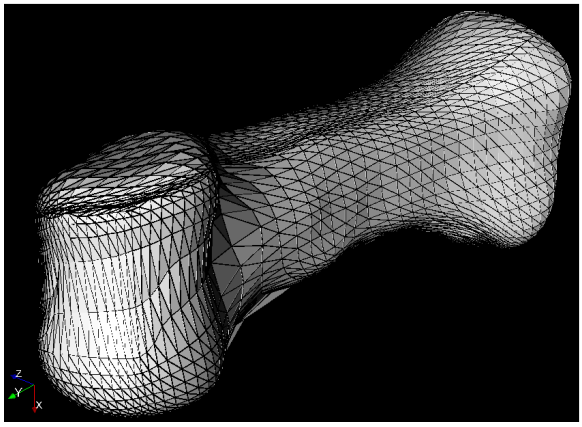

Figure 2.7: Illustration of an iso-surface triangular mesh fit to a bone geometry [75].

2.3 Summary

The following Table summarizes the methods reviewed in this chapter for atlas to brain tumor image registration.

Table 2.1: Methods for Atlas to Brain Tumor Image Registration.

Method	Brain Tissue Model	Tumor Growth Model	Contributions
Dawant *et al.*, 2002, [18]	N/A	N/A	Introduces a large seed in the atlas and propose a registration method based on Thirion's Algorithms [89].
Cuadra *et al.*, 2004, [16]	N/A	Radial Growth	Extends [18], introduces a small tumor seed with radial growth.
Stefanescu *et al.*, 2004, [87]	N/A	N/A	Masks the tumor and introduces a non-rigid registration method based on optical flow with diffusion filter as regularization term.
Kyriacou *et al.*, 1999, [48]	Non-linear elastic solid	Uniform growth with a constant strain	Contracts the tumor from the patient's image before registering the atlas. Then, grows a seed in the atlas.
Mohamed *et al.*, 2006, [64]	Non-linear hyperelastic material	Wasserman's Proposal in [97]	Includes tumor and edema extension in the biomechanical model, implements a statistical strategy to find the model parameters.
Zacharaki *et al.*, 2008, [106]	"	"	Proposes a statistical model to estimate deformation field, uses an optimization framework and introduces a deformable registration method based on HAMMER algorithm [22].

continued in page 24

Method	Brain Tissue Model	Tumor Growth Model	Contributions
Zacharaki *et al.*, 2009, [107]	Inhomogeneous hyperelastic material	Non-linear reaction-advection diffusion model	Is an extension of [106] introducing the Eurlerian formulation proposed by Hogea *et al.* in [37].
Gooya *et al.*, 2011, [31]	”	Non-linear reaction-advection diffusion model	Registers atlas to brain images with Glioblastoma implementing the Eurlerian formulation proposed by Hogea *et al.* in [38].
Parisot *et al.*, 2014, [71]	N/A	N/A	Introduces a concurrent tumor segmentation and atlas to patient registration framework.

Chapter 3

A New Approach for Atlas to Patient Image Registration with Tumor

In the last chapter, we reviewed methods that attempt to solve the problem of atlas to patient registration with tumors, and classified them in two main categories: methods with *vs* without bio-mechanical models. Following the exceptional success of bio-mechanical models over optical flow methods, we will introduce in this chapter a new approach to atlas to patient image registration capable of dealing with brain tumor based on tumor growth and mass-effect simulations. The aim of the simulation is to increase the registration accuracy between the atlas and the original patient image by deforming the atlas's brain structures according to the mechanical behaviour of the brain tissue and tumor pressure. Once the brain structures has been deformed due to the tumor growth and mass-effect simulation, our method applies a common deformable registration procedure to complete the process. The results obtained in this way are more accurate than the results obtained by simply registering the images directly. Our approach consists of a set of steps involving tumor segmentation, deformable registration of the tumor to the atlas space, a level set method to build a displacement map that guides the tumor growth simulation according to the segmentation, sampling and seeding, atlas deformation with a mesh free method, and a finally deformable registration of the atlas after the mass-effect simulation to the patient's image. All these stages are illustrated in Figure 1.4 in Chapter 1, and explained with further details in this chapter.

Our main contributions are focused on the tumor growth simulation in the atlas. The strength of our approach is that it relies on a simulation of tumor growth based on an actual tumor boundary extracted from the patient's image instead of assuming an unrealistic spherical or uniform growth model. Our method also relies on a mesh-free method to compute the mass-effect deformation, and avoid the troubles with mesh-based methods when dealing with large deformations. As an added bonus, our method is implemented in parallel in GPUs using the CUDA language which reduces the computational time required for the simulation. For simplicity, we will refer to our method as ARMSTG, which is an acronym for Atlas Registration Based on Mesh-free Simulation of Tumor Growth. Sections

3.1 to 3.6 correspond to a description of each step illustrated in Figure 1.4. Section 3.7 explains the GPU implementation of the tumor growth and mass-effect simulation.

3.1 Tumor Segmentation

The first stage of ARMSTG as shown in Figure 1.4 consists of segmenting the tumor in the patient's image. ARMSTG works with a binary tumor mask covering all the areas affected by the tumor including edema, tumor core, cysts, and necrotic tissue.

3.1.1 Segmentation Method

During the development of ARMSTG, we used images from the Multi-modal Brain Tumor Segmentation Challenge (BRATS 2013) [58]. This database provides a training data set containing multi-modal MRI scans of patients with low-grade and high-grade gliomas, skull stripped. The database also provides manual segmentation of the tumors that we used to check the accuracy of the segmentation.

As part of this thesis, we have developed an automatic segmentation algorithm, named Simple Tumor Segmenter (STS) [20, 81], which segments brain tumors based on enhanced tumor contrast from standard clinical MRI sequences. This algorithm was designed as part of the the Brain Tumor Analysis Project' objective, which is a collaboration between the University of Alberta's Computing Science Department and the Cross Cancer Institute to improve the treatment of brain tumors by applying machine learning and image processing techniques.

STS segments three distinctive tissues associated to a brain tumor: edema, tumor core, and enhancing rim from four standard clinical MRI sequences: T1-weighted (T1), T1-weighted with gadolinium contrast agent (T1C), T2-weighted (T2), and Fluid Attenuated Inversion Recovery (FLAIR). The core of this algorithm is an automatic histogram multi-thresholding procedure followed by morphological operations that include geodesic transformations [84]. Although segmentation methods based on histograms are very sensitive to the poor contrast at the boundaries of the tissues, STS overcomes this challenge by using the information provided by the different modalities and with the use of a double thresholding at different intensity levels. Figure 3.1 summarizes the segmentation method presented in [20].

This algorithm automatically searches and places different thresholds in the histogram envelope of brain MRIs such as the one depicted in Figure 3.2. In general, brain MRI histograms are bimodal. The first mode contains the most common intensity values in the image background, which are zero or close to zero while the second mode mostly contains intensity values corresponding to brain parenchyma (white and gray matter) and the surrounding soft tissues.

With the use of the localized thresholds, the initial stage of the STS yields binary images that contains all different regions of interest (*e.g.* background, foreground, skull, edema and

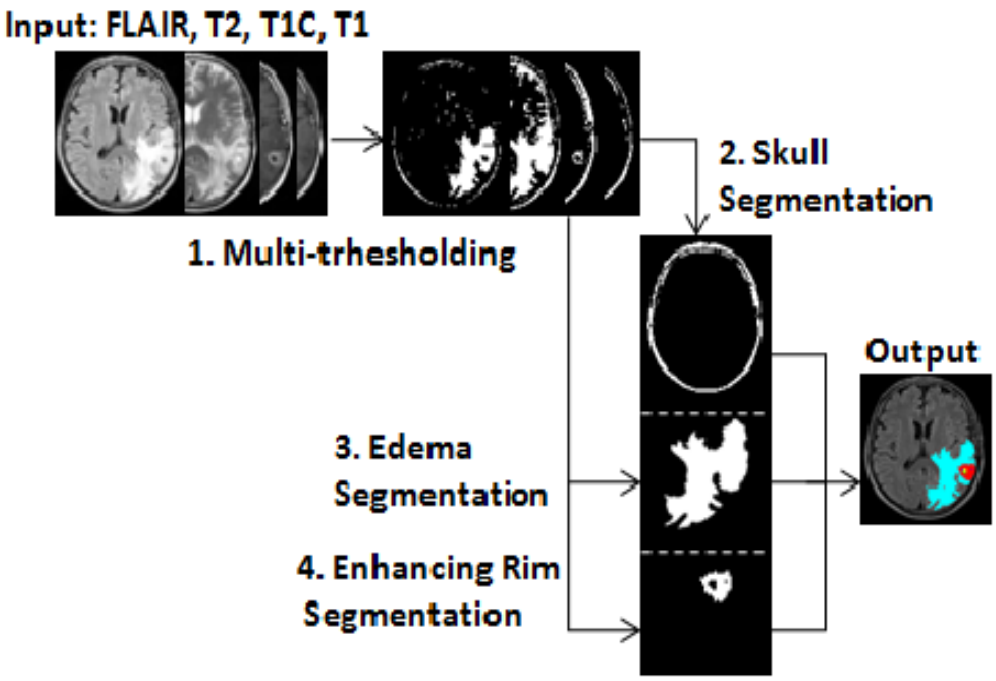

Figure 3.1: Segmentation method based on multi-thresholding

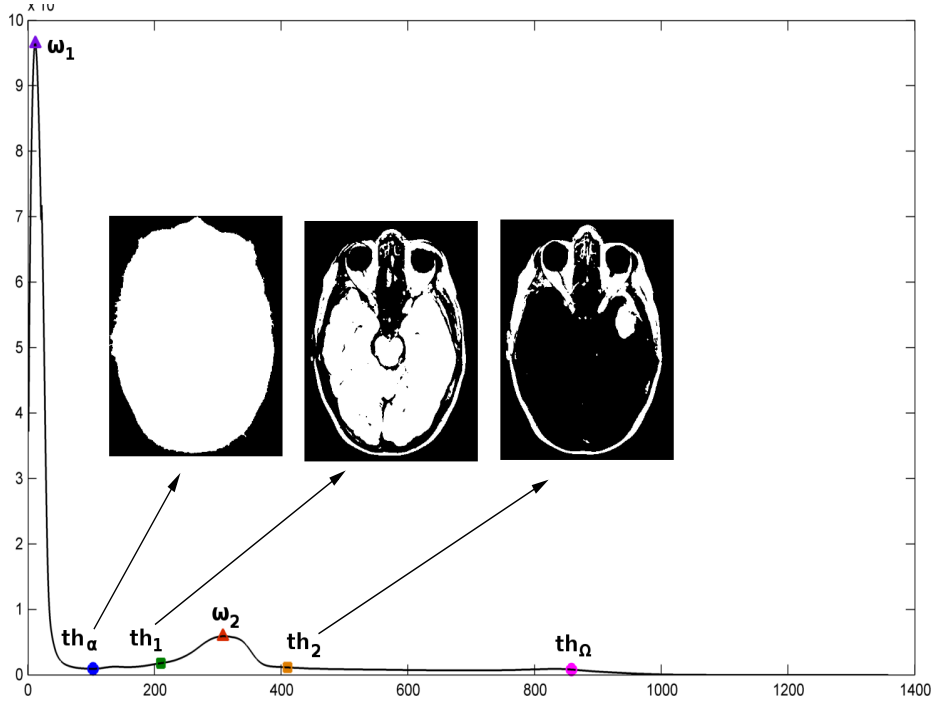

Figure 3.2: Bi-modal function with modes ω_1 and ω_2 and multiple thresholds: th_α, th_1, th_2 and th_Ω

.

enhancing rim) corresponding with high contrast values along the different MRI sequences.

As Figure 3.2 shows, STS localizes three specific thresholds and their resulting binary images are illustrated in Figure (3.3) and Figure (3.4)

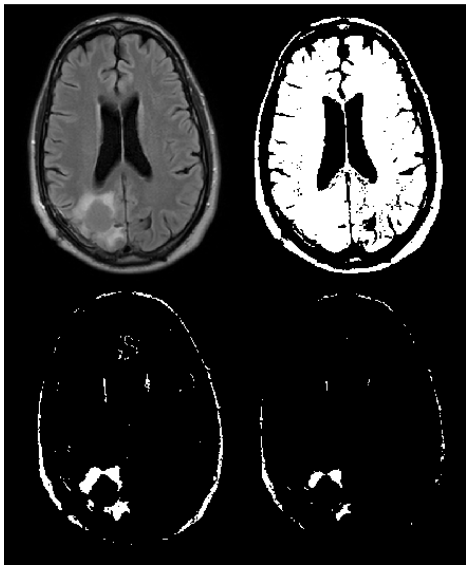

Figure 3.3: Thresholding results on one slice from FLAIR. The top left is the slice in FLAIR and top right is the result of thresholding with th_1. The bottom images are the results obtained by thresholding with th_2 on Flair.

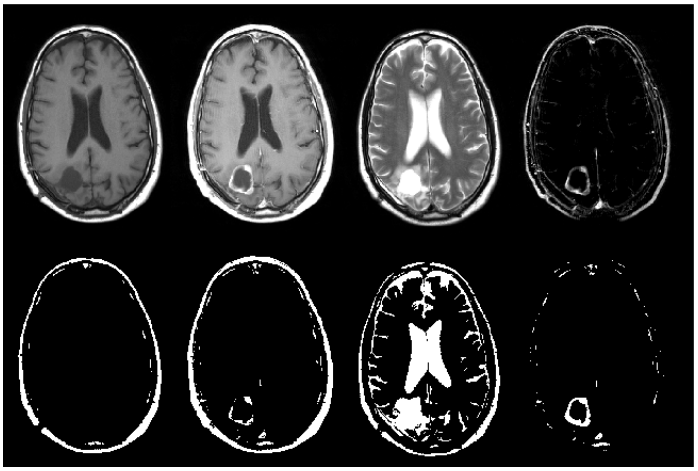

Figure 3.4: Thresholding results on one slice from different MRI sequences. On the top row from left to right: T1, T1C, T2, T1C-T1. On the bottom row from left to right, the thresholding results for th_2 over the respective modality above.

In order to automatically localize the thresholds, STS analyses inflexion points on the histogram envelopes where the sign of the curve slope changes between the first and second modes of the histogram, and after the second mode and th_Ω. This analysis is perform over a smoothed histogram envelope of the MRI using a Savitzky-Golay FIR filter [82].

Thresholds th_α and th_Ω segment the image background and the last fluctuating intensities of the histogram respectively. The threshold th_1 segments the image background plus regions of low intensity such as ventricles and sulci. The resulting image can be seen in Figure 3.2 and at the top right of Figure 3.4 and is a segmentation of the brain tissue, excluding CFS. In the case of BRATS' images the segmentation of the brain tissue is more clear since these images are skull stripped, examples of this can be seen in Figure 3.16. We will refer to this threshold in different part of this document. The threshold th_2 segments high intensity values yielding an image that contains edema or part of the tumor represented with high intensity values and skull.

In order to establish a baseline for the method, we compared segmentation results from a set of sixteen patient cases with glioblastoma at different stages of development. The original clinical sequences were provided by the case database at the Cross Cancer Institute, Alberta. An oncology clinical expert provided a hand-segmentation for these sixteen cases identifying two tumor tissue classes: edema, and enhancing rim around the tumor core. The segmentation results were compared using Dice coefficient [21] to assess the similarity between the images segmented by our method and the images segmented by the expert. The results showed a high degree of agreement between the manual and automatic segmentations for edema and tumor core with the Dice coefficient averages for Edema and Core of 81% and 85% respectively. Figure 3.5 shows a segmented image by STS and the comparison with a manual segmentation.

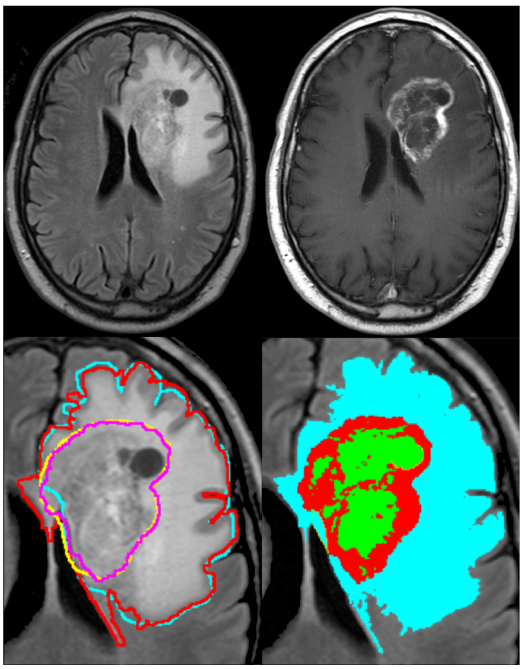

Figure 3.5: STS segmentation.

3.2 Tumor Registration from MRI Space to Atlas Space

Once the tumor is segmented in the patient's MRI images, ARMSTG uses the information related to the position, size, and the segmentation boundaries to guide the simulation of the tumor growth in the atlas. For this purpose, ARMSTG brings the segmented tumor from the patient image space to the high resolution atlas space. The purpose of this step is to grow the tumor in the atlas in a similar location, size, and shape of the original tumor in the patient's image. This step is carried out with the following procedure:

1. ARMSTG extracts two masks representing the brain tissues for the patient and atlas images. (see Figures 3.6a and 3.6b). The masks images are obtained with a simple threshold Th_α in Figure 3.2 that is automatically estimated using the segmentation method in 3.1.

2. The patient mask boundary is then registered to the atlas mask boundary using a deformable registration based on the Demons algorithm [89] (Figure 3.7a).

3. The displacement field of the registration between boundaries is applied to the tumor mask (Figure 3.7b). The result of the deformable registration is a matrix of the same dimension as the atlas image, containing the displacement for each point to match the atlas image. ARMSTG adds the displacement field to the segmented tumor and uses bilinear interpolation to complete the missing information of the reconstructed image.

3.3 Displacement Map for Tumor Growth Simulation using Time Reversal

In this step, ARMSTG shrinks the segmented tumor boundary to a unique seed point using a level set method (see Figure 3.8). During this shrinking process, our method inwardly propagates the boundary of the segmented tumor with a constant velocity in the inverse normal direction of the boundary until it becomes a single point (tumor center). This shrinking process is carried out in the binary mask that was brought to the atlas resolution.

During the tumor growth simulation, ARMSTG regrows the tumor from the tumor center in the outward direction using the evolution of the level set boundaries saved during the shrinking process. Using this boundary evolution, the algorithm computes at each time step the deformation produced by the presence of the tumor based on a bio-mechanical deformation simulation. This reverse procedure is carried out over the atlas image and will later be explained in Section 3.5.1

The level set method was introduced by Osher and Sethian [70] for tracking interface motion. As illustrated in Figure 3.9, an interface is defined as the boundary between two different regions in a given domain. The general idea behind the level set method is to follow the evolution of a function ϕ whose zero-level set always corresponds to the position

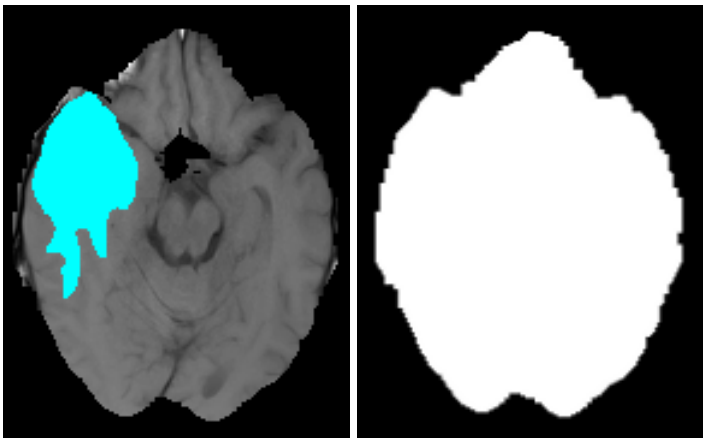

(a) Patient (b) Mask

(c) Atlas (d) Mask

Figure 3.6: At the top, (a) a slice from a patient image, and (b) the mask of the patient slice. At the bottom, (c) the respective slice in an atlas, and (d) the mask of the atlas slice.

of the propagating interface [1]. The motion of ϕ is governed by the partial differential equation:

$$\frac{\partial \phi}{\partial t} + \mathbf{v} \cdot \nabla \phi = 0 \tag{3.1}$$

where t is the time, ∇ is the gradient operator, and $\mathbf{v}$ is the velocity field. The function ϕ moves along its normal vector $\mathbf{n} = \dfrac{\nabla \phi}{\|\nabla \phi\|}$ with velocity $\mathbf{v}$ over time.

The velocity field $\mathbf{v}$ can be defined by $\mathbf{v} = a\,\mathbf{n}$, where a is a constant such that when $a > 0$ the interface moves in the normal outward direction and when $a < 0$ the interface moves in the normal inward direction [69]. Using this notation, the level set equation is defined by:

$$\frac{\partial \phi}{\partial t} + a\|\nabla \phi\| = 0. \tag{3.2}$$

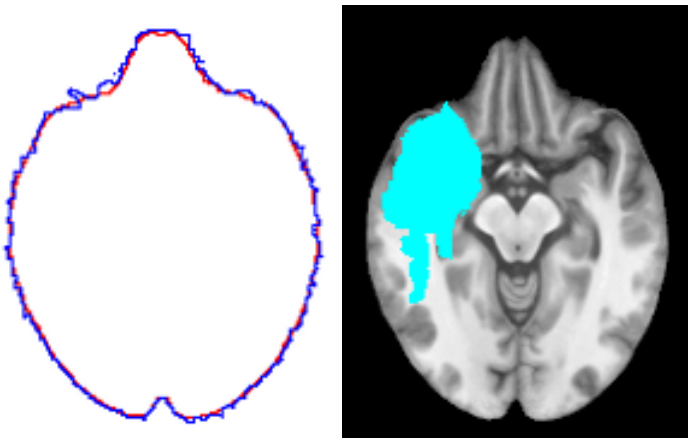

(a) Boundaries (b) Tumor

Figure 3.7: (a) Boundaries of the patient slice (blue) and the atlas slice (red) after registration, and (b) the registered tumor in the atlas slice after deformation.

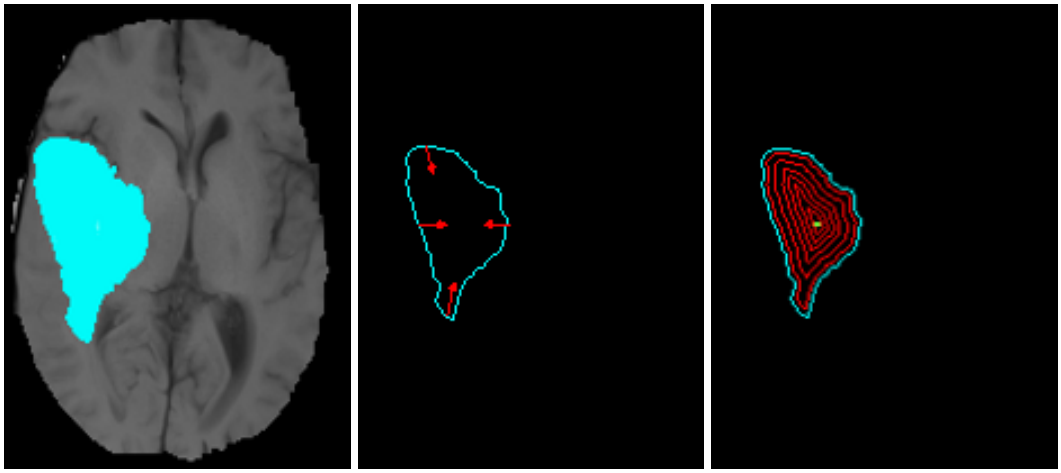

(a) Tumor Segmentation (b) Tumor Boundary (c) Level set Contours

Figure 3.8: (a) tumor segmentation, (b) boundary of the segmentation, and (c) inward level set and the seed in green

In addition, the velocity field $\mathbf{v}$ can be defined as a scalar function $F(\cdot)$ of one or various parameters such as the interface curvatures. Using this notation, the corresponding level set equation is:

$$\frac{\partial \phi}{\partial t} + F(\cdot)\|\nabla \phi\| = 0. \tag{3.3}$$

One can solve the level set equation by approximating $\frac{\partial \phi}{\partial t}$ with: $\frac{\phi^{n+1} - \phi^n}{\Delta t}$.

The function ϕ at a point $\mathbf{x} \in R^N$ is set to be equal to the signed distance function defined by:

$$\begin{cases} \phi(\mathbf{x}) = 0 & \forall\, x \in \partial\Omega \\ \phi(\mathbf{x}) < 0 & \forall\, x \in \Omega^- \\ \phi(\mathbf{x}) > 0 & \forall\, x \in \Omega^+ \end{cases} \tag{3.4}$$

where Ω^- indicates the region inside the interface and Ω^+ the region outside the interface as illustrated in Figure 3.9. The simplest implementations of a level set algorithm is to

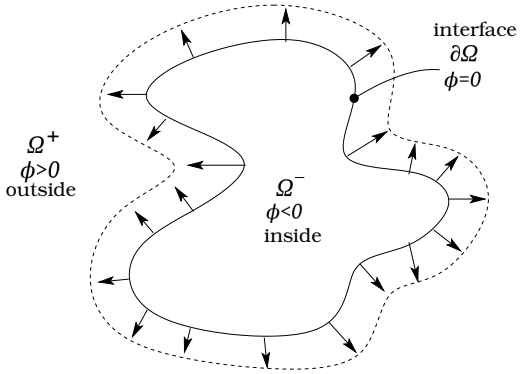

Figure 3.9: Interface Propagation

use the spatial derivatives approximations such as: upwinding, Hamilton-Jacobi Eno, and Hamilton-Jacobi Weno. More details about these methods can be found in [69] and [83].

3.3.1 Building the Displacement Map

At each iteration of the level set, during the propagation of the segmented tumor boundary inverse to the normal direction, ARMSTG saves the points on the evolving interface in a list of point coordinates. Each point in the list contains a link to its previous position in the evolving interface, generating a displacement map. The point coordinates computation entails tracking the displacements $\Delta\mathbf{x}$ for each point $\mathbf{x}$ produced by the level set procedure. ARMSTG uses a Lagrangian formulation for the boundary evolution equation in order to estimate the displacements:

$$\frac{\Delta\mathbf{x}}{\Delta t} = \mathbf{v}(\mathbf{x}). \tag{3.5}$$

The velocity field that moves the boundary (Equation 3.1) is expressed by:

$$\mathbf{v} = a\left(\frac{\phi_x}{\|\nabla\phi\|}, \frac{\phi_y}{\|\nabla\phi\|}, \frac{\phi_z}{\|\nabla\phi\|}\right) \tag{3.6}$$

where each component of $\mathbf{v}$ is the velocity in $x-$direction, $y-$direction, and $z-$direction respectively, a is a constant defined previously, and ϕ_x, ϕ_y, ϕ_z are the partial derivative of ϕ with respect to each coordinate.

For each point ARMSTG assumes the displacement in the $z-$direction equal zero and its velocity components are estimated using the Hamilton-Jacobi Weno method [69, 83].

The displacement map built in this phase is used later during the tumor growth and mass-effect simulation described in Section 3.5.1.

3.4 Sampling and Seeding the Atlas

ARMSTG performs the tumor growth and mass-effect simulation over a set of points representing the problem domain and its boundary. Those points are scattered in the image space representing brain tissue, and serve as force field nodes and integration points for a mesh-free simulation that computes the deformations created by the presence of the tumor (Section 3.5). Figure 3.10 shows a slice from an atlas image with the sampled points in blue and the tumor seed location in red.

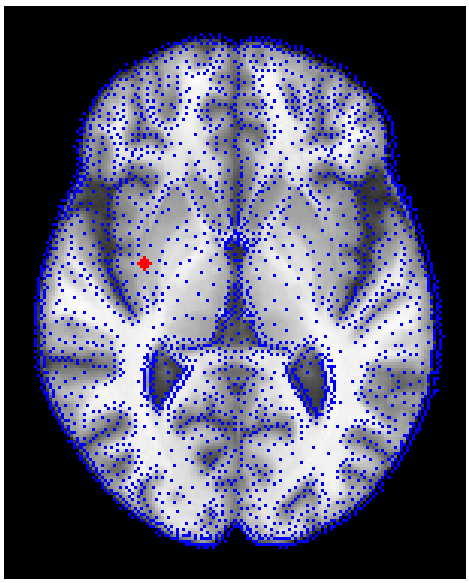

Figure 3.10: Node distribution (blue points), and tumor seed (red point)

The result of this step is a list containing some sampled point coordinates in the atlas space, including some tumor seed points. Each point in the list contains an integer number that identifies the brain tissue type to which it belongs. ARMSTG defines tissue types from 0 to 5 corresponding to: (0) brain tissue, (1) brain boundary, (2) ventricles and sulci, (3) tumor, (4) tumor boundary, and (5) tumor seed points.

Initially, the set of point only belongs to brain tissue, brain boundary, ventricles and sulci, and tumor seed. They are sampled points taken from the atlas space using different sampling methods, plus some added points located at the same position of the tumor level set center. As the simulation runs, the point's labels can change.

3.4.1 Sampling Methods

In this thesis, we implemented three different algorithms for sampling the domain: an adaptive method, a Poisson-Disk sampling, and a regular distributed sampling. For adaptive

sampling, we implemented the algorithm proposed in [103] by Yang *et al.*, which generates nodes with non uniform distribution and spatial density based on the local image variations. The method computes a feature map of the image according to the spatial distribution of the largest magnitude of the second directional directive, then employs the Floyds-Steinberg error-diffusion algorithm [24] to distribute the sampling nodes in the areas with the most image details, *e.g.* using this method the boundaries around ventricles receive the highest node density. The feature map estimated by the method $\sigma(i,j)$ for the pixel i,j is base on this method and is defined by:

$$\sigma(x,y) = \left(\frac{G(x,y)}{A}\right)^{\gamma} \text{ where}$$
$$G(x,y) = \max_{\theta \in [0,2\pi]} |f''_{\theta}(x,y)| \,. \tag{3.7}$$

In Equation 3.7 the parameter A is the largest value of $G(x,y)$ over the image domain and γ is a positive constant set to 1. The feature map is used to compute an indicator function $b(i,j)$:

$$b(i,j) \equiv \begin{cases} 1 & \text{if } \sigma(i,j) \ \geq \ q \\ 0 & \text{otherwise} \end{cases} \tag{3.8}$$

which indicates the presence of a node if $b(i,j) = 1$, the variable q is a threshold introduced as a parameter. The procedure uses the indicator function values to estimate a quantization error for each pixel (i,j) as shown in Equation 3.9. Then the quantization error are diffused at (i,j) in proportions to its four immediate neighbors.

$$e(i,j) = \sigma(i,j) - (2q)b(i,j). \tag{3.9}$$

The Poisson-Disk node generation is based on Dunbar and Humphrey's work in [23]. Poisson-disk distributions mimic the distribution of photo-receptors in a primate eye, and is able to generate nodes with blue noise characteristics for computer graphic applications. This sampling method begins with an initial set consisting of a single point randomly chosen in the atlas image domain. The initial point is added to an output list or processing list. Iteratively the method generates k more points randomly within an annulus surrounding a chosen point from the current set in the processing list. The annulus around the chosen point is limited to a minimum allowable distance between two radius r and $2r$. If the generated point is close (within radius r) to an existing sample in the current processing list, then the point is rejected else the point is added to the processing list. This procedure continues until it is no longer possible to add more points to the processing list.

The last sampling, regular distributed, was performed by selecting points from the atlas image with a constant nodal spacing in x, y and z directions [51]. Figure 3.11 shows an atlas slice with the three different sampling methods implemented in this work. All three methods were applied to the atlas image slice by slice. Then we joined all the sample points

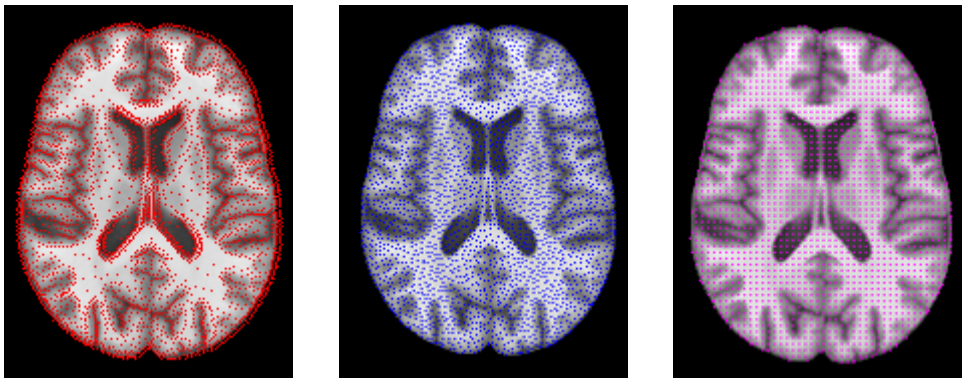

(a) Adaptive (b) Poisson Disk (c) Uniform

Figure 3.11: Three different samplings over an atlas slice: adaptive, Poisson disk, and uniform.

from the slices and added the slice number as a third dimension 3D point samples for each sampling method.

The sample size for the three methods depends on the certain parameters. For the adaptive sampling, the number of nodes generated depends on the threshold q which is also called quantization step size parameter. For Poisson-Disk method the number of nodes generated depends on the minimum distance r where it is allowed to place the next point of the sample. For the uniform sampling, the number of nodes depends on the sampling intervals in the x-direction and y-direction.

3.4.2 Seed Points

In our algorithm, the seed location coincides with the center of the inner contour generated by the level set method evolution (red point in Figure 3.10) once the boundary has collapsed to a minimum size. The size of the seed is a parameter that must be set before the simulation. All the seed points initially share the same location in the atlas image, later they are distributed around the tumor expanding boundary as the simulation runs. The seed points are added to the list containing the generated nodes and are initially labeled as seed points.

3.5 Tumor Growth and Mass-effect Simulation Using a Mesh-free Method

After generating the nodes and seeding the model, the next steps is to perform the tumor growth and mass-effect simulation. The simulation of the deformation in the brain structures produced by the presence of the patient's tumor necessitates the development of a novel mesh-free method that simulates the bio-mechanical evolution of the atlas deformation over time starting from a tumor when it was at the seed size to a tumor fully grown.

This is done by growing the tumor using the inner contours generated by the level set method. Before explaining how this simulation is implemented, let us briefly introduce mesh-free methods.

3.5.1 Mesh-free Methods Overview

Mesh-free methods are an alternative to solve partial differential equation systems without the need for a fixed mesh or grid. One of the big advantage of mesh-free methods over fixed mesh methods is that they can easily deal with large deformations that create non-linear energy function in mesh based method which are hard to stabilize and compute. Mesh-free method also do not require re-meshing, which reduces computational cost significantly. Contrary to mesh-based FEM, mesh-free methods approximate continuous mechanic problems by using a set of scattered nodes that carry the value of the field variables. The methods fit the shape functions representing the problem domain for each point of interest based on a set of local nodes called support domain (see Figure 3.13), thus the shape functions are not limited to mesh geometry as in FEM. They can have different shapes so they can fit closely the geometry of the problem to solve. This advantage allows for more accurate approximations of curve boundaries as illustrated in *e.g.* Figure 3.12, where a curved boundary is approximated in mesh-based methods by straight edges of triangular elements as opposed to a set of scatted nodes in mesh-free methods. The process of node generation in mesh-free methods is simpler than mesh-based as there is no artificial topology imposed on the placement. The nodal distribution is usually not uniform and often denser in areas where the displacement gradients are larger. The domain representation and the shape function are the most relevant differences between mesh-based FEM and mesh-free methods while the system of equations representing the physics of deformation are obviously very similar [6].

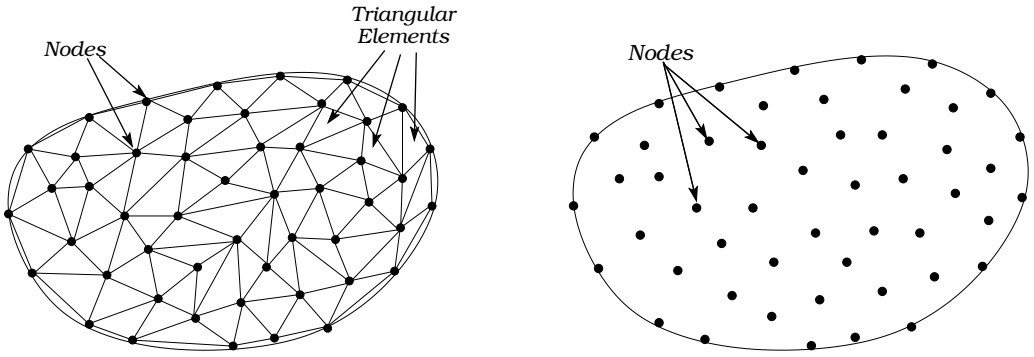

(a) Triangular Mesh (b) Mesh-free representation

Figure 3.12: Triangular mesh vs. mesh-free domain representation.

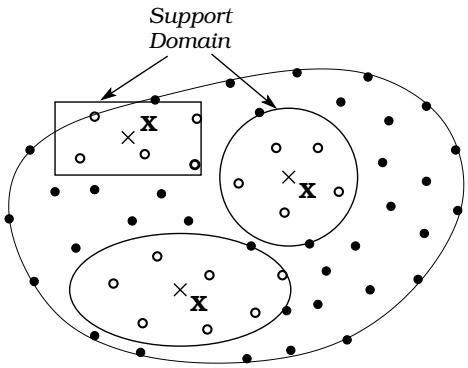

(a) Support Domains

Figure 3.13: Different support domains defined around points $\boldsymbol{x}$. The support domain around a point $\boldsymbol{x}$ is determined by the nodes marked by the donuts ○.

Tumor Growth

The tumor growth simulation starts by growing the seed boundary points using the boundaries generated during the shrinking stage. Each boundary obtained by the level set in Section 3.3 is again re-generated in the opposite direction (outwards) during the simulation. At each iteration, each new point on the tumor boundary moves according to the displacement map saved during shrinking until the original tumor boundary is reached. During the first iterations, the size of the seed should be large enough to shape the first contours without leaving gaps in the boundary. However, as the boundary grows, it is necessary to add new points in order to avoid the creation of gaps.

First, the current tumor boundary points move to their new positions according to the displacement map. Then, at each iteration t_i, the method checks for all the field nodes enclosed within the new tumor boundary and changes their labels to tumor boundary or tumor according to these rules:

1. For each point falling inside of the tumor ARMSTG searches for the closest point in the list of contour points given by the displacement map. If there is another point labeled as a tumor boundary in that location, then the point inside of the tumor is labeled as a tumor point.

2. If there is not any tumor boundary point at the location of the closest point in the displacement map, then ARMSTG displaces the new point falling inside of the tumor to the position of the given point in the displacement map and labeled it as a tumor boundary point.

The tumor growth simulation is carried out in this way during N iterations, where N is the number of contours produced by the level set method described in Section 3.3.

Mass-effect Simulation

As the simulated tumor grows from the seed toward the original tumor segmentation boundary, the displacements propagate to the rest of the atlas field nodes. In this way, the brain structures are deformed according to the tumor progression slowly, avoiding numerical instabilities and converging to stable solutions. ARMSTG estimates the displacement $\boldsymbol{u}$ at every point $\boldsymbol{x} = (x, y, z)$ by interpolating this field variable from neighboring points falling inside a local support domain around the point of interest (Figure 3.13). The following paragraphs describe how the algorithm is implemented.

1. **Domain Representation and Support Domain.** The field nodes representing the problem domain are the list of points generated in Section 3.4. A support domain is defined as a domain in the vicinity of a point of interest that can be or not be a node [50, 51]. ARMSTG computes support domains for all the field nodes in the list of sampled points. Equation 3.10 defines the support domain dimension d_s around a point of interest $\boldsymbol{x}$.

$$d_s = \alpha_s d_c \tag{3.10}$$

   where α_s is the dimensionless size of the support domain which is defined as a scaling of the average nodal spacing d_c. The distance d_c is initially estimated from the average distance of K neighbors around $\boldsymbol{x}$. In our implementation, following similar ideas as [51, 65], we set $\alpha_s = 3.0$ and treated K as a program parameter.

2. **Shape Functions.** Shape functions describe the local geometry of the object at any point of interest $\boldsymbol{x}$. Shape functions are involved in the approximation of the field variable $\boldsymbol{u}$ by:

$$\boldsymbol{u}(\boldsymbol{x}) = \sum_{i=1}^{n_s} \boldsymbol{\phi_i}(\boldsymbol{x})\boldsymbol{u_i} \tag{3.11}$$

   where n_s is the number of nodes sampling the support domain of the point $\boldsymbol{x}$, $\boldsymbol{\phi_i}(\boldsymbol{x})$ and $\boldsymbol{u_i}$ are the shape function and nodal field variable at the ith node. In the proposed mesh-free method the approximation of $\boldsymbol{\phi}_i$ is performed using using Radial Basis Functions (RBF) [11]. We chose the Thin Plate Splines (TPS) RBF because of its simplicity (only requires one parameter *i.e.* an exponent η), and because it produced less singularities than other functions tested during the method evaluation. This is defined as:

$$R_i(\boldsymbol{x}, \boldsymbol{x}_i) = r_i^{\eta} \tag{3.12}$$

   where η and r_i is the Euclidian distance between the point of interest $\boldsymbol{x}$ and its neighbor $\boldsymbol{x}_i$. In this work η was set to $\frac{1}{dc \times dc}$.

3. **Mass and Volume.** One can see the set of sampled points as physical elements carrying on all the simulation variables required to solve the equation system governing its mechanical behaviour. Two of these variables are mass and volume.

ARMSTG estimates the mass m and the volume V for each point of the list of nodes by assuming a constant mass at each point in the neighbourhood $\boldsymbol{x}$ that does not change during the simulation. The interpolation function is similar to the one defined by Müller *et al.* [65, 66] and is defined by:

$$W(r,h) = \begin{cases} \dfrac{315}{64\pi h^9}({d_s}^2 - r^2) & \text{if} \quad r \leq h, \\ 0 & \text{if} \quad \text{otherwise} \end{cases} \tag{3.13}$$

where r is the distance to the point $\boldsymbol{x}$ and d_s is the support domain dimension defined in Equation 3.10. The volume $V_{\boldsymbol{x}}$ associated with the point $\boldsymbol{x}$ is defined as:

$$V_{\boldsymbol{x}} = \frac{m_{\boldsymbol{x}}}{\rho_{\boldsymbol{x}}}, \quad m_x = s{d_c}^3\rho, \quad \rho_x = \sum_{i=1}^{n} m_i w_{xi} \tag{3.14}$$

$$m_{\boldsymbol{x}} = s{d_c}^3\rho, \tag{3.15}$$

$$\rho_{\boldsymbol{x}} = \sum_{i=1}^{ns} m_i w_{xi} \tag{3.16}$$

where
$m_{\boldsymbol{x}}$: is the mass of the point $\boldsymbol{x}$;
$\rho_{\boldsymbol{x}}$: is the density at point $\boldsymbol{x}$;
d_c: is the average distance between $\boldsymbol{x}$ and all its neighbors in the support domain;
ρ: is the material density;
s: is the scaling factor chosen such that ρ_x is close to ρ;
ns: is the number of nodes conforming the support domain of $\boldsymbol{x}$; m_i: is the mass of the node x_i, $i = 1, ..., n$ in the support domain of $\boldsymbol{x}$;
and $w_{xi} = W(\|x - x_i\|, d_s)$.

4. **Bio-mechanical Model** The implemented mesh-free formulation is similar to the model for soft tissue deformation for surgical simulation described in [8, 39, 60]. These approaches introduce Total Lagrangian Explicit Dynamic algorithm (TLED) which differs from the common updated Lagrangian formulation as it calculates the system of equation variables with reference to the initial configuration instead of the previous system configuration [6]. The TLED algorithm formulate the system of equations of the mesh-free radial point interpolation method by computing the force associated to each support domain [39] and is defined as:

$$\overset{t}{_0}\mathbf{F} = \int_{{}_0V} \overset{t}{_0}\mathbf{B}_L^T \overset{t}{_0}\mathbf{S} \mathrm{d}^0V \tag{3.17}$$

where $\overset{t}{_0}\mathbf{B}_L$ is the full strain-displacement matrix and $\overset{t}{_0}\mathbf{S}$ is the second Piola-Kirchoff stress vector. Equation 3.17 is solved by numerical integration applied over the set of

nodes. In the notation, the left superscript represents the current time or iteration and left subscript represents the time of the reference configuration which in this case is 0 (initial configuration).

The strain-displacement matrix is defined as:

$$\begin{array}{rcl} {}^{t}_{0}\mathbf{B}_{L} & = & [{}^{t}_{0}\mathbf{B}^{(1)}_{L}, {}^{t}_{0}\mathbf{B}^{(2)}_{L}, \ldots, {}^{t}_{0}\mathbf{B}^{(n)}_{L}], \\ {}^{t}_{0}\mathbf{B}^{(i)}_{L} & = & \mathbf{D}'{}^{t}_{0}\mathbf{X}^{T} \end{array} \tag{3.18}$$

where $\mathbf{D}$ is the shape function derivatives matrix and ${}^{t}_{0}\mathbf{X}$ is the deformation gradient computed from the shape derivatives matrix and the nodal displacements $\boldsymbol{u}$, *i.e.* ${}^{t}_{0}\mathbf{X} = \mathbf{D}'{}^{t}\boldsymbol{u} + \mathbf{I}_3$, $\mathbf{I}_3$ is a 3×3 identity matrix.

The second Piola-Kirchoff stress-vector is defined as [62]:

$${}^{t}_{0}\mathbf{S} = \mu \mathbf{J}^{-2/3}(\mathbf{I}_3 - \frac{1}{3}\mathbf{I}^{t}_{0}\mathbf{C}^{-1}) + \lambda(\mathbf{J} - 1)\mathbf{J}^{t}_{0}\mathbf{C}^{-1} \tag{3.19}$$

where $\mathbf{I}$ is the first invariant of the Deviatoric Right Cauchy Green deformation tensor $\mathbf{C}$, $\mathbf{J}$ is the determinant of the deformation gradient, and μ and λ are the shear and bulk modulus of the material respectively.

The Cauchy Green tensor is the squared of local change in distances due to the deformation and define the state of stress at a point inside a material in the deformed placement or configuration. Invariants of a tensor are scalar functions of the tensor components which remain constant under a basis change [6].

Equation 3.19 is a neo-Hookean model describing a hyper-elastic mechanical behaviour of the brain tissue implemented in ARMSTG's mesh-free method. Table 3.1 contains the values for Young's modulus (E) and Poisson's ratios (v) for different kind of brain tissue considered in this work. These values were taken from Miller *et al.* works in [59, 62], and they are used to calculate the lambda λ and bulk modulus μ involved in Equation 3.19 which are defined by:

$$\lambda = E\frac{v}{(1+v)(1-2v)}, \tag{3.20}$$

$$\mu = E\frac{v}{2(1+v)}. \tag{3.21}$$

Table 3.1: Young's modulus and Poisson's ratio for the constitutive model of the brain tissue. The values in this table were taken from [59, 62]

Tissue	E (Pa)	v
Parenchyma	$3,000$	0.49
Tumor	$3,000$	0.49
Ventricles and sulci	10	0.1

The values in Table 3.1 has been used in several works to simulate brain tissue behaviour [39, 62, 100, 108]. Although CFS has mechanical properties similar to water, the values assigned to Young's modulus (E) and Poisson's ratios (v) in Table 3.1 mimic a soft compressible elastic solid to allow ventricles deform as the the tumor grows. In this way, we are not simulating the properties of the liquid contained into ventricles and sulci, but the brain structures that deform as the intracranial pressure increases due to a tumor presence.

5. **Displacement Calculation.** As in TLED, ARMSTG uses the central difference method derived from Newton's second law to calculate the global nodal displacement defined as:

$$ {}^{t+\Delta t}_{0}\boldsymbol{u} = \frac{-\Delta t^2}{\mathbf{M}} {}^{t}\mathbf{F} + 2{}^{t}_{0}\boldsymbol{u} - {}^{t-\Delta t}_{0}\boldsymbol{u}. \tag{3.22} $$

6. **Boundary Conditions.** At each iteration ARMSTG updates the coordinates of each point in the problem domain by:

$$ {}^{t+\Delta t}\boldsymbol{x} = {}^{t}\boldsymbol{x} + {}^{t+\Delta t}_{0}\boldsymbol{u}. \tag{3.23} $$

   However, the algorithm updates some points according to a preestablished displacement. These points are those corresponding to the tumor boundary that create the displacement map given in Section 3.5, and the points belonging to the boundary of the brain tissue whose displacements are set to 0 during the simulation.

   Points belonging to the brain tissue boundary in the atlas are part of the list loaded at the beginning of the simulation and are identified by their respective labels (Section 3.4). At each iteration, the algorithm checks after computing $\boldsymbol{x}(t + \Delta t)$ if it does not fall beyond the brain boundary. In case that the new coordinate is outside the regions representing brain tissue, then $\boldsymbol{u}(t + \Delta t)$ is re-estimated such that $\boldsymbol{x}(t + \Delta t)$ approximates the position of the closest brain boundary point, and the label of $\boldsymbol{x}(t + \Delta t)$ changes to brain boundary for the rest of the simulation. Figure 3.14 illustrates the brain tissue boundary in one atlas slice.

7. **The Algorithm Scheme.** Figure 3.15 shows a pseudo code of the TLED meshfree method implemented in this thesis. ARMSTG executes the main loop of the algorithm nl times, where nl is the number of contours generated by the level set method in Section 3.3. ARMSTG enumerates the contours from 1 to nl, starting by the inner contour to the outer contour. At each iteration, one contour is reproduced by the displacement of the points at the tumor boundary according to the displacement map, then the displacements are propagated to the rest of the atlas using the meshfree algorithm.

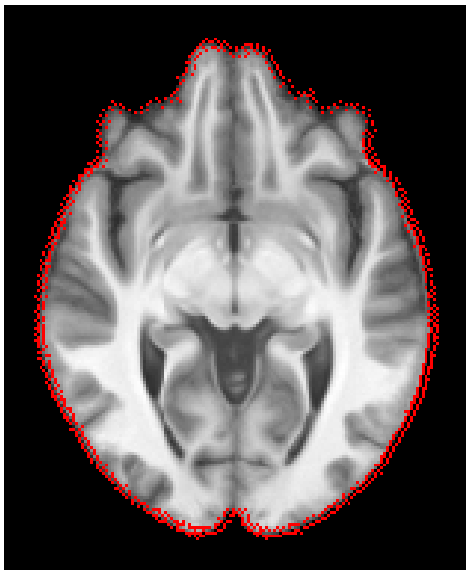

(a) Boundary Points

Figure 3.14: One atlas slice with brain boundary points.

- **Load Points** (nodes, seed, boundary)
- **Load Displacement Map for the Tumor Contour**
- **Initialize Displacement (u = 0)**
- **Compute Support Domain and Derivatives**
  (Radial basis interpolation, thin plate splines)
- **Compute Mass and Volume for Each Suport Domain**

Main Loop

- **Compute Deformation Gradients (X) and Stiffness Matrix S**
- **Compute Forces (F) for Each Support Domain**
- **Estimate Individual Forces for Each Point**
- **Apply Boundary Conditions and Grow the Tumor**
- **Update Displacements**

Keep in the Loop Until Reaching the Tumor Segmentation Boundary

Figure 3.15: Mesh-free algorithm.

3.6 Deformable Registration

The result of simulating the tumor growth and mass-effect mechanics is an image containing the patient's tumor in the atlas space. If successful, the deformed brain structure in the atlas will be similar to the patient's image. However, each patient image contains some other features that distinguish it from a standard atlas *e.g.* brain shape. Hence, it is necessary to apply a deformable registration algorithm to adjust the atlas deformation by

bringing some other particular shape features from the patient's image to the atlas space. This is the last stage of our method for which we used a deformable registration method based on a diffeomorphic Demons algorithm [41, 91, 95].

In a similar way that we carried out the segmented tumor registration to the atlas space 3.2, in this stage we applied the diffeomorphic Demons algorithm over binary images representing the brain tissues of the patient and the atlas with tumor (see figure 3.16), instead of the patient and deformed atlas directly. The registration of binary images instead of intensity images gives better results since the algorithm does not have to deal with the irreconcilable intensity differences between the source and target images. The deformation field obtained from registering the binary images of the patient tissue and deformed atlas tissue is then applied to the deformed atlas in intensity scale.

The binary images of the brain tissue for this stage are obtained by the threshold th_1 obtained by STS as shown in Figure 3.2. The procedure can be summarized in the following steps:

1. ARMSTG uses STS to obtain the threshold th_1 from both the patient image and the deformed atlas with tumor.

2. The respective thresholds for each image are applied, obtaining in this way binary images of the brain tissue as the illustrated in Figure 3.16.

3. ARMSTG applies a diffeomorphic Demon registration algorithm to the binary images and saves the generated displacement field.

4. The resulting displacement field, which is represented in a matrix with the same dimension of the atlas image and contains the displacement in x, y and z coordinates, is applied to the intensity atlas image with the tumor using the same procedure explained in Section 3.2. This step is the final result of ARMSTG, and the final intensity images shown in the second column of Appendix A.

3.7 GPU Implementation with CUDA

One can find in the literature some research works [42, 88, 102] that implemented the TLED algorithm presented in [60] using FEM and structural meshes using Graphic Processing Units (GPU). These works use GPU with the purpose of speeding up the algorithm, and improving the accuracy of the method by using larger numbers of structural elements than what is possible using a CPU implementation.

In our implementation, we also took advantage of the high computational power offered by GPU to speed up the mesh-free TLED implementation. The algorithm in Figure 3.15 can be divided in two parts. The first part is conformed by a set of initialization steps such as load points and displacement map, support domain computation, and mass and

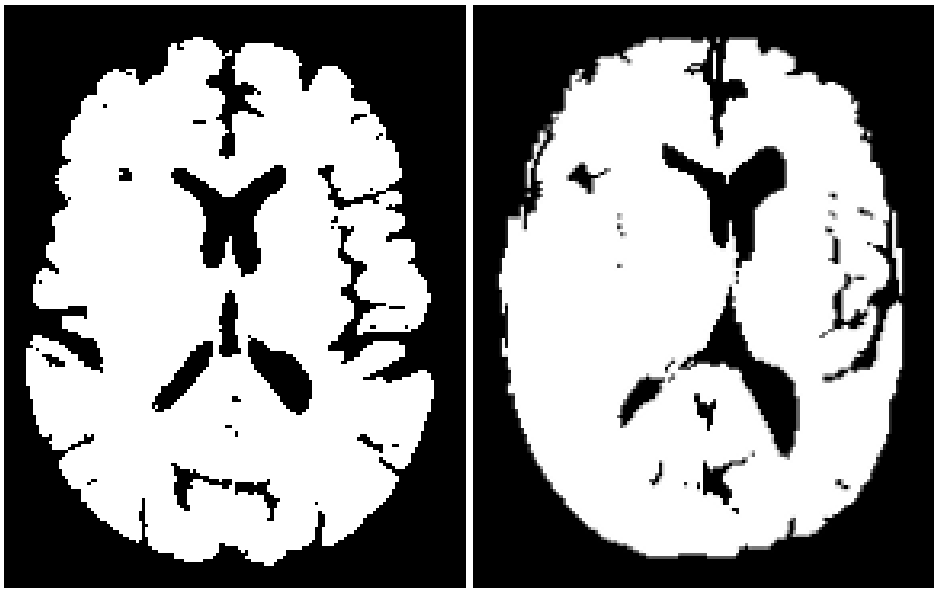

(a) Atlas (b) Patient

Figure 3.16: (a) brain tissue segmented from the atlas, (b) brain tissue segmented from the patient.

volume computations. Although this first part is performed only once in the whole simulation, it requires high computational time because it needs to compute the shape function derivatives, the mass, and the volume estimations which must be done for each node of the problem domain. For this first part, we used six GPU kernels that carried out the following procedures:

1. *Computation of shape functions and derivatives*. This step of the algorithm is accomplished by two GPU kernels, one to built the assembled equation system for each node [50], and another to solve the equation systems using gaussian elimination. The computational time required by this step was considerably reduced with GPU compare to CPU. Once the GPU kernel is launched, the computations are made in parallel and independently for each node.

2. *Mass and volume estimations*. Equations 3.13 to 3.16 are also computed in parallel with the GPU kernels. We designed three kernels, one to compute Equation 3.13 for each node, one to compute mass for each node with Equation 3.15, and one to compute mass with Equation 3.14.

3. *Support domain dimension*. We designed a GPU kernel to compute in parallel each support domain dimension with Equation 3.10.

The second part of the algorithm, shown in Figure 3.15, is computed by a set of iterative steps that include the following operations: deformation gradient, stiffness matrix and

forces computations, boundary conditions and displacement updates. Similarly to Joldes *et al.* [42] and Wittek *et al.* [102], we implemented three main kernels for this second part of the algorithm to perform the computation of deformation gradient, calculation of forces, and the update of displacements in parallel. Additionally, we also designed an extra GPU kernel that is able to speed-up the calculations during the tumor growth stage. The GPU kernel finds possible points inside of the tumor each time that a new contour is recreated during the growth simulation. It computes the distance between individual points in the domain of the tumor center and verifies that this distance is less than a given ratio. If the condition is not fulfilled, the point is immediately considered outside of the tumor boundaries. In this way, the number of points to be considered for more exhaustive computations is reduced to points only inside of the tumor. The distance ratio that is compared is the maximum distance of the tumor center to the points on the current tumor boundary. Figure 3.17 illustrates this mechanism. As explained in Section 3.5.1 ARMSTG generates a new tumor contour at each iteration of the simulation and checks for points falling inside of the current tumor contour. This procedure becomes quite expensive if all the points in the domain are checked. Therefore, we reduced the set of point to be checked to only those falling inside of the sphere of minimum ratio enclosing completely the current tumor contour using the GPU.

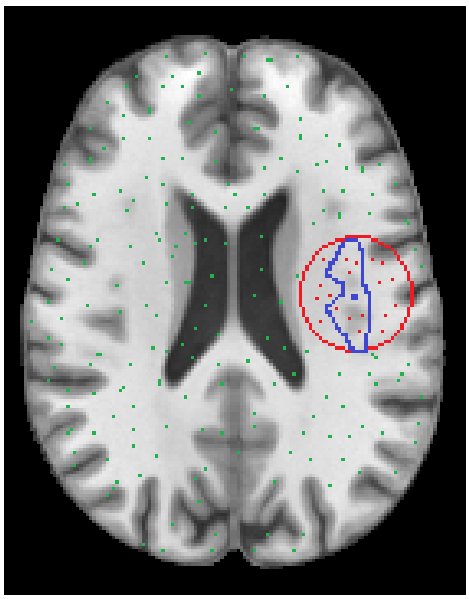

Figure 3.17: Selecting points inside of the tumor. Tumor center in blue, current tumor contour in blue, points selected by the implemented GPU kernel in red, and the rest of the domain points in green.

All the kernels were implemented with CUDA using a NVIDIA graphic card with the specifications given in Table 3.2 which was installed in a workstation with the specifications given in Table 3.3.

Table 3.2: GPU Specifications

NVIDIA GT780 GPU Engine Specifications	
CUDA Cores:	2304
Clock Freq (MHz):	863
Memory Clock (MHz):	2500
Memory Type:	GDDR5
Memory Interface Width:	384 bit
Memory Bandwidth (GB/sec):	188.4
Total Memory:	3072 MB

Table 3.3: CPU Specifications

Intel Core i7-7490K Specifications	
Number of Cores:	4
Clock Freq (GHz):	4.00
Memory Clock (MHz):	2500
Memory Type:	DDR3
Total Memory:	32768 MB

Chapter 4

Evaluation of the ARMSTG Algorithm

In this chapter, we present experimental results that evaluate how the proposed atlas to patient registration method performs under various conditions and cases. We evaluated ARMSTG's performance against three non-linear registration algorithms: diffeomorphic demons registration [41, 91, 95], the Automatic Registration Toolbox (ART), and the symmetric diffeomorphic image registration algorithm with cross-correlation SyN [4]. The last two methods were ranked as the best non-linear registration method for brain MRI in [46]. We also evaluated the influence of various ARMSTG parameters on the method accuracy, the benefit of our tumor growth simulation model based on the real shape of the tumor, and the method's computational performance on standard CPU and on parallel GPU hardware using CUDA.

The experiments were conducted over twelve MRIs taken from the MICCAI'S 2013 Multimodal Brain Tumor Segmentation (BRATS) challenge training data set [58]. The experiments yielded several registered images whose similarities to the respective original MRIs were measured using a metric based on a distance field. Before presenting the experimental results, we will first introduce the data set and the similarity metric used in this work. Then, in section 4.3, we will describe each experiment and their results, and we will also discuss the pros and cons of the evaluated methods.

4.1 MICCAI's Data Set

We selected twelve cases from the thirty multi-contrast MRIs of the training data set provided by MICCAI's BRATS challenge [58], these include ten high-grade and two low-grade glioma cases. The data set contains T1, T2, FLAIR, and post-Gadolinium T1 MRI sequences of size $216 \times 160 \times 176$ voxels for each patient. All volumetric images in the BRAT's data set are already linearly co-registered to the T1 contrast image, skull stripped, interpolated at 1 mm isotropic resolution, and are already manually segmented by a human expert as a gold standard. The only criterion considered for the data selection was the completeness of the manually segmented brain tissues. We discarded cases where the brain parenchyma appears incomplete from the training data set. The 12 selected images were

aligned to the sagittal plane of the image using an algorithm proposed by Liu and Collins [104].

4.2 Similarity Metric

In order to assess the similarity between the registered atlas images to a patient case, we computed a metric based on a distance field. A distance field is a collection of distances between each point of an image to the closest point of any object within the domain [43]. Figure 4.1 is an example of a distance field. The procedure applied to obtain a distance field is commonly called the distance transform $\mathcal{D}$, *e.g.* the image in Figure 4.1 was obtained with an Euclidian distance transform, *i.e.* the distance of each pixel to the closest non-zero pixel in the image is estimated with the equation of the Euclidian distance.

Let $\mathbf{I}_a$ and $\mathbf{I}_b$ be two binary images in $\Re^3$ containing the ventricle boundaries of the atlas and the patient respectively, then we define the similarity metric S between these two images as an integration mapping $\mathcal{S} : \Re^3 \mapsto \Re^1$ as:

$$\mathcal{S}(\mathbf{I}_a, \mathbf{I}_b) = \mathbf{I}_a \odot \mathcal{D}(\mathbf{I}_b) \tag{4.1}$$

where $\mathcal{D}$ is the mapping $\mathcal{D} : \Re^3 \mapsto \Re^3$ and $\odot$ is the integration operator over all image set, which is defined as:

$$\mathbf{A} \odot \mathbf{B} = \sum_{i,j,k}^{M,N,O} A(i,j,k)B(i,j,k) \tag{4.2}$$

where $\mathbf{A}$ and $\mathbf{B}$ are 3D matrices of size (M, N, O).

We computed Equation 4.1 with the following steps:

1. Segment ventricles from the atlas binary images of the brain tissue registered to the patient images in Section 3.6, and the binary image of the patient brain tissue;

2. Extract boundaries of the segmented ventricles from both the atlas and patient ventricle images (this step yields two binary images as shown in Figure 4.2);

3. Compute the distance transform $\mathcal{D}$ of the patient ventricle boundary. In this work we used Euclidian distance transform similar to the example shown in Figure 4.1;

4. Multiply point to point the Euclidian distance transform image to the binary image of the ventricle boundaries in the atlas, the result of this step is an image containing only the distance of the atlas ventricles boundary to the patient ventricle boundary;

5. Compute the summation of the resulting image's voxels.

The ventricle segmentation was semi-automatically performed over the brain tissue masks obtained in the last step of ARMSTG, Section 3.6, (see Figure 3.16). In the image we first manually selected some points in the ventricles, then we extract the largest connected component to these points. The largest connected component mostly corresponds

0	0	0	0	0	0	0
0	0	0	1	0	0	0
0	0	1	0	1	0	0
0	1	0	0	0	1	0
0	0	1	1	1	0	0
0	0	0	0	0	0	0

(a) Binary Image

2.8284	2.2361	1.4142	1.0000	1.4142	2.2361	2.8284
2.2361	1.4142	1.0000	0	1.0000	1.4142	2.2361
1.4142	1.0000	0	1.0000	0	1.0000	1.4142
1.0000	0	1.0000	1.0000	1.0000	0	1.0000
1.4142	1.0000	0	0	0	1.0000	1.4142
2.2361	1.4142	1.0000	1.0000	1.0000	1.4142	2.2361

(b) Distance Transform

Figure 4.1: (a) original binary where a value of 1 represents an edge pixel and zero a background pixel. (b) distance transform where each value represents the distance to the closest edge pixel in mm.

to the image's ventricles. Then, we cleaned up the resulting image to eliminate any part that didn't belong to the ventricles. Figure 4.2 shows some examples of the segmented ventricles for a patient data and for an atlas.

4.3 Experimental Results

We designed a series of experiments in order to evaluate the accuracy and performance of ARMSTG. The experiments will be presented in five groups: the first group evaluates the effect of sampling sizes, some parameters of the level set, and the time-step parameter of the mesh-free simulation. The second group compares the three sampling methods explained in Section 3.4.1. The third group compares our tumor growth simulation model based on the real tumor shape *vs* a spherical tumor growth model. The fourth group compares ARMSTG with three other non-linear deformation registration methods. The fifth group analyzes the computation performance of the algorithm for a CPU based implementation and its parallel implementation using CUDA on a GPU.

4.3.1 Parameter Evaluations

Effect of the sampling size

As mentioned in Section 3.4.1, the number of samples generated by the three mesh-less sampling methods depends on certain control parameters for the distance between sample

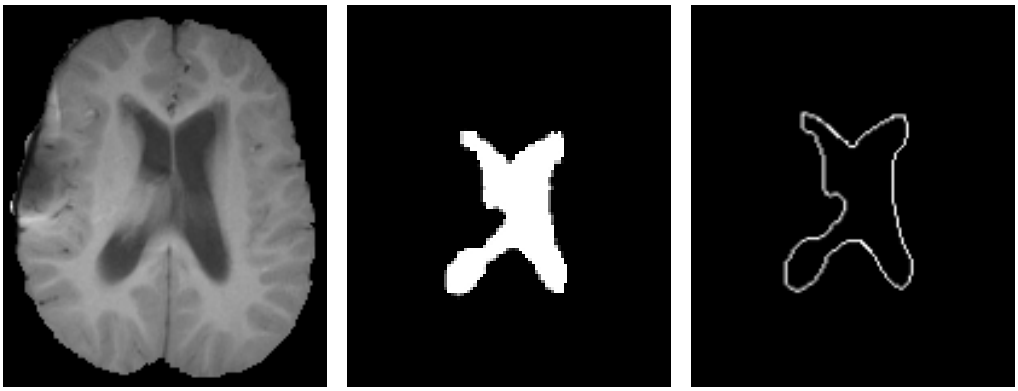

(a) Patient Image (b) Ventricles (c) Boundary

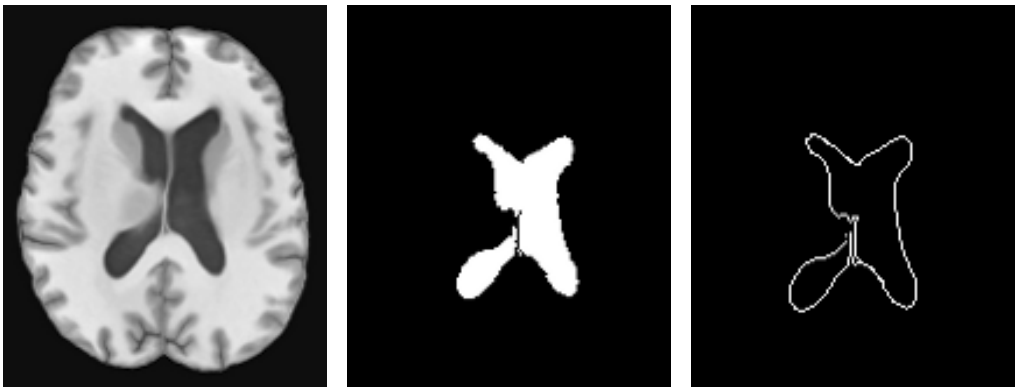

(d) Registered Atlas Image (e) Ventricles (f) Boundary

Figure 4.2: Ventricle Segmentation of a patient and registered atlas images.

points [23, 51, 103]. Due to how the control parameters between methods affect the sample spacing, it was not possible to match the exact sample size between the three methods. We selected a set of different values for these parameters as described in Table 4.1 in order to generate set for our statistical analysis. For the adaptive sampling method, the sample size depends on a quantization step-size q that is inversely proportional to the number of samples generated. For the Poisson-disk sampling method, the sample size depends on the minimum ratio or distance r at which the points can be placed from each other. For the uniform sampling method, the sample size depends on the constant spacing parameter s.

For our statistical tests to evaluate the influence of the sample size, we computed a total of 108 atlas to patient registrations for each sampling method, *i.e.*, 3 sampling instances $\times$ 12 cases $\times$ 3 control parameter value in order to evaluate the influence of the sampling size on the results. Each sampling method with the different sizes was separately analyzed using Kruskal-Wallis test [85] in order to detect if there were any differences in choosing specific values.

Kruskal-Wallis test is a nonparametric ANOVA statistical method that analyzes the variance for one-way classification or one-factor experiments by ranks. This test is applied for small samples when the data do not meet the normality assumption of its homologous

Table 4.1: Different sample sizes for each sampling method.

Sampling Method	Parameter	Value	Sample Size
Adaptive	Quantization step-size (q)	0.004	67,767
		0.01	157,268
		0.25	208,582
Poisson-disk	Minimum distance (r)	2.0	222,881
		3.0	41,831
		4.0	61,041
Uniform	Spacing (s)	3.0	166,132
		4.0	96,214
		5.0	63,848

parametric test one-way ANOVA. This test is applied to test whether the samples come from the same distribution. Like most non-parametric tests, Kruskal-Wallis is performed over ranked data.

We generated groups of twelve observations, one per patient, for each parameter value for each individual sampling method. Tables 4.2 to Table 4.6 and Figures 4.3 to 4.5 summarize the results of the Kruskal-Wallis test for each individual sampling method. The mean rank of each group is represented by a small circle and their respective error interval represented by a line extending out from the circle.

Table 4.2: Kruskal Wallis ANOVA table to evaluate the sample size effect over ARMSTG's performance with adaptive sampling.

Source	SS	df	MS	χ^2	Prob $> \chi^2$
Columns	30.5	2	15.25	0.27	0.8716
Error	3,854.5	33	116.803		
Total	3,885	35			

In the ANOVA tables produced by Kruskall-wallis tests the first row called *Columns* contains the estimated values to measure the sum of squares of the differences between each group mean and the total mean of the whole data. The second row *Error* contains the estimated values to measure the sum of squared differences between each data and its respective group means. The third row *Total* measures the sum of squared differences between each data points and the mean of the whole data. The value SS is the respective result of the sums of squares for each measure, and df is the freedom degree which is equivalent to the number of data point taken into account in the statistic calculation minus 1. The Kruskal-wallis test replaces the classical F-statistic used in one-way ANOVA by a χ^2 (chi-square) statistic. Thus, Prob $> \chi^2$ is the $p-$value that measures the significance of the statistic.

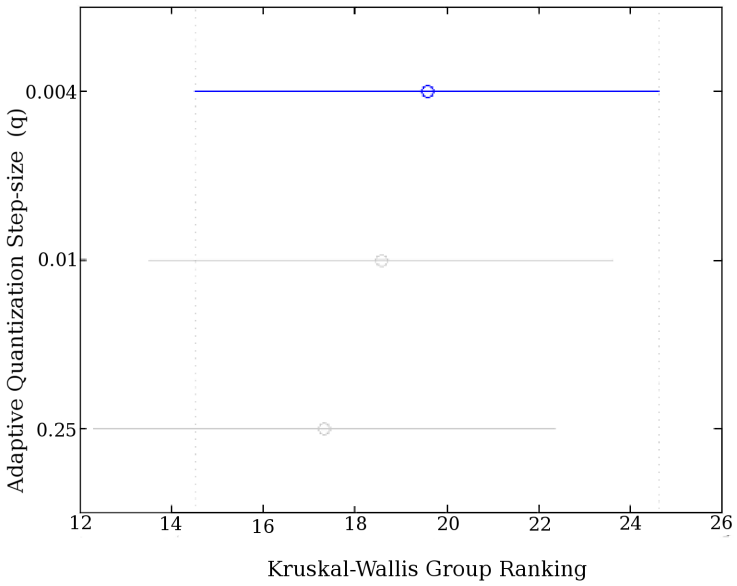

Figure 4.3: Pairwise comparison of mean ranks to evaluate the sample sizes effect over ARMSTG's performance with adaptive sampling.

Table 4.3: Mean distances between ventricles of the twelve patient's images and the registered atlases obtained with ARMSTG using adaptive sampling and three different sample sizes.

ARMSTG Quantization-step q
For Adaptive Sampling

q	Size	Mean of $\mathcal{S}$ Metric
0.004	67,767	9,691.23
0.01	157,268	9,673.74
0.25	208,582	9,317.92

Table 4.4: Kruskal Wallis ANOVA table to evaluate the sample size effect over ARMSTG's performance with poisson-disk sampling.

Source	SS	df	MS	χ^2	Prob $> \chi^2$
Columns	1,590.62	2	795.308	12.24	0.0022
Error	3,349.38	36	93.038		
Total	4,940.00	38			

Similar to other non-parametric statistical test, Kruskal-wallis is performed over ranked data. The statistical procedure followed by this test first arranges the data within each group such that the smallest value gets a rank of 1, the next smallest gets a rank of 2, and so on.

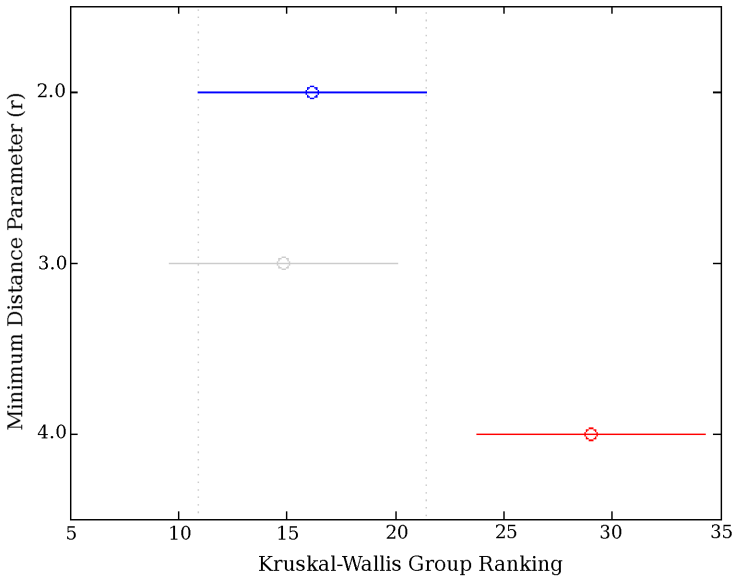

Figure 4.4: Pairwise comparison of mean ranks to evaluate the sample sizes effect over ARMSTG's performance with poisson-disk sampling.

Table 4.5: Mean distances between ventricles of the twelve patient's images and the registered atlases obtained with ARMSTG using Poisson-disk sampling and three different sample sizes.

ARMSTG Minimum Distance r
For Poisson-disk Sampling

r	Size	Mean of $\mathcal{S}$ Metric
2.0	222,881	9,681.530
3.0	41,831	9,224.632
4.0	61,041	33,220.210

Table 4.6: Kruskal Wallis ANOVA table to evaluate the sample size effect over ARMSTG's performance with uniform sampling.

Source	SS	df	MS	χ^2	Prob $> \chi^2$
Columns	1,082	2	541.00	9.75	0.0076
Error	2,803	33	84.94		
Total	3,885	35			

Figure 4.3 to Figure 4.5 and so all the pairwise comparison of mean rank plots in this documents illustrates the differences of mean ranks between the evaluated groups. In these

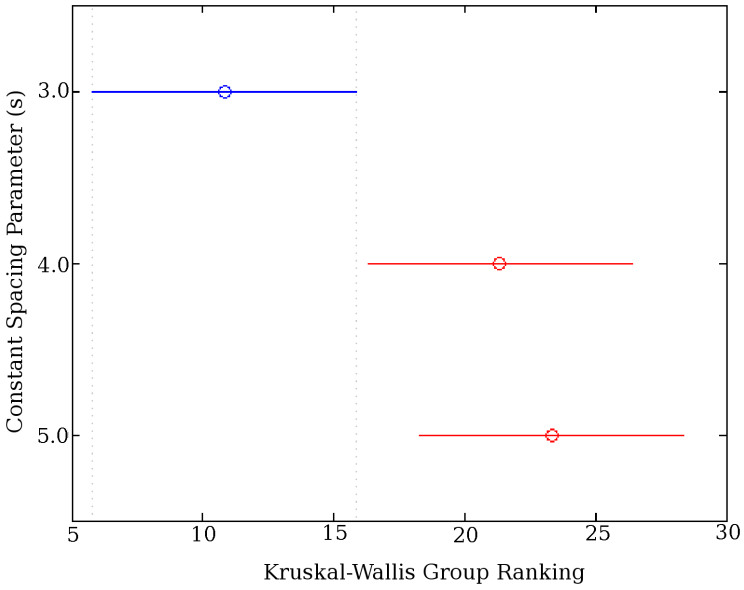

Figure 4.5: Pairwise comparison of mean ranks to evaluate the sample sizes effect over ARMSTG's performance with uniform sampling.

Table 4.7: Mean distances between ventricles of the twelve patient's images and the registered atlases obtained with ARMSTG using uniform sampling and three different sample sizes.

ARMSTG Spacing s For Uniform Sampling		
s	Size	Mean of $\mathcal{S}$ Metric
3.0	166,132	9,030.57
4.0	96,214	33,293.80
5.0	63,848	49,336.16

figures the x-axis represents the compared groups, and the y-axis represents the mean ranks of groups.

The $p-$ value of 0.8716 in Table 4.2 is large enough to reject the hypothesis of a difference between the distribution of the observations for the adaptive sampling algorithm with a 5% significance level; while the $p-$ value obtained for Poisson-disk and uniform sampling algorithms in Tables 4.4 and 4.6 shows that at least one group of observations with the different sample sizes dominates over the others for each test. In Figure 4.3, Figure 4.4, and Figure 4.5 one can observe that ARMSTG performed better using small ratios with Poisson-disk sampling, and a spacing of $s = 3$ using uniform sampling.

Effects of the Seed Size

The seed is the starting point of the tumor growth simulation. In Section 3.4, we mentioned that we located p seed points at the center of the inner tumor contour. The purpose of having p points is to allow the initialization of the growth simulation to pass from the seed location to the first tumor contour and also to preserve the mass for the mass-effect simulation. Commonly, the first contours of the tumor only contain a few points because the level set procedure is applied inwardly until there is not enough internal points to generate another contour in the image. Therefore, the number of seed points p could be set to a small number of points. We tested three values for three parameter values 3, 7 and 10. In our experiments, we found that larger number of seed points frequently created singular solution when computing the RBF interpolating function. This is because the larger the number of seed points at the same location, the greater probability of singular linear system where the determinant is close to zero.

In order to analyze the effect of the seed size in ARMSTG's results, we generated 108 observations, *i.e.* 3 seed size values $\times$ 3 samplings $\times$ 12 patient's cases. The results were analyzed using the Friedman test [27].

The Friedman test is a non-parametric statistical test for testing the difference between several samples. The test ranks each row (block) from low to high separately, then considers the values of the ranks by columns (groups). The null hypothesis evaluated by this test is that the column effects are all the same against the alternative that they are not all the same [54].

In this context the observations were organized in 36 rows grouped by sampling method, *i.e.* 3 groups of 12 patient's MRI in each one, and three columns, each one representing a seed size value. An ANOVA analysis of this experiment is summarized in Table 4.8. Figure 4.6 shows the pairwise comparison of the mean ranks of the three groups as a function of the three seed size values, from top to bottom for the number of seed points equal to: 3, 7, and 10.

Table 4.8: Friedman ANOVA table to evaluate the effect of the seed size over ARMSTG's performance

Source	SS	df	MS	χ^2	Prob$> \chi^2$
Columns	126.7	2	63.361	1.14	0.565
Iterations	12.9	4	3.236		
Error	11,511.3	99	116.276		
Total	11,651	107			

In Table 4.8 a $p-$ value of 0.65 means that there were no significant differences in ARMSTG's performance using either seed size within a 5% of significance level, and Figure 4.6 shows the mean values obtained at evaluating ARMSTG with the different seed sizes very close to each other.

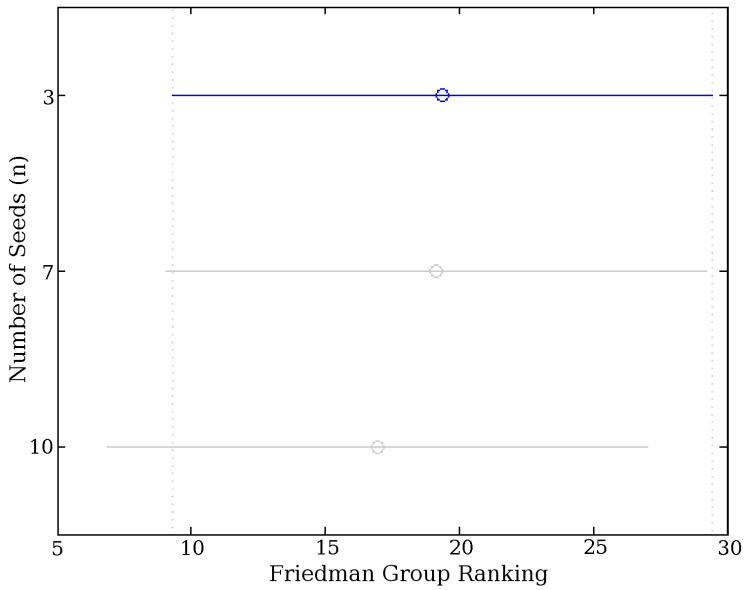

Figure 4.6: Pairwise comparison of mean ranks to evaluate the effect of the seed size over ARMSTG's performance.

Table 4.9: Number of tumor contours generated by the level set with different iteration number for each patient's cases.

Iterations/Patients	1	2	3	4	5	6	7	8	9	10	11	12
2	24	21	34	32	37	40	38	29	35	37	25	47
4	12	11	17	16	19	20	19	15	18	19	13	24
6	8	7	12	11	13	14	13	10	12	13	9	16
8	6	6	9	8	10	10	10	8	9	10	7	12

Effect of the Level Set Parameters

We evaluated the effect of two parameters required by the level set method described in Section 3.3. The first parameter is the number of iterations for the level set and second parameter is the constant value a in Equation 3.2. The number of iterations has a direct effect on the number of tumor contours generated by the level set. This number determines the number of times that the advancing front is updated until it reachs the center of the tumor (see Section 3.3). We selected four different values for this parameter: 2, 4, 6, and 8. Table 4.9 lists the number of tumor contours generated for each iteration number for each patient's cases.

The four values for the iteration number of the level set were tested using ARMSTG with the different sampling methods. Hence, we generated a total of 144 observations for this experiment, *i.e.*, 4different values $\times$ 3sampling methods $\times$ 12patient cases. The results were analyzed using Friedman test [27]. The ANOVA analysis of this test is summarized

in Table 4.10, and the pairwise comparison of the mean values for the four groups is shown in Figure 4.7. The respective mean ranks are shown from top to bottom in the same order.

Table 4.10: Friedman ANOVA table to evaluate the effect of the iteration number of the level set on ARMSTG's performance.

Source	SS	df	MS	χ^2	Prob $> \chi^2$
Columns	243.7	3	81.241	1.24	0.7426
Iterations	8.4	6	1.407		
Error	2,783.8	132	207.453		
Total	3,036	141			

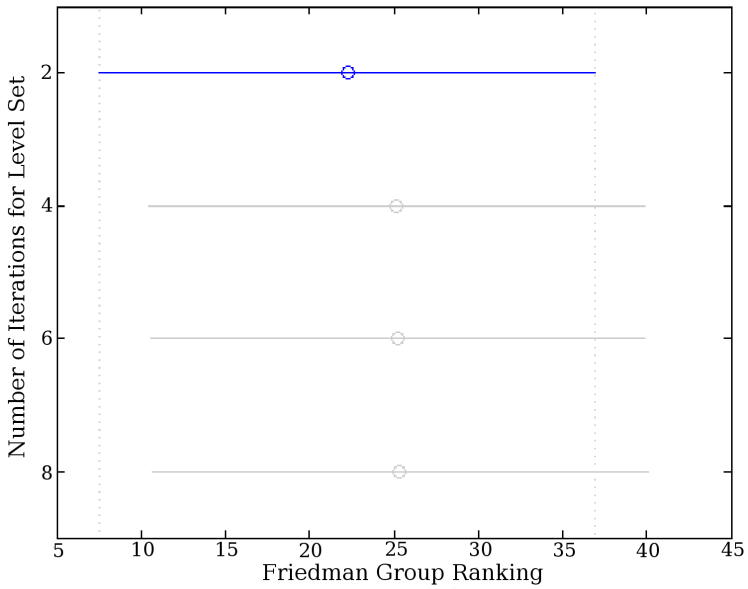

Figure 4.7: Pairwise comparison of mean ranks to evaluate the effect of the level set iteration number over ARMSTG's performance.

In the same way, we also evaluated the effect of the parameter a on the level set. For this purpose, we chose three different values for this parameter: 0.1, 0.5, and 0.9. Contrary to the number of iterations, these three values did not cause any observable variation in the number of contours generated by the level set. In this experiment, 108 observations were produced, *i.e.*, 3 different values $\times$ 3 sampling methods $\times$ 12 patient cases. The ANOVA analysis generated by Friedman test is summarized in Table 4.11 and the mean value comparison for the three parameter's values are shown in Figure 4.8.

The two $p-$ values in Table 4.10 and Table 4.11 of 0.74 and 0.99 indicate that both the number of iterations and the level set a parameter do not have any effect over ARMSTG's performance at a 5% significance level.

Table 4.11: Friedman ANOVA test to evaluate the effect of the constant level set parameter a on ARMSTG's performance.

Source	SS	df	MS	χ^2	Prob $> \chi^2$
Columns	0.7	2	0.333	0.01	0.997
Iterations	0.9	4	0.229		
Error	11,600.4	99	117.176		
Total	11,602	105			

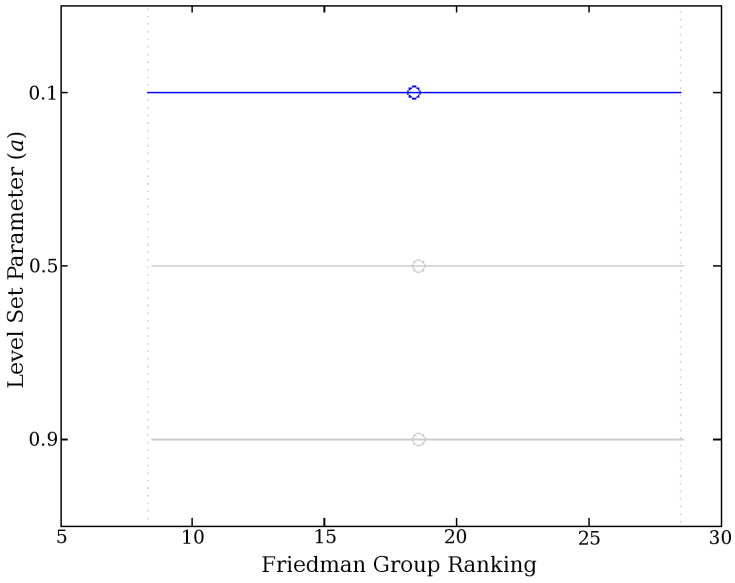

Figure 4.8: Pairwise comparison of mean ranks to evaluate the effect of the level set parameter a over ARMSTG's performance.

Effect of the Simulation Time Step (Δt)

In this experiment, we analyze the effect of the the simulation time step involves in Equation 3.23. The time step is related to the dilation wave speed across the material, and produces stable results only under certain critical value Δt_c [39]. In this thesis, we evaluated 6 different values for these parameter: 0.0025, 0.005, 0.01, 0.05, 0.09, and 0.13. In total, 216 observations were generated for this analysis, *i.e.*, 6 parameter values $\times$ 3 samplings $\times$ 12 patient cases. The analysis was performed with the Friedman test. Table 4.12 contains a summary of the ANOVA analysis, and Figure 4.9 shows the pairwise comparison of the mean values in the same order.

The $p-$ value of Table 4.12 means that Δt affected ARMSTG's performance. At least two observation groups are different between each other at 5% significance. In Figure 4.9 one can see that ARMSTG yielded better results with Δt less than 0.05. This observation is corroborated by Figure 4.10 where ARMSTG's performance with the three different sampling methods and ($\Delta t \leq 0.05$) looks very similar and very disparate for ($\Delta t > 0.05$).

Table 4.12: Friedman ANOVA table to evaluate the effect of the simulation time step on ARMSTG's performance.

Source	SS	df	MS	χ^2	Prob $> \chi^2$
Columns	12,706.9	5	2541.39	34.48	1.91e-06
Iterations	5,027.4	10	502.74		
Error	54,121.6	180	300.68		
Total	71,856	197			

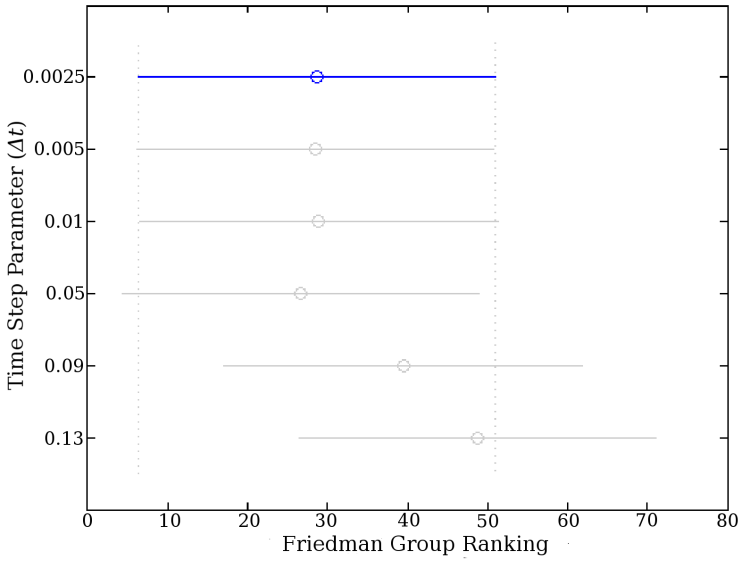

Figure 4.9: Pairwise comparison of mean ranks to evaluate the effect of the simulation time step Δt over ARMSTG's performance.

Discussion

The Kruskal-Wallis test is applied in order to evaluate the null hypothesis that all observations, organized by columns (groups), arise from the same distribution. When Kruskal-Wallis null hypothesis is rejected, then one can conclude that at least one group is different from the others, and at least one group is stochastically dominant over one or more groups [47].

In our first experiment, we analyzed the effect of the sample size for the various sampling strategies, where one can observe that the $p-$ value of the ANOVA analysis in Table 4.2 did not reject the null hypothesis for adaptive sampling at 5% significance level. One can not conclude that the three groups corresponding to the registration results of the method with adaptive sampling, and with the three different sampling sizes evaluated for this case were different, and came from different distributions. Figure 4.3 and Table 4.3 show that the mean distances of the ventricles for the twelve MRI cases and the registered atlases with the different sample sizes were very similar.

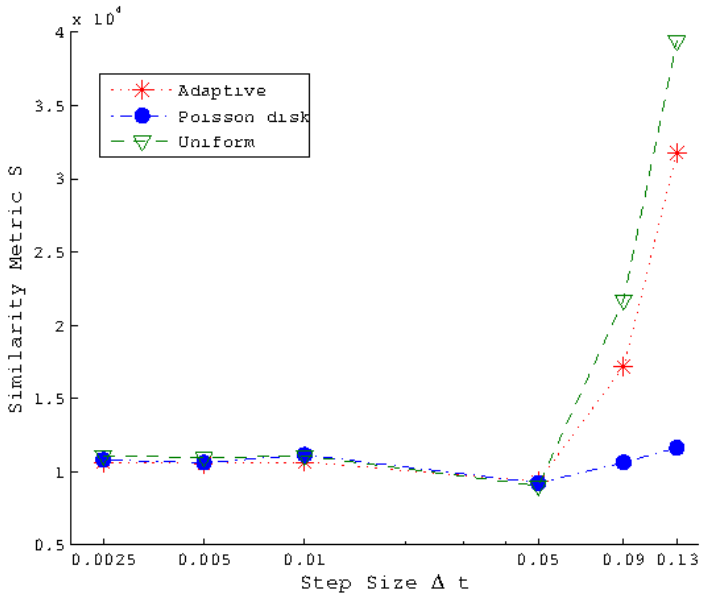

Figure 4.10: ARMSTG's performance with different time step Δt. The similarity metric is in mm.

According to Tables 4.4 and 4.6, the same conclusion cannot be made for the Poisson-disk and uniform samplings. The Kruskal-Wallis test rejected the null hypothesis for both samplings, which means that the sample size yield significant differences in both sampling strategies. Figure 4.4 and Figure 4.5 illustrate the pairwise mean rank differences between the groups. In the case of the Poisson-disk sampling, one can observe that the third group corresponds to the largest of the three maximum ratios evaluated in this test, and is significantly different to the other two groups. In Table 4.5 one observe that this group obtained the worst mean distance in comparison to the other two groups. In the case of the uniform sampling, the first group corresponds to the minimum spacing evaluated in this experiment and is significant different to the other two groups which had larger mean distances than the first. This can also be seen in Table 4.7. Evaluating smaller spacing values for uniform sampling was not possible because of the computational intractability of large sample size.

From these results, one can conclude that the spacing between samples influences the ARMSTG performance more than the sample size. This can be the reason why there is no significant difference for the adaptive sampling case with the sample sizes. Independently of the sample size, this sampling tends to take points very close between each other where features of the image are located *e.g.* ventricle or sulci boundaries. Contrary to this, the other two sampling methods take samples with a minimum ratio or with a constant spacing, controlling in this way the distance between samples.

Other parameters analyzed in this thesis were the seed size, the iteration number of the level set, and the constant a that multiplies the velocity in Equation 3.2 of the level set. For these evaluations we used the Friedman test to prove the null hypothesis that there were

no differences between groups of the parameter measures under different conditions. Table 4.8, Table 4.10, and Table 4.11 show that for these three parameters, the Friedman test did not rejected the null hypothesis, with $p-$ values of 0.565, 0.7426, and 0.997 respectively. These results mean that these parameters did not have any effect over ARMSTG's performance with the selected values. The mean distances of the tested groups confirm that the results obtained with these parameters are all very close to each other as can be seen in Figure 4.6, Figure 4.7, and Figure 4.8.

With the Friedman test, we also evaluated the effect of the simulation time step Δt over ARMSTG's performance. The $p-$ value $= 1.91 \times 10^{-6}$ yielded by this test rejected the null hypothesis, meaning there was a significant difference between at least two groups of observations for this parameter. Figure 4.9 shows that the mean values of the four first groups are very close to each other. They only differ by the mean value generated for the fifth and sixth time step during the experiment. Observing Figure 4.10, one can say that the method produced stable results under the critical value of $\Delta t_c = 0.05$.

Selected Parameters for ARMSTG

Based on the observations discussed previously and the results presented so far in this Section, we selected the set of parameters shown in Table 4.13 to perform other tests of our method:

Table 4.13: ARMSTG's parameters.

Parameter	Value
Sample size - adaptive	208,582
Sample size - Poisson	41,831
Sample Size - uniform	166.132
Seed Size	10.0
Level set iteration number	2.0
Level set Parameter a	0.3
Simulation time step	0.05

The sample size for each sampling method was selected based on the results in Table 4.3, Table 4.5, and Table 4.7. Among the three tested sample sizes for each sampling method, the selected values yielded the best mean distances for each method, *i.e.* $q = 0.25$ in the third row in Table 4.3 for adaptive sampling, $r = 3.0$ in the second row in Table 4.5 for Poisson-disk, and $s = 3.0$ the first row in Table 4.7 for uniform. In a similar way, despite the non-significant difference, we selected a seed size, an iteration number for the level set, and a value for the parameter a of the level set. For the simulation time step we selected the critical value $\Delta t_c = 0.05$.

4.3.2 Difference Between Samplings

The experiments shown previously evaluated the effect of the sample size over ARMSTG's performance for each sampling method individually. The results of these experiments alone do not allow us to give any conclusion about which method performed better with ARMSTG. The results in Table 4.3, Table4.5, and Table 4.7 intuitively indicates that uniform sampling is the best choice since the first row of the respective table contains the smallest mean distance of all the experiments. In order to test this hypothesis we performed Kruskal-Wallis test over three groups, each one representing each sampling method. The selected groups correspond to the parameters values that yielded the smallest mean distances (Table 4.13). A total of 36 observations, *i.e.*, 3 sampling methods $\times$ 12 patient cases were arranged in three groups: adaptive, Poisson-disk, and uniform. Table 4.14 summarizes the ANOVA analysis result and Figure 4.11 shows the distribution of the means in a difference box plot diagram.

Table 4.14: ANOVA table generated with Kruskal Wallis to compare sampling methods.

Source	SS	df	MS	χ^2	Prob $> \chi^2$
Columns	2.17	2	1.083	0.02	0.9903
Error	3,882.83	33	117.662		
Total	3,885	35			

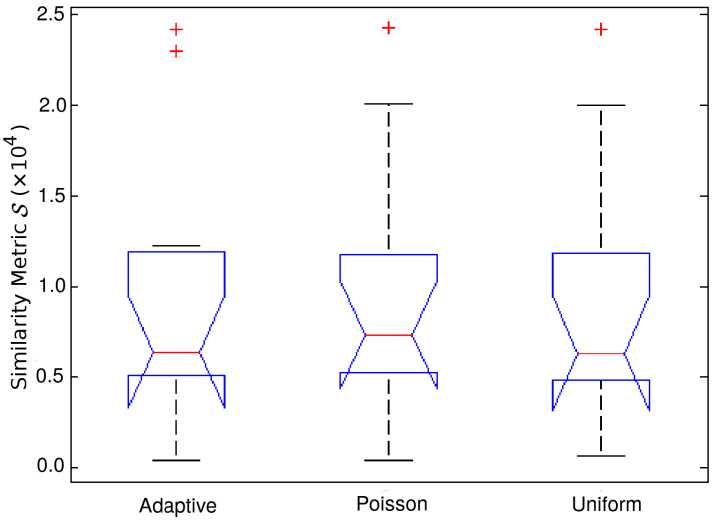

Figure 4.11: Box plot comparison between sampling methods. The similarity metric is in mm

A $p-$ value $=$ 0.9903 in Table 4.14 does not reject the null hypothesis at the 5% significance level. The three groups corresponding to the best results obtained with each sampling come from the same distribution. The box plot in Figure 4.11 shows that the

mean distances for each group are very close, although the range of distance of the group corresponding to adaptive sampling, differs from the other two.

Discussion

Although ARMSTG yielded the smallest mean distance with uniform sampling, one can not conclude that this is the best sampling method. Neither can one conclude that adaptive sampling is the best choice although the results obtained with this method, using different sample sizes, look more consistent than the other methods in Table 4.3. This observation is statistically supported by the comparison between the best groups for each sampling evaluation carried out in these experiments. The $p-$value $= 0.9903$ in Table 4.14 indicates that there is no significant difference between the selected groups representing the different sampling methods, and the box plot in Figure 4.11 confirms this result.

We observed that ARMSTG produced more singular matrices with adaptive sampling when estimating the RBF than the other two methods. This is because adaptive sampling can generate spatially consecutive samples that induce linearly dependent equations. For this reason, despite of being the method that generated the result most consistent with the selected parameter values, one cannot state that it is the best choice for sampling.

4.3.3 Shape-based *vs* Semi-spherical Tumor Growth Simulation Models

In this thesis, we have remarked than one of the main differences of our method in comparison with other methods is the fact that it simulates the tumor growth process in the atlas space and that we used a tumor model based on the real tumor shape as opposed to a simple spherical model. The purpose of this experiment is to evaluate the tumor growth simulation model introduced in Chapter 3 in comparison to a spherical model.

For this experiment, we took each segmented tumor for each patient case and built a semi-spherical tumor mask following this procedure:

1. For each axial slice containing a part of the tumor, we fit the tumor segmentation in a circular mask as shown in Figure 4.12. The segmented tumor is circumscribed in the best circle that enclosed the whole segmented tumor, *i.e.* the circle with the minimum ratio to cover the whole segmented area (Figure 4.12a);

2. We then applied AND binary image operator to fit each circular mask in the brain tissue as shown in Figure 4.12b.

Then, we used ARMSTG's level set procedure to built a displacement map as explained in Section 3.3 (see Figure 4.12c), and performed a ARMSTG simulation using the three sampling methods implemented in this thesis. In this way, we obtained three groups of observations, one for each sampling method: adaptive, poisson and uniform, and each one containing the twelve MRI cases. These three groups plus the three groups evaluated in the

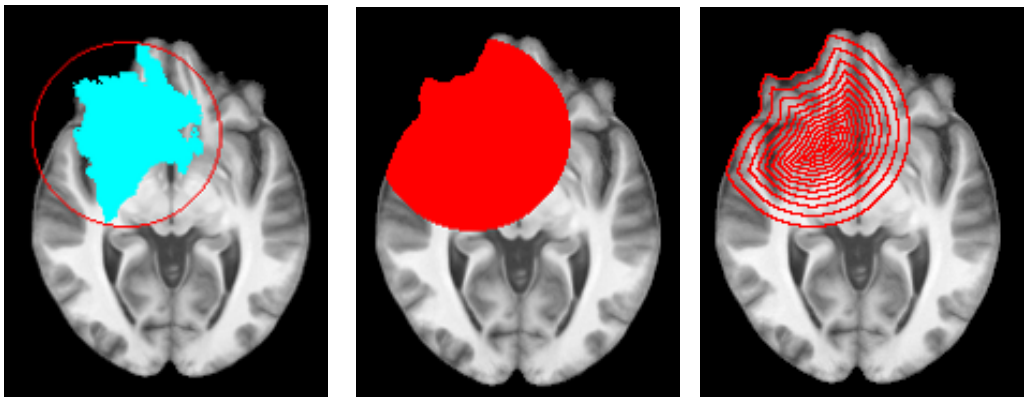

(a) (b) (c)

Figure 4.12: Circular tumor growth model. (a) segmented tumor circumscribed by a circle. (b) circular mask representing the tumor area. (c) level set.

experiment previously, *i.e.* the three groups in Figure 4.11, were compared using Kruska-Wallis test. The results of this experiments are summarized in Table 4.15 and Figure 4.13 is a box plot where one can see the differences between the similarity metric means for each tumor growth model and each sampling. Figure 4.14 shows the deformation obtained over one slice using the semi-spherical tumor growth model and the deformation obtained with our model.

Table 4.15: ANOVA table generated with Kruskal Wallis to compare circular tumor growth model *vs* real shape tumor growth model.

Source	SS	df	MS	χ^2	Prob $> \chi^2$
Columns	4,218.6	5	843.72	13.83	0.0167
Error	13,776.4	54	255.119		
Total	17,995	59			

We obtained a $p-$ value $= 0.0167$, less than 0.05, which means that the null hypothesis is rejected at the 5% significance level. At least one group stochastically dominates another group. Figure 4.13 shows that ARMSTG implemented with the tumor growth simulation model based on real shape performed better than the implementation with the semi-spherical model. Although, circular masks are individually fit for each slice containing part of the segmented tumor, the growth simulation is carried out over the set of node representing 3D sampled points in the problem domain. Therefore, in this thesis we have used the term semi-spherical tumor growth model.

Discussion

With this experiment, we have demonstrated that the proposed tumor growth model based on the real tumor shape and level set contributes to a good ARMSTG's performance. The

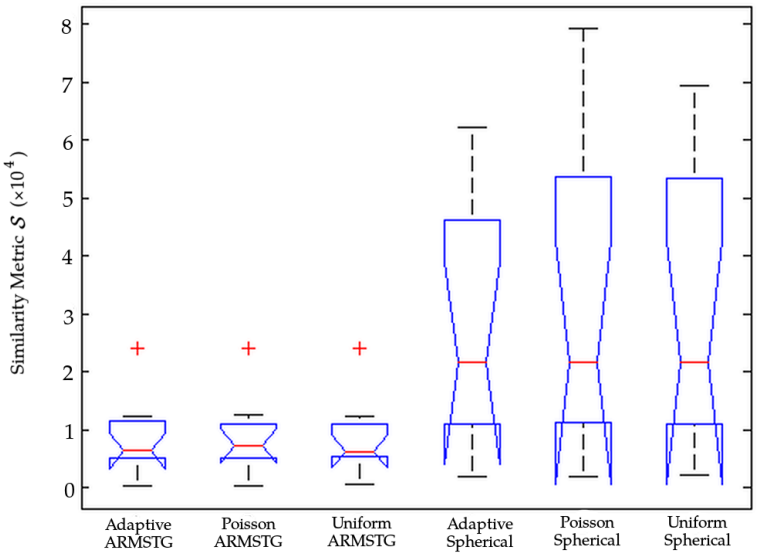

Figure 4.13: Box plot comparison tumor growth models, based on tumor shape and semi-spherical. The similarity metric is in mm.

$p-$ value $= 0.0167$ indicates that the groups can not be treated as equal, and Figure 4.13 makes clear that ARMSTG performed better with the different sampling methods and our tumor growth model, than with the different samplings and the spherical tumor growth model. Figure 4.14b shows that a possible cause of the bad results obtained with the semi-spherical model could be the extension of the area covered by the circular mask, which is much larger than the area covered by the real tumor. Therefore, one can intuitively say that the method performs a more extensive deformation which leads to bad results. For our patient cases, circles circumscribed inside of the tumor area, which would cover less tumor area, could not be the solution either, since large areas of the real tumor would be excluded of the tumor mass-effect simulation, also leading to highly dissimilar images.

4.3.4 ARMSTG *vs* Other Brain Registration Methods

ARMSTG *vs* Direct Registration With Diffeomorphic Demons Algorithm

In Section 3.6, we proposed to register binary masks of the brain tissue from the atlas with patient images instead of performing the registration directly over the images with their original intensity scales. The purpose of this analysis was to evaluate whether the process of the tumor growth and mass-effect simulation proposed in this thesis improves the results of the binary mask registration. In order to carry out this evaluation, we registered the binary masks of the atlas and patient images using the same diffeomorphic demons registration [41, 91, 95] employed in the last stage of ARMSTG, *i.e.* we performed the registration directly without introducing the patient's tumor into the atlas image. For this experiment,

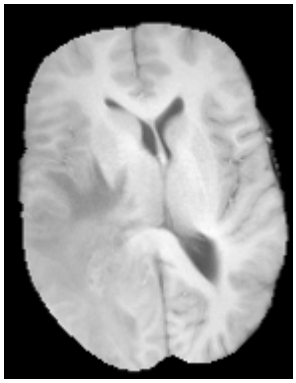

(a) Original Slice

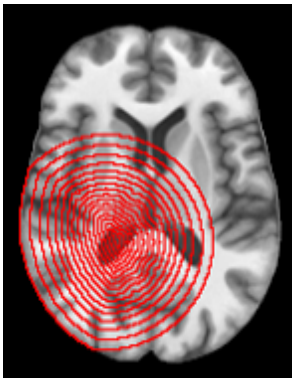

(b) Circular level set

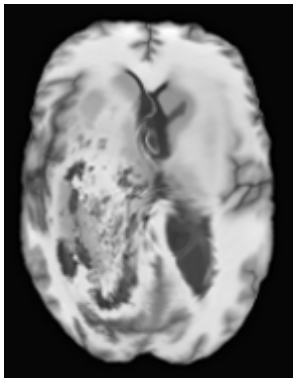

(c) Circular tumor growth

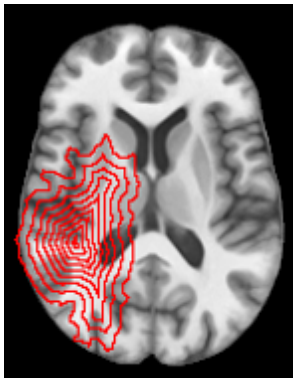

(d) Real shape level set

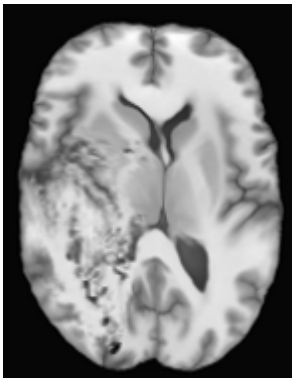

(e) Proposed tumor growth

Figure 4.14: Circular tumor growth model result. (a) original slice taken from a patient case. (b) level set of the circular mask. (c) registration result using the circular level set. (d) registration result using the tumor real shape.

we took the binary mask of the atlas brain tissue and registered it with a binary mask of each patient brain tissue. The binary masks of the patient were generated using the threshold th_1 compute by STS algorithm and described in Section 3.1.

The registration results of these experiment were analyzed using Kruskal-Wallis test. We performed the experiment with 4 groups corresponding to ARMSTG with the three

sampling methods, and the diffeomorphic demon registration of the binary masks without tumor. The ANOVA analysis is presented in Table 4.16 and Figures 4.15 and 4.16 shows the means distribution for the the 4 groups.

Table 4.16: Anova table generated with Kruskal-Wallis to compare ARMSTG's with direct diffeomorphic demon registration.

Source	SS	df	MS	χ^2	Prob $> \chi^2$
Columns	2,537.17	3	879.056	13.45	0.0037
Error	6,574.83	44	149.428		
Total	9,212	47			

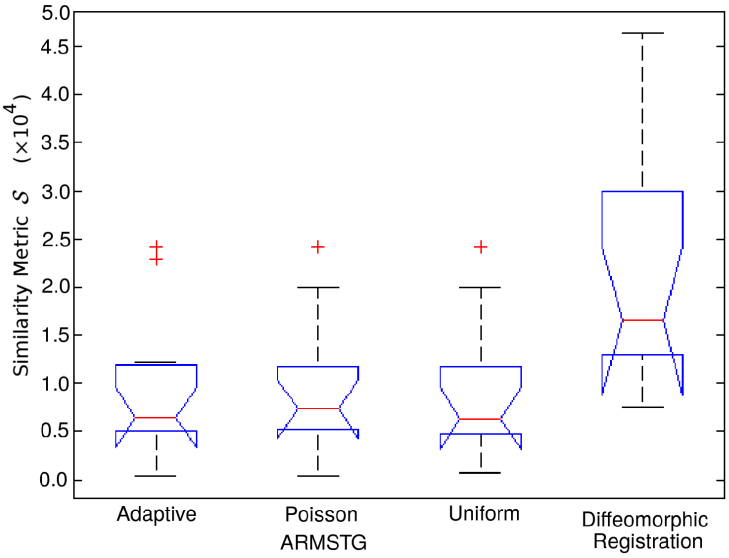

Figure 4.15: Box plot ARMSTG *vs* direct diffeomorphic demon registration.

The $p-$value obtained in this test was 0.0037 as the last column in Table 4.15 shows. This $p-$value rejects the null hypothesis of similar distribution between groups at the 5% confidence level, meaning that there is at least one group of observations dominating the others. Figure 4.16 shows the mean distances between the ventricles of the patient's images and the registered images. The three first box plots represent the evaluation of the registered images with ARMSTG using the three implemented sampling methods, and the fourth group represents the evaluation of the registered images with diffeomorphic demon registration directly. In this figure one can see that ARMSTG obtained a better evaluation with any of the sampling methods, than the direct registration of the images using dffeomorphic demon registration. Figure 4.16 also illustrates the difference of the similarity distance means between ARMSTG results and direct diffeomorphic demons registration results, showing the superiority of ARMSTG.

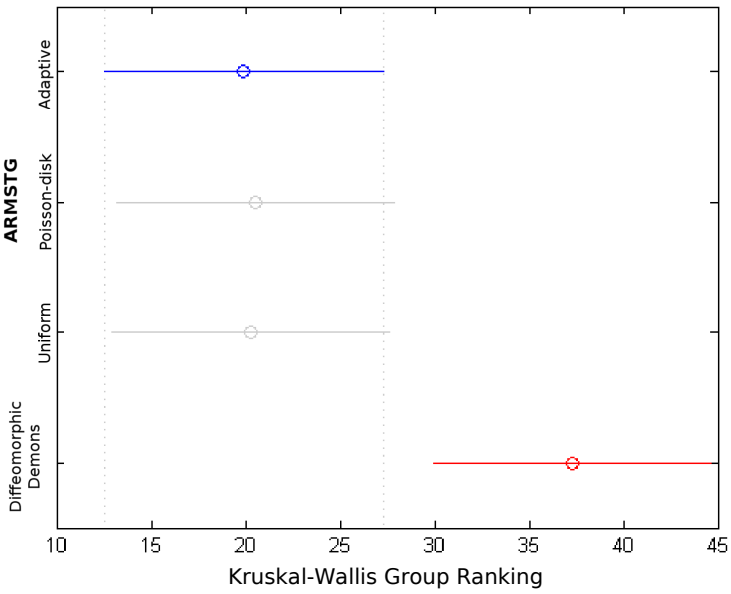

Figure 4.16: Pairwise comparison of mean ranks to evaluate ARMSTG *vs* direct diffeomorphic demon registration.

ARMSTG *vs* Other Brain MRI Registration Methods

We also compared the performance of ARMSTG with other registration methods, such as the Automatic Registration Toolbox (ART) [94], and the symmetric diffeomorphic image registration with cross-correlation (SyN), described in [3, 4]. Both algorithms yielded the best registration results in the evaluation described by Klein *et al.* [46], who evaluated fourteen non-linear deformation algorithms applied to human brain MRI registration. In that evaluation, ART and SyN were classified as the top ranking.

In order to perform these comparisons, we added two more groups to the data set obtained by ARMSTG with different sampling methods. The two new groups represented the results obtained by SyN and ART. This time sixty data sets divided in five groups were analyzed with the Kruskal-Wallis test. The results are summarized in Table 4.17 and Figure 4.17 and Figure 4.18.

Table 4.17: Kruskal-Wallis results comparing ARMSTG *vs* SyN and ART.

Source	SS	df	MS	χ^2	Prob $> \chi^2$
Columns	9,532.83	4	2,383.21	31.26	2.17e-06
Error	8,462.17	55	153.86		
Total	17,995	59			

In this test, we obtained a $p-$ value $= 2.17 \times 10^{-6}$ which indicates that at least one group dominates the others at the 5% confidence level. Figure 4.17 shows that ARMSTG with the different sampling methods (Adaptive, Poisson-disk and Uniform) produced better

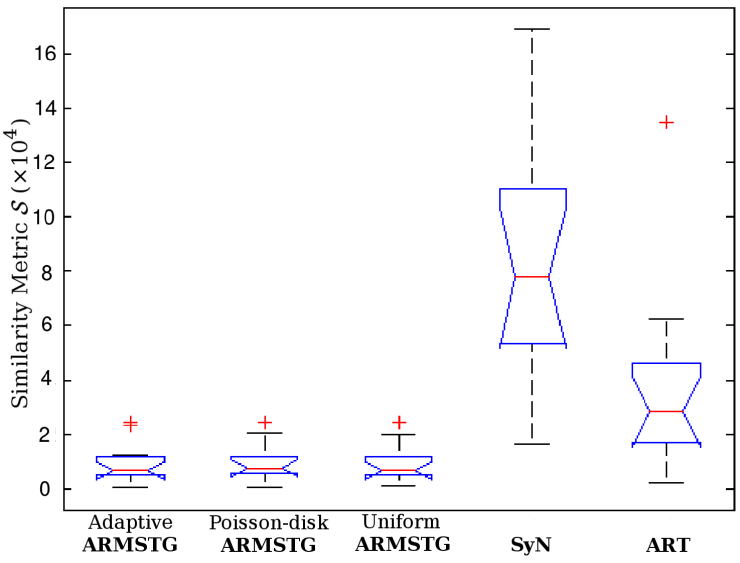

Figure 4.17: Box plot ARMSTG *vs* other registration methods

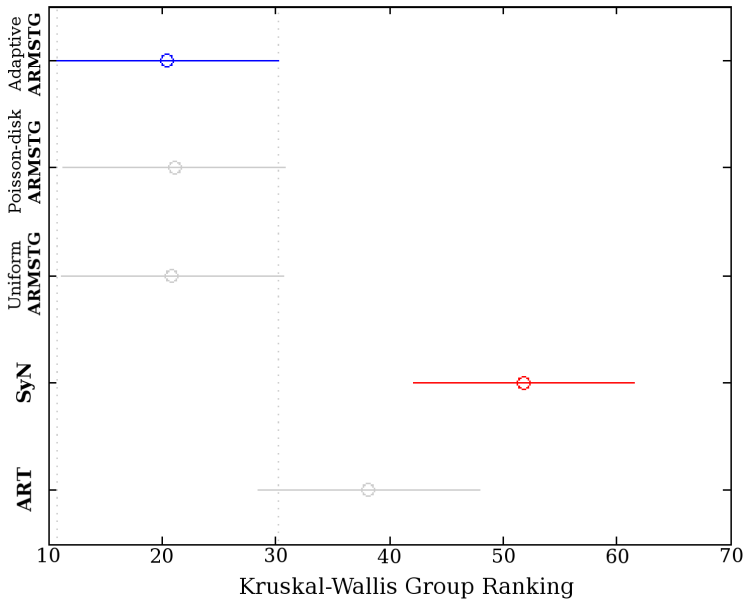

Figure 4.18: Pairwise comparison of mean ranks to evaluate ARMSTG *vs* other registration methods.

results than SyN and ART. Figure 4.18 also shows the differences between the similarity distance mean values between the evaluated methods.

Discussion

The experiment designed to compare ARMSTG *vs* Direct Diffeomorphic Demons proves that introducing the patient's tumor in the atlas via tumor growth and mass-effect simulation

improves the results of the atlas registration. This result is supported by a $p-$ value $=$ 0.0037 obtained in the respective statistical test and illustrated in Figures 4.15 and 4.16. One can see that the figures show evident visual improvement of ARMSTG over the direct Diffeomorphic Demons registration. Figure 4.19 also supports this affirmation; the atlas image after applying the displacement field produced by the direct diffeomorphic demon registration looks distorted in comparison to the original patient image; while the image produced by ARMSTG looks structurally similar to the patient image. The patient image in the figure was rotated to be aligned with the sagittal axis.

ARMSTG also outperformed SyN and ART as the $p-$ value $= 2.17 \times 10^{-6}$ as the statistical test points out. Figure 4.17 and Figure 4.18 show the difference between the methods. ARMSTG obtained the smallest mean distance in comparison to the other two methods; while SyN obtained the worst performance result. The superiority of ARMSTG in comparison with SyN and ART can also be seen in Figure 4.20 which shows an example of the registration obtained with the three methods. Figure 4.19 only shows the registration result obtained by ARMSTG's with uniform sampling for simplicity as the rest of results obtained with the other sampling methods are very similar.

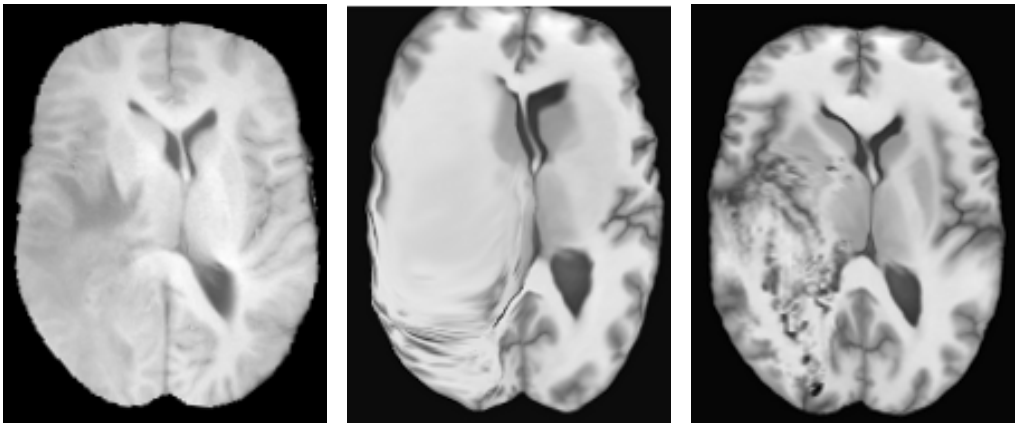

(a) Patient (b) Diffeomorphic Registration (c) ARMSTG

Figure 4.19: ARMSTG *vs* direct diffeomorphic registration.

4.3.5 Running Time between CPU and GPU Implementations

The purpose of this test was to evaluate the advantage of using GPU and CUDA to compute the tumor growth and mass-effect simulation. We compared the computation time of ARMSTG implemented with the compute power of GPU, and an identical version of the method implemented with CPU. This test was carried out over the data set for the twelve patient's cases. Figure 4.21 shows a plot of the total computation time for both versions and for all the cases. The red line correspond to the total time spent by the CPU version on each case, and the blue line corresponds to the total time spent by the parallel implementation of

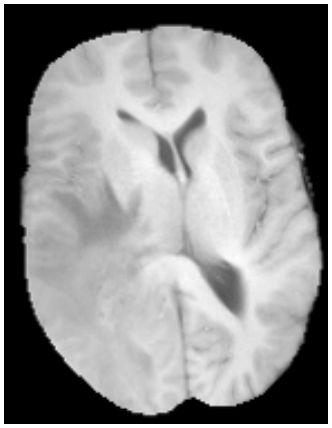

(a) Original Patient

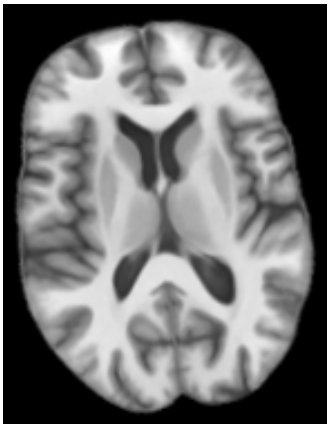

(b) SyN

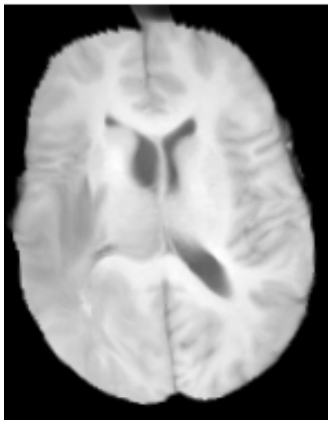

(c) ART

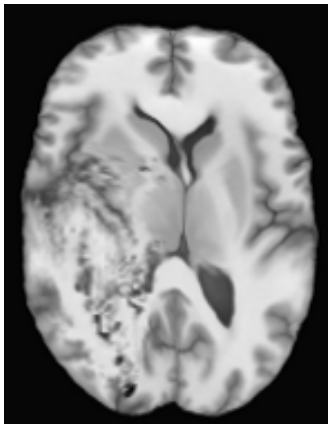

(d) ARMSTG

Figure 4.20: ARMSTG *vs* SyN and ART registrations.

ARMSTG using GPU and CUDA. Both results were obtained using Poisson-disk sampling method and the set of parameter values given in Table 4.13.

Both version GPU and CUDA were implemented on the same workstation with the specifications given in Tables 3.2 and 3.3.

Discussion

All the registration results analyzed in this work were generated using a version of the method implemented with CUDA on a GPU. We evaluated the advantage of this implementation in comparison to a version of the method implemented on CPU. Figure 4.21 illustrates the differences in computation time between the two versions. The use of GPU reduced the total computation time required to carried out a tumor growth and mass-effect simulation by 45% . The mean computation time for the GPU version was 85 seconds, while the mean computation time of the CPU version was 188.58 seconds. This performance could be improved by using newer more powerful GPUs like the new Titan Z from NVIDIA which has 5760 CUDA cores. In addition, more powerful architectures using mul-

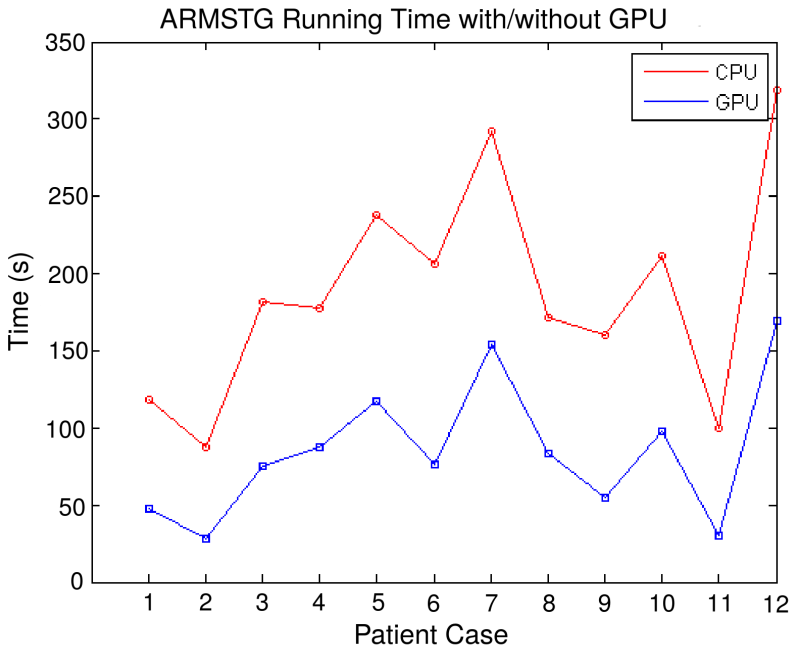

Figure 4.21: Running time for ARMSTG with GPU *vs* CPU for each patient case.

tiple GPUs based on unified memory architecture can be used to accelerate this simulation further.

4.4 Qualitative Evaluation

Additionally to the quantitative evaluation presented in this chapter, we also evaluated ARMSTG results visually. The registration results of the atlas to the twelve patient with different grades of glioma selected in this thesis are illustrated in Figures A.1, A.2, and A.3 in Appendix A. From left to right, first column shows the patient images, the second column shows ARMSTG's registration results, and the third and fourth columns show the registration results obtained with SyN and ART. In general one can observe very good similarity between the atlas image registered to the patients cases using ARMSTG in comparison with the other two methods. In cases with large deformations such as the last row in Figure A.1, the third row in Figure A.2 and the last row in Figure A.3 one can see the advantage of ARMSTG in pushing and deforming the atlas brain structures according to the source image. The results obtained with the three algorithms compared in these figures might look more similar for cases with small tumors causing small deformation as the case in the third row in Figure A.1 shows.

Chapter 5

Conclusion

Registering atlas to brain MRI is a challenging task due to the differences between the target and source images. The challenge is compounded even more when the patient's image contains a tumor because the mass-effect deforms the brain structure and augments the anatomical differences between the atlas and the patient's image.

Some authors have concluded that many traditional non-linear registration methods fail when tumors are present [16, 18, 31, 48, 64, 107]. Our work has confirmed this conclusion with the experiments conducted in Section 4.3.4, where we were able to show that without simulation of the tumor growth process some non-linear methods for brain registration are not capable of representing accurately the deformation. The results presented in Section 4.3.4 shows that our approach outperformed two of the top ranking algorithms found in the literature SyN [3, 4] and ART [94], as well as the famous diffeomorphic demon registration [41, 91, 95]. These three methods have been widely used for non-linear registration of brain MRIs.

In particular, Avants *et al.* [3] states that SyN obtains good results when the distance between the template brain and the target brain is large, which is the case for patients with brain tumor. However, this method had the worst performance in experiments carried out in Section 4.3.4. One reason for this result is that Avant's *et al.* does not consider images with tumor in the development of his method. The authors used images of normal and dementia patients whose brain structural differences are not as large as the differences between a normal and a patient brain with tumor.

ART is a program of non-linear inter-subject registration of 3D structural MRI scans provided by the Neuroimaging Informatics Tools and Resources Clearinghouse (NITRC) [94]. This tool for brain image registration is not able to deal with large deformation caused by brain tumor as shown in Figure 4.17 and Table 4.17. Klein *et al.* [46] used both methods ART and SyN to co-register brain images and to establish correspondences across brain structures. Both methods were evaluated with several image data sets and ranked as the best methods to co-register brain MRI images and perform comparative morphometry. However, our experiments show that these two methods are not as good as our method.

Figure A.1, Figure A.2, and Figure A.3 in Appendix A illustrate the great capabilities of the proposed method. In the figures one can see the similarity between slices of the

patient images used in the experiments and the registration results and how it outperform results obtained with SyN and ART methods.

Section 4.3.4 also shows that ARMSTG outperformed the diffeomorphic demon registration [41, 91, 95] of the images without the process of introducing the tumor patient in the atlas image. Algorithms based on demon registration [91] have been evaluated before in other works for the purpose of registering images with large deformation caused by diseases [3, 16, 18], and it has been demonstrated that this algorithm alone fails when large differences between the target and the source images are present. In this work, we have proved that the results of diffeomorphic demon registration considerably improves when ARMSTG is first applied. We use diffeomorphic demon registration in ARMSTG only as a last step because of its availability and easy use trough 3D Slicer [41, 75].

5.1 ARMSTG Advantages

The key component of ARMSTG is that contrary to the other three non-linear methods evaluated in this work, our method deforms the brain structures in the atlas by simulating the tumor growth and mass-effect using a bio-mechanical model. The experimental results in Section 4.3.4 proved that the strategy of introducing the tumor in the atlas simulating an actual tumor growth lessens the difference between the target and the source, which improves the registration results. Although other authors introduced a similar strategy [31, 64, 107], ARMSTG extends the concept by using a total Lagrangian mesh-less method for the simulation, and a guided tumor growth model using the actual shape of the segmented tumor from the original multi-modal MRI's of a patient.

The use of a mesh-less method provided many advantages to ARMSTG, such as the ability of handling large deformations without re-meshing, and making possible the use of the proposed tumor growth model guided by the actual shape of the tumor instead of a spherical or regular shape. Our tumor growth model does not deal with the problem of seed initialization as the methods in [31, 64, 107]. ARMSTG does not require to search for the initial seed position with an optimization procedure and is not sensitive to the initial seed size, as demonstrated in Section 4.3.1.

Moreover, experimental results in Section 4.3.3 demonstrated that our tumor growth model guided by segmented patient multi-modal MRIs is superior and more realistic than a simple regular shape model, such as a sphere. As demonstrated in this thesis, if one uses a semi-spherical growth tumor model, the shape over deforms the atlas structures and produce bad results. The strategy of using a regular shape to deform the atlas could work well for cases with small tumors that look like spheres. However, in most cases tumors have irregular shapes.

Besides the robustness of ARMSTG to parameter variation related to seed size, we found that the method is also robust to different sampling methods such as: adaptive, Poisson-disk and uniform. The experimental results in Section 4.3.2 support this conclusion. Also, one can see in Section 4.3.1 that ARMSTG performance is not affected by

parameter variations related to the level set procedure, such as the iteration number and the parameter a in Equation 3.2.

Another advantage of ARMSTG is that it uses GPU, which substantially helped to reduce the computational time required for the tumor growth and mass-effect calculations. Although, some authors [42, 88, 102] have implemented the TLED algorithm proposed in [60] in GPU, our mesh-less implementation is unique and efficient. Besides, we not only implemented in parallel the iterative main loops of the algorithm as illustrated in Figure 3.15, but also implemented in parallel the computation of the shape functions and its derivatives.

The proposed method is an alternative that can be used to register brain MRIs with tumor to a common stereotaxic space for the purpose of segmenting brain structures or doing image comparisons. Another interesting application of the method is the interactive surgical simulation when deformation of virtual organs is required. One of the major limitation for this kind of application is the significant computation time to perform large organ deformation if one use FEM methods. A GPU implementation of non-linear constitutive model such as the algorithm implemented for ARMSTG overcomes this limitation.

With ARMSTG, we have extended non-linear registration methods based on bio-mechanical simulation in the following aspects:

1. We have developed a complete mesh-free implementation of TLED for brain atlas to patient registration with tumor;

2. We have integrated the mesh-free TLED implementation with a tumor growth model based on the real shape of the tumor using a simple segmentation of multi-modal MRIs of the patient;

3. We have implemented in parallel our method with GPU, reducing considerably the computation time.

5.2 Some Implementation Issues

During the development of ARMSTG there were some implementation issues that are also important to mention here:

One of them is that ARMSTG yielded better results when the distances between nodes are small. This observation make sense since mesh-free computations rely on point neighborhoods to which shape functions are fitted. The more compact the neighborhoods (support domain) are, the better the geometry representation is. However, processing large point samples requires a lot of computation power and time. Fortunately, because of the large computational power of GPU's, one can use large sample sizes as seen in Table 4.1.

Another important issue observed during the development of ARMSTG is that, although Section 4.3.1 shows that there were not effects created by the seed size, we found

that it is better to use a small number of seed points to avoid singularities in the linear equation systems. This is because if the initial position of the seed points at the beginning of the simulation are located at the same place as the center of the inner tumor contour generated by the level set, singularities can be produced. If the number of seed points is large, the method will have a support domain where the majority of the seed points are too close to each other and may generate a singular equation system. A small numbers of seed points *i.e.* less than the half of the support domain size, did not create singularity problems. In the future, we will distribute the seed points randomly around the tumor center in order to reduce the possibility of producing singular equation systems.

5.2.1 Limitations

They are also some limitations to ARMSTG:

An important limitation was the quality and quantity of the set of MRIs taken from BRATS challenge. Although BRATS challenge provides four MRIs sequence for each patient, some of them look like reconstructed images with aliasing effects. The parenchyma in some patient's cases are not complete for all the modalities, as a consequence, we had to discard these cases. As a future work, we would like to evaluate ARMSTG's performance with a better quality set of images. The main reason to persist in the use of BRATS data set is that, in spite this problem, the data set provides manual tumor segmentations for each patient case which have been use for benchmark the segmentation methods. Hence, during the development of ARMSTG, we did not worry about the problem relating to the accuracy of tumor segmentation. This can be an issue of our method when other data set without tumor segmentations are selected.

Another limitation that we had during our GPU implementation is the use of some specialized schemes that improve memory access speed to texture and shared memories. These limitation was due to the large number of samples handled in the calculations for different sampling methods (see Table 4.1). However, one can obtain a considerable reduction in running time when compared with a CPU version of the algorithm as shown in Figure 4.21. Although we used local memory, which is not the fastest type of memory in a GPU, we reduced the amount of CPU-GPU communication by loading the most used variables in the initialisation part of the simulation to the GPU memory such as: nodal support domains, shape function derivatives, forces and displacements. All the operations related to these variables were carried out directly in GPU when the simulation starts.

5.3 Future Work

As a future work, we would like to extend ARMSTG's structure or pipeline to be applied to other human organ registration such as lung, bladder and others. Also, we would like to extend ARMSTG to simulate brain deformation during surgery and compare the result with the method designed for this purpose such as [8, 42, 102].

We would also like to evaluate ARMSTG over other data set containing images with better quality, and to improve the initial distribution of tumor seed points in the atlas. Also, we would like to evaluate other non-linear registration algorithm (other than the diffeomorphic demon) for the last stage of ARMSTG.

Another future work is the improvement of STS for brain tumor segmentation. Although, our segmentation method yield good results for the image set provided by the Brain Tumor Analysis Project at University of Alberta (Section 3.1), we would like to evaluate the method with other data set, and to implement a more robust technique to localize the tumor threshold th_2 (Figure 3.2, in Section 3.1).

Bibliography

[1] David Adalsteinsson and James A. Sethian. A fast level set method for propagating interfaces. *J. Comput. Phys.*, 118(2):269–277, May 1995. ISSN 0021-9991. doi:10.1006/jcph.1995.1098.

[2] P. Aljabar, K. Bhatia, M. Murgasova, J. Hajnal, Boardman. J., L. Srinivasan, M. Rutherford, L. Dyet, A. Edwards, and D. Rueckert. Assessment of brain growth in early childhood using deformation-based morphometry. *NeuroImage*, 39(1):348–358, 2008. ISSN 1053-8119. doi:10.1016/j.neuroimage.2007.07.067.

[3] B. B. Avants, C. L. Epstein, M. Grossman, and J. C. Gee. Symmetric diffeomorphic image registration with cross-correlation: Evaluating automated labeling of elderly and neurodegenerative brain. *Med. Image Anal.*, 12(1):26–41, 2008. ISSN 1361-8415. doi:10.1016/j.media.2007.06.004. Special Issue on The Third International Workshop on Biomedical Image Registration WBIR 2006.

[4] Brian B. Avants, Nicholas J. Tustison, Gang Song, Philip A. Cook, Arno Klein, and James C. Gee. A reproducible evaluation of ANTs similarity metric performance in brain image registration. *NeuroImage*, 54(3):2033–2044, 2011. doi:10.1016/j.neuroimage.2010.09.025.

[5] Isaac N. Bankman. *Handbook of Medical Image: Processing and Analysis*. Academic Press series in biomedical engineering. Academic Press, second edition edition, December 2008.

[6] Klaus Jurgen Bathe. *Finite Element Procedures in Engineering Analysis*, volume 106 of *Prentice-Hall civil engineering and engineering mechanics series*. Prentice Hall, 1982. ISBN 0133173054.

[7] Jan-Philip Bergeest and Florian Jäger. A Comparison of Five Methods for Signal Intensity Standardization in MRI Bildverarbeitung für die Medizin 2008. In Thomas Tolxdorff, Jürgen Braun, Thomas Deserno, Alexander Horsch, Heinz Handels, Hans-Peter Meinzer, W Brauer, and Gesellschaft für Informatik GI, editors, *Bildverarbeitung für die Medizin 2008 SE - Informatik Aktuell*, pages 36–40. Springer Berlin Heidelberg, Berlin, Heidelberg, 2008. ISBN 978-3-540-78639-9. doi:10.1007/978-3-540-78640-5_8.

[8] J. Berger, A. Horton, Grand Joldes, Adam Wittek, and Karol Miller. Coupling finite element and mesh-free methods for modelling brain deformation in response to tumour growth. *MIDAS Journal - Computational Biomechanics*, jun 2008. URL `http://hdl.handle.net/10380/1383`.

[9] Lynne E. Bilston. Brain tissue mechanical properties. In Karol Miller, editor, *Biomechanics of the Brain*, Biological and Medical Physics, Biomedical Engineering, chapter 4, pages 69–89. Springer New York, 2011. ISBN 978-1-4419-9997-9. doi:10.1007/978-1-4419-9997-9_4.

[10] Maurice A. Biot. General theory of three-dimensional consolidation. *J. Appl. Phys.*, 12(2): 155–164, 1941. ISSN 00218979. doi:10.1063/1.1712886.

[11] Martin D. Buhmann. *Radial Basis Functions: Theory and Implementations*. Cambridge University Press, 2003.

[12] Mariano Cabezas, Arnau Oliver, Xavier Lladó, Jordi Freixenet, and Meritxell Cuadra-Bach. A Review of Atlas-based Segmentation for Magnetic Resonance Brain Images. *Comput. Meth. Prog. Bio.*, 104(3):158–177, December 2011. ISSN 0169-2607. doi:10.1016/j.cmpb.2011.07.015.

[13] Timothy J. Carter, Maxime Sermesant, David M. Cash, Dean C. Barratt, Christine Tanner, and David J. Hawkes. Application of soft tissue modelling to image-guided surgery. *Med. Eng. Phys.*, 27(10):893–909, 2005. doi:10.1016/j.medengphy.2005.10.005.

[14] Media Centre. World Health Organization, 2012.

[15] Laurence P. Clarke, Robert P. Velthuizen, Matt Clark, Jorge Gaviria, Larry Hall, Dmitry Goldgof, Reed Murtagh, S. Phuphanich, and Steven Brem. MRI Measurement of Brain Tumor Response: Comparison of Visual Metric and Automatic Segmentation. *Magn. Reson. Imaging*, 16(3):271–279, April 1998. ISSN 0730-725X. doi:10.1016/S0730-725X(97)00302-0.

[16] Meritxell Bach Cuadra, Claudio Pollo, Anton Bardera, Olivier Cuisenaire, Jean-Guy Villemure, and Jean-Philippe Thiran. Atlas-based segmentation of pathological MR brain images using a model of lesion growth. *IEEE Trans. Med. Imaging*, 23(10):1301–1314, 2004. doi:10.1109/TMI.2004.834618.

[17] Christos Davatzikos. Spatial transformation and registration of brain images using elastically deformable models. *Comput. Vis. Image Und.*, 66(2):207–222, May 1997. doi:10.1006/cviu.1997.0605.

[18] B. M. Dawant, S. L. Hartmann, Shiyan Pan, and S. Gadamsetty. Brain atlas deformation in the presence of small and large space-occupying tumors. *Comput. Aided Surg.*, 7(1):1–10, 2002. doi:10.1002/igs.10029.

[19] Idanis Diaz, Pierre Boulanger, Russell Greiner, and Albert Murtha. A critical review of the effects of de-noising algorithms on MRI brain tumor segmentation. In *Engineering in Medicine and Biology Society, EMBC, 2011. Proceedings of the 33rd Annual International Conference of the IEEE on*, pages 3934–3937. IEEE, Boston, MA, August 30 – September 3 2011. doi:10.1109/IEMBS.2011.6090977.

[20] Idanis Diaz, Pierre Boulanger, Russell Greiner, Bret Hoehn, Lindsay Rowe, and Albert Murtha. An automatic brain tumor segmentation tool. In *Engineering in Medicine and Biology Society (EMBC), 2013 35th Annual International Conference of the IEEE*, pages 3339–3342. IEEE, San Diego, CA, July 3–7 2013. doi:10.1109/EMBC.2013.6610256.

[21] Lee R. Dice. Measures of the Amount of Ecologic Association Between Species. *Ecology*, 26(3):297–302, July 1945. URL `http://www.jstor.org/stable/1932409`.

[22] Shen Dinggang and Christos Davatzikos. HAMMER: hierarchical attribute matching mechanism for elastic registration. *IEEE Trans. Med. Imaging*, 21(1):1421–1439, November 2002. doi:10.1109/TMI.2002.803111.

[23] Daniel Dunbar and Greg Humphreys. A spatial data structure for fast poisson-disk sample generation. *ACM Trans. Graph.*, 25(3):503–508, July 2006. ISSN 0730-0301. doi:10.1145/1141911.1141915.

[24] Robert W. Floyd and Steinberg Louis. An adaptive algorithm for spatial greyscale. *Proc. Soc. Inf. Disp.*, 17(2):75–77, 1976.

[25] D. Frederick and T. S. Chang. *Continuum mechanics*. Allyn and Bacon series in mechanical engineering and applied mechanics. Allyn and Bacon, 1963.

[26] Jerome Friedman, Trevor Hastie, and Robert Tibshirani. Additive logistic regression: a statistical view of boosting. *Annals of Statistics.*, 28(2):337–407, 1998.

[27] Milton Friedman. A comparison of alternative tests of significance for the problem of m rankings. *Ann. Math. Statist.*, 11(1):86–92, March 1940. doi:10.1214/aoms/1177731944.

[28] Y. C. Fung. *Biomechanics: Mechanical Properties of Living Tissues*, volume 2. Springer, 1993. ISBN 0-387-97947-6.

[29] Mary L Gawne-Cain, Stephanie Webb, Paul Tofts, and David H Miller. Lesion volume measurement in multiple sclerosis: How important is accurate repositioning? *J. Magn. Reson. Imaging*, 6(5):705–713, 1996. ISSN 1522-2586. doi:10.1002/jmri.1880060502.

[30] GLOBOCAN 2008 (IARC) Section of Cancer Information. GLOBOCAN 2008, 2012.

[31] Ali Gooya, George Biros, and Christos Davatzikos. Deformable registration of glioma images using EM algorithm and diffusion reaction modeling. *IEEE Trans. Med. Imaging*, 30 (2):375–390, February 2011. ISSN 02780062. doi:10.1109/TMI.2010.2078833.

[32] Genetha A Gray and Tamara G Kolda. Asynchronous Parallel Pattern Search for Derivative-Free Optimization. *ACM Trans. Math. Software*, 32(3):485–507, 2006. doi:10.1145/1163641.1163647.

[33] Charles R G Guttmann, Ron Kikinis, Mark C Anderson, Marianna Jakab, Simon K Warfield, Ron J Killiany, Howard L Weiner, and Ferenc A Jolesz. Quantitative follow-up of patients with multiple sclerosis using MRI: Reproducibility. *J. Magn. Reson. Imaging*, 9(4): 509–518, 1999. ISSN 1522-2586. doi:10.1002/(SICI)1522-2586(199904)9:4<509::AID-JMRI2>3.0.CO;2-S.

[34] Joseph Hajnal, Nadeem Saeed, Angela Oatridge, Elaine Williams, Ian Young, and Graeme Bydder. Detection of subtle brain changes using subvoxel registration and subtraction of serial MR images. *J. Comput. Assist. Tomo.*, 19(5):677–691, 1995. ISSN 0363-8715.

[35] Joseph Hajnal, Nadeem Saeed, Elaine Soar, Angela Oatridge, Ian Young, and Graeme Bydder. A Registration and Interpolation Procedure for Subvoxel Matching of Serially Acquired MR Images. *J. Comput. Assist. Tomo.*, 19(2):289–296, 1995.

[36] S. Hakim, J. G. Venegas, and J. D. Burton. The physics of the cranial cavity, hydrocephalus and normal pressure hydrocephalus: Mechanical interpretation and mathematical model. *Surg. Neurol.*, 5(3):187–210, 1976.

[37] Cosmina Hogea, George Biros, Feby Abraham, and Christos Davatzikos. A robust framework for soft tissue simulations with application to modeling brain tumor mass effect. *Phys. Med. Biol.*, 52(23):6893, 2007. ISSN 0031-9155. doi:10.1088/0031-9155/52/23/008.

[38] Cosmina Hogea, Christos Davatzikos, and George Biros. An image-driven parameter estimation problem for a reaction-diffusion glioma growth model with mass effects. *J. Math. Biol.*, 56(6):793–825, 2008. doi:10.1007/s00285-007-0139-x.

[39] Ashley Horton, Adam Wittek, Grand Roman Joldes, and Karol Miller. A meshless total Lagrangian explicit dynamics algorithm for surgical simulation. *Int. J. Numer. Method. Biomed. Eng.*, 26:977–998, March 2010. doi:10.1002/cnm.1374.

[40] Ahmedin Jemal, Freddie Bray, Melissa M Center, Jacques Ferlay, Elizabeth Ward, and David Forman. Global cancer statistics. *CA: A Cancer Journal for Clinicians*, 61(2):69–90, mar apr 2011. ISSN 1542-4863. doi:10.3322/caac.20107.

[41] H. Johnson and Y. Zhao. BRAINSDemonWarp: An applicaton to perform demons registration. *Insight J.*, jan – jun 2009. URL `http://hdl.handle.net/1926/1517`.

[42] Grand Roman Joldes, Adam Wittek, and Karol Miller. Real-time nonlinear finite element computations on {GPU} application to neurosurgical simulation. *Computer Methods in Applied Mechanics and Engineering*, 199(4952):3305–3314, 2010. ISSN 0045-7825. doi:10.1016/j.cma.2010.06.037.

[43] M. Jones, J. A. Baerentzen, and M. Sramek. 3D distance fields: a survey of techniques and applications. *IEEE Trans. Vis. Comput. Graph.*, 12(4):581–599, July 2006. ISSN 1077-2626. doi:10.1109/TVCG.2006.56.

[44] Fahmi Khalifa, Garth M. Beache, Georgy Gimel'farb, Jasjit S. Suri, and Ayman S. El-Baz. State-of-the-Art Medical Image Registration Methodologies: A Survey. In Ayman S. El-Baz, Rajendra Acharya U., Majid Mirmehdi, and Jasjit S. Suri, editors, *Multi Modality State-of-the-Art Medical Image Segmentation an dRegistration Methodologies*, volume 1, pages 235–280. Springer US, 2011. ISBN 978-1-4419-8195-0. doi:10.1007/978-1-4419-8195-0_9.

[45] Kitware. Insight Segmentation and Registration Toolkit (ITK). Electronic, 2012. URL `http://www.itk.org`.

[46] A. Klein, J. Andersson, B. A. Ardekani, J. Ashburner, B. Avants, Ming-Chang Chiang, G. E. Christensen, L. Collins, J. Gee, P Hellier, Song, M. Jenkinson, Lepage C., Rueckert, Thompson, Vercauteren, Woods, Mann, and Parsey. Evaluation of 14 nonlinear deformation algorithms applied to human brain MRI registration. *NeuroImage*, 46(3):786–802, 2009. ISSN 1053-8119. doi:10.1016/j.neuroimage.2008.12.037.

[47] William H. Kruskal and W. Allen Wallis. Use of Ranks in One-Criterion Variance Analysis. *J. Am. Stat. Assoc.*, 47(260):583–621, 1952. ISSN 01621459. doi:10.2307/2280779.

[48] S. K. Kyriacou, Christos Davatzikos, S. J. Zinreich, and R. Nick Bryan. Nonlinear elastic registration of brain images with tumor pathology using a biomechanical model. *IEEE Trans. Med. Imaging*, 18(7):580–592, July 1999. doi:10.1109/42.790458.

[49] Louis Lemieux, Udo C Wieshmann, Nicholas F Moran, David R Fish, and Simon D Shorvon. The detection and significance of subtle changes in mixed-signal brain lesions by serial MRI scan matching and spatial normalization. *Med. Image Anal.*, 2(3):227–242, sep 1998. doi:10.1016/S1361-8415(98)80021-2.

[50] G. R. Liu. *Meshfree Methods: Moving Beyond the Finite Element Method*. CRC Press, second edition edition, October 2002. ISBN 978-1-4200-8209-8.

[51] G. R. Liu and Y. T. Gu. *An Introduction to Meshfree Methods and Their Programming*. Springer, 2005.

[52] A Madabhushi and J K Udupa. Interplay between intensity standardization and inhomogeneity correction in MR image processing. *IEEE Trans. Med. Imaging*, 24(5):561–576, 2005. ISSN 0278-0062. doi:10.1109/TMI.2004.843256.

[53] G. E. Mase and G. T. Mase. *Continuum Mechanics for Engineers, Second Edition*. Computational Mechanics and Applied Analysis Series. Taylor & Francis, 1999. ISBN 978-0-8493-1855-9.

[54] MATLAB. *version 9.0.0.783 (R2012b)*. The MathWorks Inc., Natick, Massachusetts, 2012.

[55] Gary Mavko, Tapan Mukerji, and Jack Dvorkin. *The Rock Physics Handbook: Tools for Seismic Analysis of Porous Media*. Stanford-Cambridge Program. Cambridge University Press, 2009. ISBN 0-521-86136-5.

[56] Gloria P. Mazzara, Robert P. Velthuizen, James L. Pearlman, Harvey M. Greenberg, and Henry Wagner. Brain Tumor Target Volume Determination for Radiation Treatment Planning Through Automated MRI Segmentation. *Int. J. Radiat. Oncol.*, 59(1):300–312, 2004. ISSN 03603016. doi:10.1016/j.ijrobp.2004.01.026.

[57] T. H. G. Megson. *Structural and Stress Analysis*. Amsterdam: Elsevier Butterworth-Heinemanl, 2005. ISBN 0-7506-6221-2.

[58] Bjoern Menze, Andras Jakab, and Stefan Bauer. The Multimodal Brain Tumor Image Segmentation Benchmark (BRATS). *IEEE Trans. Med. Imaging*, page 33, 2014. doi:10.1109/TMI.2014.2377694.

[59] Karol Miller and Kiyoyuki Chinzei. Mechanical properties of brain tissue in tension. *J. Biomech.*, 35(4):483–490, 2002. doi:10.1016/S0021-9290(01)00234-2.

[60] Karol Miller, Grand Joldes, Dane Lance, and Adam Wittek. Total Lagrangian explicit dynamics finite element algorithm for computing soft tissue deformation. *Commun. Numer. Methods Eng.*, 23(2):121–134, feb 2007. doi:10.1002/cnm.887.

[61] Karol Miller, Adam Wittek, and Grand Joldes. Biomechanics of the brain for computer-integrated surgery. *Acta Bioeng. Biomech.*, 12(2):25–37, 2010. URL `http://www.actabio.pwr.wroc.pl/Vol12No2/2.pdf`.

[62] Karol Miller, Adam Wittek, and Grand Joldes. Biomechanical modeling of the brain for computer-assisted neurosurgery. In Karol Miller, editor, *Biomechanics of the Brain*, Biological and Medical Physics, Biomedical Engineering, pages 111–136. Springer New York, 2011. ISBN 978-1-4419-9996-2. doi:10.1007/978-1-4419-9997-9_6.

[63] Ashraf Mohamed and Christos Davatzikos. Finite element modeling of brain tumor mass-effect from 3D medical images. In *Medical Image Computing And Computer-Assisted Intervention (MICCAI 2005). Proceedings of the 8th International Conference on,*, volume LNCS-3749 of *Lecture Notes in Computer Science*, pages 400–408. Springer, 2005. doi:10.1007/11566465_50.

[64] Ashraf Mohamed, Evangelia I Zacharaki, Dinggang Shen, and Christos Davatzikos. Deformable registration of brain tumor images via a statistical model of tumor-induced deformation. *Med. Image Anal.*, 10(5):752–63, 2006. ISSN 13618415. doi:10.1016/j.media.2006.06.005.

[65] Matthias Müller, David Charypar, and Markus Gross. Particle-based fluid simulation for interactive applications. In *Proceedings of the 2003 ACM SIGGRAPH/Eurographics Symposium on Computer Animation*, SCA '03, pages 154–159, San Diego, CA, USA, July 27–31 2003. Eurographics Association. ISBN 1-58113-659-5.

[66] Matthias Müller, R. Keiser, A. Nealen, M. Pauly, M. Gross, and M. Alexa. Point based animation of elastic, plastic and melting objects. In *Proceedings of the 2004 ACM SIGGRAPH/Eurographics Symposium on Computer Animation*, SCA '04, pages 141–151, Los Angeles, CA, USA, August 8–12 2004. ACM Association for Computing Machinery. ISBN 3-905673-14-2. doi:10.1145/1028523.1028542.

[67] R. Greiner Murtha, M. Brown, and A. Brain Tumour Analysis Project, 2012. http://webdocs.cs.ualberta.ca/ btap/people.php.

[68] László G Nyúl and Jayaram K Udupa. On standardizing the MR image intensity scale. *Magn. Reson. Med.*, 42(6):1072–1081, 1999. ISSN 1522-2594. doi:10.1002/(SICI)1522-2594(199912)42:6<1072::AID-MRM11>3.0.CO;2-M.

[69] Stanley Osher and Ronald Fedkiw. *Level Set Methods and Dynamic Implicit Surfaces*. Springer Verlag, 2003. ISBN 978-0-387-95482-0.

[70] Stanley Osher and James A. Sethian. Fronts propagating with curvature-dependent speed: algorithms based on Hamilton-Jacobi formulations. *J. Comput. Phys.*, 79(1):12–49, November 1988. ISSN 0021-9991. doi:10.1016/0021-9991(88)90002-2.

[71] Sarah Parisot, William Wells III, Stphane Chemouny, Hugues Duffau, and Nikos Paragios. Concurrent tumor segmentation and registration with uncertainty-based sparse non-uniform graphs. *Med. Image Anal.*, 18(4):647–659, 2014. doi:10.1016/j.media.2014.02.006.

[72] Julia Patriarche and Bradley Erickson. A Review of the Automated Detection of Change in Serial Imaging Studies of the Brain. *J. Digit. Imaging*, 17(3):158–174, September 2004. ISSN 0897-1889. doi:10.1007/s10278-004-1010-x.

[73] Keith D. Paulsen and Michael I. Miga. Biomechanical modeling for image registration: Applications in image guided neurosurgery. In Joseph V. Hajnal, Derek L. G. Hill, and David J. Hawkes, editors, *Medical Image Registration*, chapter 15, pages 331–362. CRC Press, Cambridge, 2001. doi:10.1201/9781420042474.ch15.

[74] Dzung L. Pham, Chenyang Xu, and Jerry L. Prince. Current methods in medical image segmentation. *Annu. Rev. Biomed. Eng.*, 2(1):315–337, August 2000. doi:10.1146/annurev.bioeng.2.1.315.

[75] S Pieper, B Lorensen, W Schroeder, and R Kikinis. The NA-MIC Kit: ITK, VTK, pipelines, grids and 3D slicer as an open platform for the medical image computing community, 2006.

[76] Marcel Prastawa, Elizabeth Bullitt, Sean Ho, and Guido Gerig. A brain tumor segmentation framework based on outlier detection. *Med. Image Anal.*, 8(3):275–283, 2004. doi:10.1016/j.media.2004.06.007.

[77] David Rey, Gérard Subsol, Hervé Delingette, and Nicholas Ayache. Automatic detection and segmentation of evolving processes in 3D medical images: Application to multiple sclerosis. *Med. Image Anal.*, 6(2):163–179, June 2002. ISSN 1361-8415. doi:10.1016/S1361-8415(02)00056-7.

[78] Torsten Rohlfing, Natalie M. Zahr, Edith V. Sullivan, and Adolf Pfefferbaum. The SRI24 multichannel atlas of normal adult human brain structure. *Human Brain Mapping*, 31(5): 798–819, 2009. ISSN 10659471. doi:10.1002/hbm.20906.

[79] Jean Rothman and MPH Medically reviewed by Niya Jones, MD. Brain Tumor Statistics, 2012.

[80] D. Rueckert. Nonrigid registration: Concepts, Algorithms, and Applications. In J V Hajnal, L G Hill, and D J Hawkes, editors, *Medical Image Registration*, pages 281–302. CRC Press, Cambridge, 2001.

[81] Mohamed Ben Salah, Idanis Diaz, Russell Greiner, Pierre Boulanger, Bret Hoehn, and Albert Murtha. Fully automated brain tumor segmentation using two MRI modalities. In *Advances in Visual Computing*, volume 8033 of *Lecture Notes in Computer Science*, pages 30–39. Springer Berlin Heidelberg, 2013. ISBN 978-3-642-41913-3. doi:10.1007/978-3-642-41914-0_4.

[82] Abraham Savitzky and M. J. E. Golay. Smoothing and differentiation of data by simplified least squares procedures. *Anal. Chem.*, 36(8):1627–1639, 1964. doi:10.1021/ac60214a047.

[83] James A. Sethian. *Level Set Methods and Fast Marching Methods: Evolving Interfaces in Computational Geometry, Fluid Mechanics, Computer Vision, and Materials Science*. Cambridge University Press, June 1999. ISBN 0-521-64557-3.

[84] Pierre Soille. *Morphological Image Analysis: Principles and Applications*. Springer, 2010.

[85] Murray R. Spiegel, John J. Schiller, and R. Alu Srinivasan. *Schaum's Outline of Probability and Statistics*. McGraw-Hill, 2 edition, March 2000. ISBN 0-07-135004-7.

[86] Radu Stefanescu, Xavier Pennec, and Nicholas Ayache. Grid Enabled Non-rigid Registration with a Dense Transformation and a priori Information. In *6th International Conference on Medical Image Computing and Computer-Assisted Intervention International – MICCAI 2003*, volume LNCS 2879 of *Lecture Notes in Computer Science*, pages 804–811, Montreal, Canada, November 15–18 2003. Springer. ISBN 978-3-540-20464-0. doi:10.1007/978-3-540-39903-2_98.

[87] Radu Stefanescu Stefanescu, Olivier Commowick, Grégoire Malandain, Pierre-Yves Bondiau, Nicholas Ayache, and Xavier Pennec. Non-rigid Atlas to Subject Registration with Pathologies for Conformal Brain Radiotherapy. In *7th International Conference on Medical Image Computing and Computer-Assisted Intervention International – MICCAI 2004*, volume LNCS 3216 of *Lecture Notes in Computer Science*, pages 704–711, Saint-Malo, France, September 26–29 2004. Springer. ISBN 978-3-540-30135-6. doi:10.1007/978-3-540-30135-6_86.

[88] Z. Taylor, M. Cheng, and S. Ourselin. High-speed nonlinear finite element analysis for surgical simulation using graphics processing units. *IEEE Trans. Med. Imaging*, 27(5):650–663, may 2008. doi:10.1109/TMI.2007.913112.

[89] Jean-Philippe Thirion. New feature points based on geometric invariants for 3D image registration. *Int. J. Comput. Vision*, 18(2):121–137, 1996. ISSN 09205691. doi:10.1007/BF00054999.

[90] Jean-Philippe Thirion. Measuring lesion growth from 3D medical images. In G. Calmon, editor, *Motion of Non-Rigid and Articulated Objects, 1997 IEEE Computer Society Workshop on*, volume 0, page 112, June 1997. ISBN 0-8186-8040-7. doi:10.1109/NAMW.1997.609861.

[91] Jean-Philippe Thirion. Image matching as a diffusion process: An analogy with Maxwell's demons. *Med. Image Anal.*, 2(3):243–260, 1998. ISSN 13618415. doi:10.1016/S1361-8415(98)80022-4.

[92] Paul M. Thompson, Michael S. Mega, Roger P. Woods, Chris I. Zoumalan, Chris J. Lindshield, Rebecca E. Blanton, Jacob Moussai, Colin J. Holmes, Jeffrey L. Cummings, and Arthur W. Toga. Cortical change in alzheimer's disease detected with a disease-specific population-based brain atlas. *Cereb. Cortex*, 11(1):1–16, 2001 January 2001. ISSN 1047-3211. doi:10.1093/cercor/11.1.1.

[93] Arthur W. Toga and Paul M. Thompson. Image registration and the construction of multidimensional brain atlases. In Isaac N. Bankman, editor, *Handbook of Medical Imaging: Processing and Analysis*, chapter 43, pages 635–653. Academic Press, Orlando, FL, USA, second edition edition, 2009. ISBN 0-12-077790-8. doi:10.1016/B978-012373904-9.50053-2.

[94] The Neuroimaging Informatics Tools and Resources Clearinghouse (NITRC). Automatic registration toolbox, 2011. URL `http://www.nitrc.org/projects/art/`.

[95] Tom Vercauteren, Xavier Pennec, Aymeric Perchant, and Nicholas Ayache. Non-parametric Diffeomorphic Image Registration with the Demons Algorithm. In Nicholas Ayache, Sébastien Ourselin, and Anthony Maeder, editors, *Medical Image Computing and Computer*

Assisted Intervention (MICCAI'07), volume 4792/2007 of *Lecture Notes in Computer Science*, pages 319–326, Brisbane, Australia, October 29 – November 2 2007. Springer. ISBN 978-3-540-30135-6. doi:10.1007/978-3-540-75759-7_39.

[96] U. Vovk, F. Pernus, and B. Likar. A Review of Methods for Correction of Intensity Inhomogeneity in MRI. *IEEE Trans. Med. Imaging*, 26(3):405–421, 2007. ISSN 0278-0062. doi:10.1109/TMI.2006.891486.

[97] Richard Wasserman, Raj Acharya, Claudio Sibata, and K H Shin. A patient-specific *In Vivo* tumor model. *Math. Biosci.*, 136(2):111–140, sep 1996. ISSN 00255564. doi:10.1016/0025-5564(96)00045-4.

[98] L. Weizman, Ben Sira L., Joskowicz L., Constantini S., Precel R., Shofty B., and Ben Bashat D. Automatic segmentation, internal classification, and follow-up of optic pathway gliomas in MRI. *Med. Image Anal.*, 16(1):177–188, 2012. ISSN 1361-8415. doi:10.1016/j.media.2011.07.001.

[99] Caroline Weltens, Johan Menten, Michel Feron, Erwin Bellon, Philippe Demaerel, Frederik Maes, Walter Van den Bogaert, and Emmanuel van der Schueren. Interobserver variations in gross tumor volume delineation of brain tumors on computed tomography and impact of magnetic resonance imaging. *Radiother. Oncol.*, 60(1):49–59, July 2001. ISSN 0167-8140. doi:10.1016/S0167-8140(01)00371-1.

[100] Adam Wittek, Karol Miller, Ron Kikinis, and S.K. Warfield. Patient-specific model of brain deformation: application to medical image registration. *J. Biomech.*, 40(4):919–929, 2007. doi:doi:10.1016/j.jbiomech.2006.02.021.

[101] Adam Wittek, T. Dutta-Roy, Z. Taylor, A. Horton, T. Washio, K. Chinzei, and Karol Miller. Subject-specific non-linear biomechanical model of needle insertion into brain. *Comput Methods Biomech Biomed Engin*, 11(2):135–146, feb 2008. doi:10.1080/10255840701688095.

[102] Adam Wittek, Grand Joldes, Mathieu Couton, Simon K. Warfield, and Karol Miller. Patient-specific non-linear finite element modelling for predicting soft organ deformation in real-time; application to non-rigid neuroimage registration. *Prog. Biophys. Mol. Biol.*, 103(2–3): 292–303, dec 2010. ISSN 0079-6107. doi:10.1016/j.pbiomolbio.2010.09.001.

[103] Yongyi Yang, Miles N. Wernick, and Jovan G. Brankov. A fast approach for accurate content-adaptive mesh generation. *IEEE Trans. Image Proc.*, 12(8):866–881, 2003. doi:10.1109/TIP.2003.812757.

[104] Liu Yanxi, Robert T. Collins, and William E. Rothfus. Robust midsagittal plane extraction from normal and pathological 3D neuroradiology images. *IEEE Trans. Med. Imaging*, 20(3): 175–192, 2001. doi:10.1109/42.918469.

[105] Evangelia I. Zacharaki, Cosmina S. Hogea, George Biros, and Christos Davatzikos. A comparative study of biomechanical simulators in deformable registration of brain tumor images. *IEEE Trans. Bio-Med. Eng.*, 55(3):1233–1236, 2008. doi:10.1109/TBME.2007.905484.

[106] Evangelia I. Zacharaki, Dinggang Shen, Seung-Koo Lee, and Christos Davatzikos. ORBIT: A multiresolution framework for deformable registration of brain tumor images. *IEEE Trans. Med. Imaging*, 27(8):1003–1017, aug 2008. doi:10.1109/TMI.2008.916954.

[107] Evangelia I. Zacharaki, Hogea Cosmina S, Dinggang Shen, George Biros, and Christos Davatzikos. Non-diffeomorphic registration of brain tumor images by simulating tissue loss and tumor growth. *NeuroImage*, 46(3):762–774, jul 2009. ISSN 10538119. doi:10.1016/j.neuroimage.2009.01.051.

[108] Johnny Zhang, Grand Joldes, Adam Wittek, A.T. Horton, S. K. Warfield, and Karol Miller. Neuroimage as a biomechanical model: Toward new computational biomechanics of the brain. In P. M. F. Nielsen, A. Wittek, and K. Miller, editors, *Computational Biomechanics for Medicine*, pages 19–28. Springer, 2012. ISBN 9781461431718.

Appendix A

Results of ARMSTG vs. SyN and ART

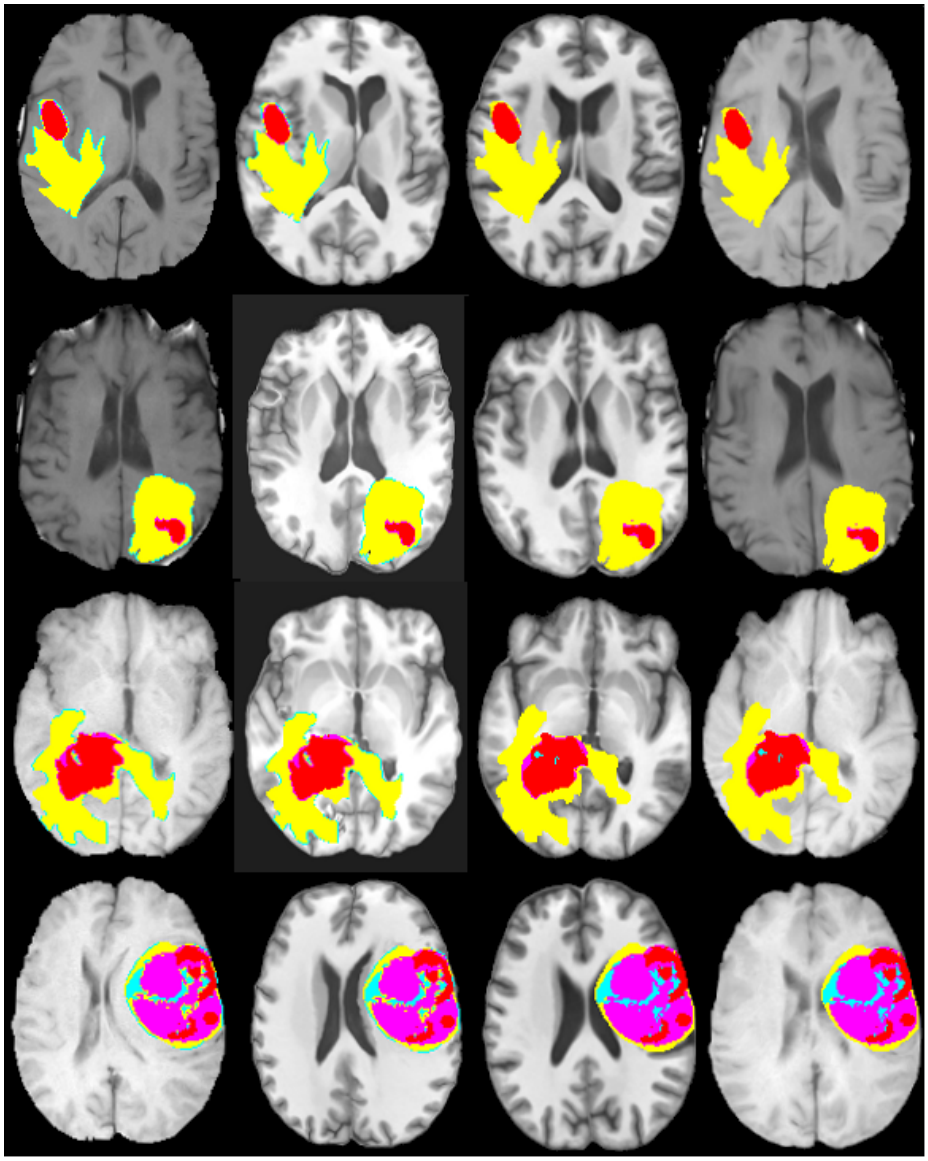

Figure A.1: ARMSTG's results in comparison to SyN's results and ART's results. Each row corresponds to the cases 1 to 4 taken from the data set provided by the BRATS challenge [58]. From left to right the original image, ARMSTG, SyN and ART registrations containing the manual segmented tumor provided by the BRATS data set. The colors in the tumors represent, yellow edema, red enhancing tumor, magenta non-enhancing tumor, cyan necrosis.

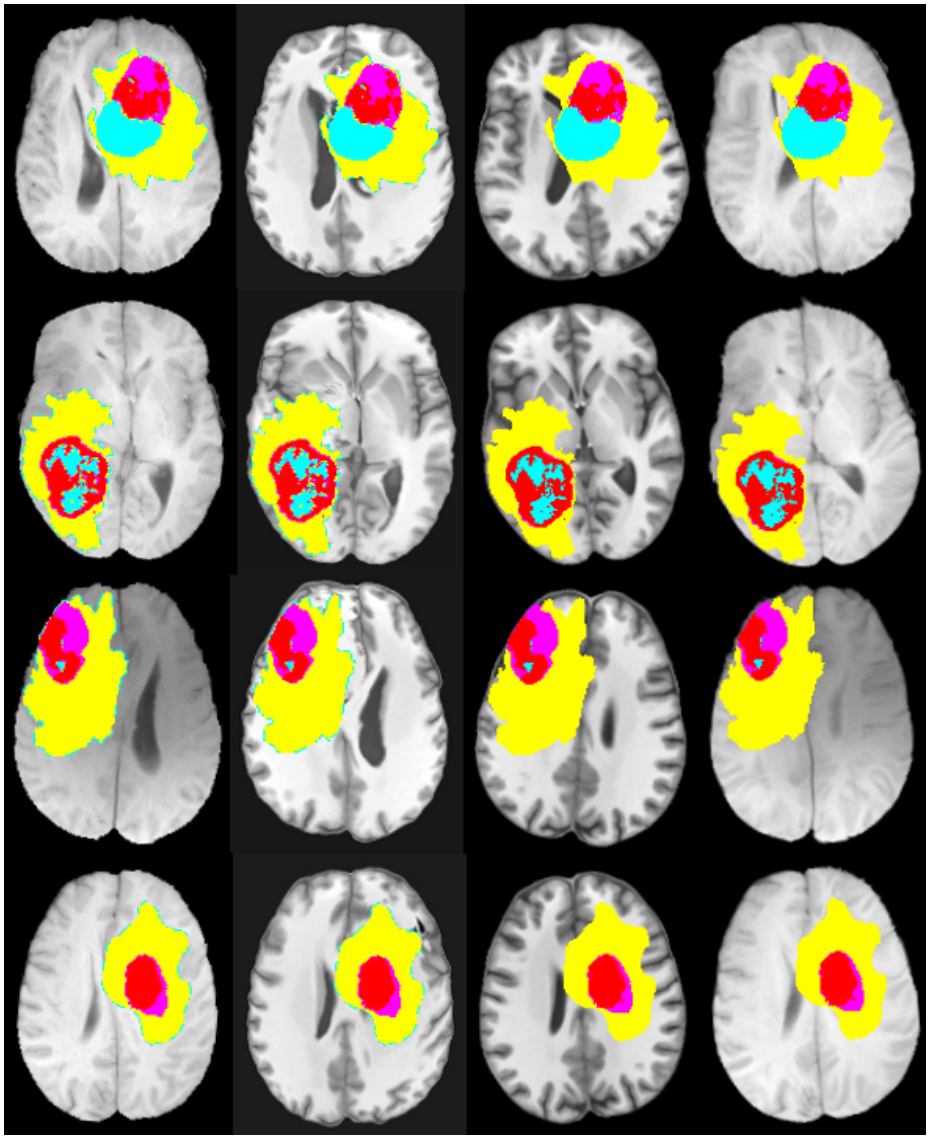

Figure A.2: ARMSTG's results in comparison to SyN's results and ART's results. Each row corresponds to the cases 5 to 8 taken from the data set provided by the BRATS challenge [58]. From left to right the original image, ARMSTG, SyN and ART registrations containing the manual segmented tumor provided by the BRATS data set. The colors in the tumors represent, yellow edema, red enhancing tumor, magenta non-enhancing tumor, cyan necrosis.

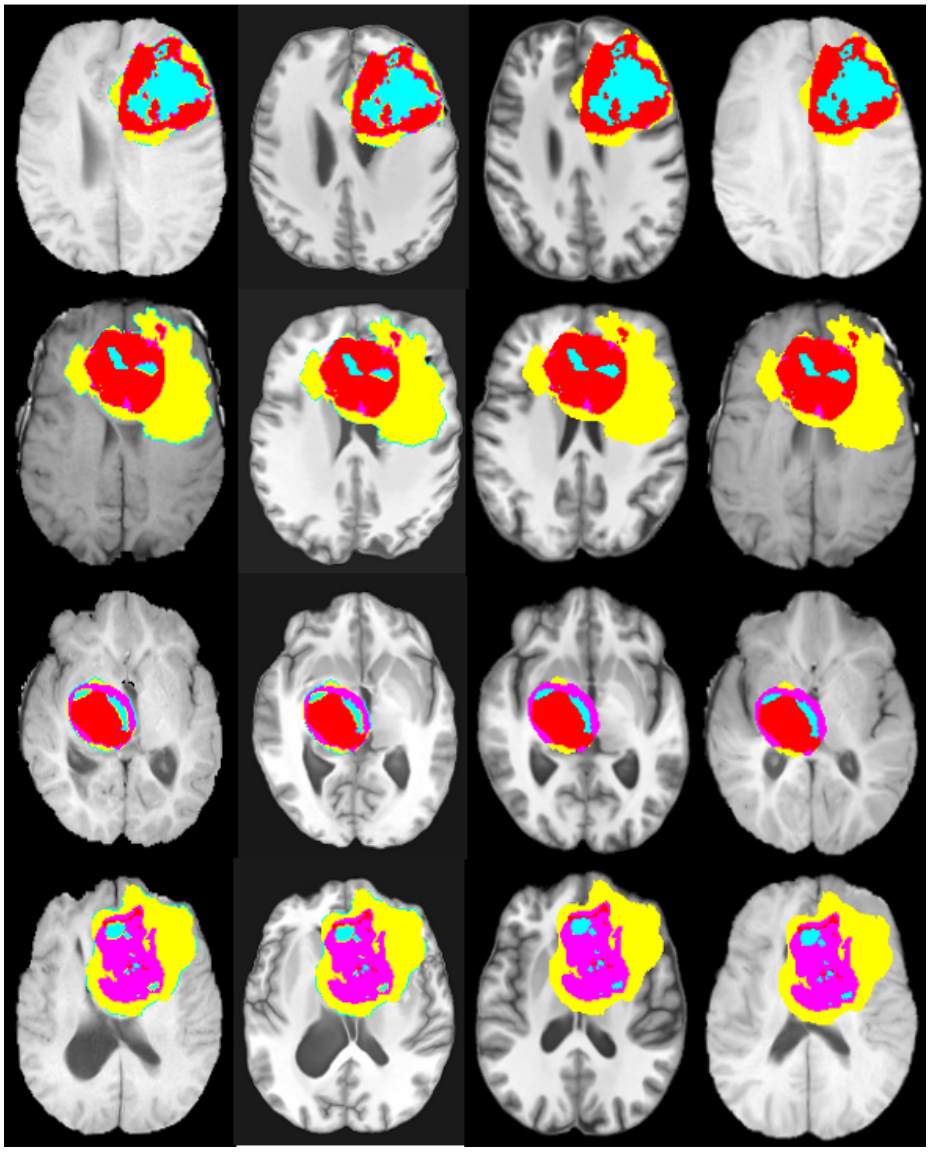

Figure A.3: ARMSTG's results in comparison to SyN's results and ART's results. Each row corresponds to the cases 9 to 12 taken from the data set provided by the BRATS challenge [58]. From left to right the original image, ARMSTG, SyN and ART registrations containing the manual segmented tumor provided by the BRATS data set. The colors in the tumors represent, yellow edema, red enhancing tumor, magenta non-enhancing tumor, cyan necrosis.